

Quantum Mechanical Modeling of Sorption of Actinides on Mineral Surfaces and Complexation with Clay Organics Under Conditions of Deep Geological Repositories

**Abschlussbericht für das Teilprojekt
„Quantenmechanische Modellierung zur Sorption von Actiniden an Mineraloberflächen und Komplexierung mit Tonorganika unter Endlagerbedingungen“**

**im Rahmen des Verbundprojektes
„Rückhaltung endlagerrelevanter Radionuklide
im natürlichem Tongestein und in salinaren Systemen“**

**Förderkennzeichen 02E11001
Projektlaufzeit Juli 2011 bis August 2015**

**Sven Krüger, Alena Kremleva
Department Chemie, Technische Universität München
85747 Garching**

Contents

1 Introduction	3
2 Project Tasks and Prerequisites.....	5
3 Development of the state of the art	8
4 Results	10
4.1 Actinide Complexes	10
4.1.1 Am(III) in aqueous solution	10
The Am(III) aqua ion	10
Am(III) hydroxide.....	11
4.1.2 Complexation with carboxylic acids	11
Formiate and Acetate	12
Lactate	20
4.1.3 Acetate in saline media: Ternary acetato chloride complexes	23
4.1.4 Borate and Boratester complexes.....	26
Comparison of Ligands and Model Complexes.....	26
Borate Complexes	27
Hydroxoborate Complexes	32
Borate Ester Complexes.....	33
4.2 Adsorption of actinides on clay minerals.....	35
4.2.1 Edge surfaces of charged clay minerals	35
Mineral models	35
Edge surfaces	37
4.2.2 U(VI) adsorption	40
Adsorption sites	40
Adsorbed species	41
Detailed comparison of exemplary complexes on various mineral models.....	42
Adsorption at unsubstituted sites	43
Adsorption at substituted sites	46
Energies.....	48
Comparison to experiment.....	49
Effect of coverage	51
Variation of layer charge.....	53
Equilibration of the solvation layer and improved energies	56
Adsorption at Fe surface substitutions	59
4.2.3 Np(V) adsorption	62
4.2.4 Adsorption of salt cations.....	67
4.3 Method development.....	69
4.3.1 Low temperature partial equilibration.....	69
4.3.2 Surface solvation by PCM	71
5 Summary	73
6 Publikations resulting from this project	75
7 References	76

Das diesem Bericht zugrundeliegende Vorhaben wurde mit Mitteln des Bundesministeriums für Wirtschaft und Technologie unter dem Förderkennzeichen 02E11001 gefördert. Die Verantwortung für den Inhalt der Veröffentlichung liegt bei den Autoren.

1 Introduction

Distribution and transport of actinides in the environment is a central topic of safety considerations and environmental protection regarding radioactive waste and its safe long-term storage in an underground repository. Uranium plays here a central role as the common fuel in nuclear power plants. Other actinides with long half-lives appear as fission products. Essential for understanding and prediction of the fate of actinide containing materials under repository or environmental conditions is a thorough knowledge of the pertinent chemistry involved, forming a prerequisite for reliable modeling of distribution and transport of these elements. This necessary chemistry knowledge includes first of all the identification of pertinent actinide compounds under various relevant conditions. In this respect complexes in solution and at mineral and construction or containment materials surfaces as well as solid and colloidal phases are of interest. Furthermore the equilibrium thermodynamics of these compounds has to be determined to account for their chemical reaction equilibria. In addition also kinetic considerations are necessary to discern fast and slow and thus less probable reaction pathways, which nevertheless play a role, taking into account the long storage times envisaged for highly radioactive waste. While for many actinide complexes in aqueous in solution the speciation is clarified and basic thermodynamic data are available at acidic pH and at room temperature [1-4], this information is more scarce at basic pH conditions, where also the speciation is less developed, and at higher temperatures [1]. The surface chemistry of actinides interacting with mineral surfaces is by far less well understood [5-7]. Here the knowledge on adsorbed species and on pertinent adsorption sites is until now rather limited and available thermodynamical models, although incorporating the available insight from various experiments, are essentially empirical [8-10]. A thorough knowledge on species and processes at the atomic level at pertinent conditions given by the host rock formations chosen for a final repository is essential for a mechanistic understanding of the actinide chemistry, allowing reliable and transferable predictions and modeling, also beyond the range experimentally accessible.

This project had been a contribution to the consortium “Rückhaltung endlagerrelevanter Radionuklide im natürlichen Tongestein und in salinaren Systemen”. It was the goal of this project in the consortium to contribute by means of quantum chemical calculations to a mechanistic understanding of actinide chemistry pertinent to long term storage of highly active nuclear waste in a deep geological repository in a clay formation, focusing on actinide adsorption on clay minerals and actinide chemistry in solution, also under saline conditions.

The computational approach applying accurate quantum chemical methods is complementary to experiment. Experimental studies of actinides in solutions and in interaction with mineral surfaces are commonly facing situations where several species are present, making their individual characterization rather difficult. Notably this is the case when there are no pertinent conditions where a particular species is dominant or when one has to

distinguish between various possible isomers or adsorption sites at mineral surfaces. Here the quantum chemical approach is helpful, as well defined species are treated and many of their properties can be determined with reliable accuracy. For that reason experimental and computational studies complement each other favorably when aiming at a detailed mechanistic understanding at the atomic level, as has been also demonstrated in actinide chemistry [11-13].

In this project two topics relevant to the chemistry of actinides under conditions of a final repository for highly active radioactive waste have been investigated. These are the complexation of actinides with components of pore and ground waters and the adsorption on clay minerals. Complexation with various anionic species present in typical pore waters contributes to the solubility of actinides, which may enhance their distribution by various transport mechanisms. Adsorption at mineral surfaces, on the other hand, is regarded as a major mechanism of retardation.

Small organic acids as complexating ligands of actinides are investigated in this project as they are a major component of the soluble fraction of clay organic matter [14,15]. Besides acetic acid, a major component of soluble clay organic matter and studied already earlier, also formic and lactic acid are treated together with experimentally working project partners. Complexes with U(VI), Np(V), and Am(III) are modelled, covering the most common oxidation states of actinides under natural conditions. For some of these complexes experimentally determined complexation constants are known, but a detailed characterization is largely missing. We systematically determined coordination modes and numbers as well as qualitative complexation energies to characterize the isomer spectrum of these species, to approach a mechanistic understanding of the species itself and their thermodynamic properties. As potential repository clay host rock formations in northern Germany contain pore waters with a considerable salt content [16], we also considered the effect of increased ionic strength on carboxylate complexes and the possible formation of ternary complexes with chlorine for an exemplary case.

Boric acid and its anions, present in sea water [17] and thus also in salt formations and related pore waters to some extent, are also introduced into a final repository as part of the nuclear inventory and by vitrified waste using borosilicate glass [18]. Borates complexation with actinides was only rarely considered prior to this project [19,20]. Borate as a compound of potential interest for the safety of a final repository gained increased interest due to the recent discovery of a very rich chemistry of solid actinide borates [21]. In this consortium, a combined experimental and computational effort is undertaken to close this gap of knowledge. In this project we concentrate on possible actinide borate complexes in solution at low borate concentrations.

Actinide adsorption on minerals has widely been studied experimentally, applying batch and column experiments as well as spectroscopic methods [5,6,22]. Macroscopic experiments

showed that the adsorption depends on the charge of the actinide ion, yielding adsorption at lower pH for higher charged species. Adsorption is further affected by the presence of organic matter or other metal ions in salt solutions [23-28]. Spectroscopic methods like EXAFS, TRLS, and vibrational spectroscopy provide a microscopic view on adsorbed actinide species [7,22,29,30]. Inner- and outer-sphere complexes as well as mono- and polynuclear adsorbates have been identified [5] and may even coexist [31,32]. Preferred mineral surface orientations and their structures in contact with aqueous solution are only scarcely characterized until now [33], especially for clay minerals. Thus, various aspects of the microscopic picture of actinide adsorption at clay mineral surfaces, like the identification of adsorption sites and species are currently a topic of research which is highly relevant to safety aspects of final repositories and a prerequisite for a thorough thermodynamic modeling. In this project we contributed the first systematic computational study of actinide adsorption on clay minerals [34].

2 Project Tasks and Prerequisites

The tasks of this project covered various topics of actinide environmental chemistry pertinent to safety issues of deep geological storage of highly radioactive waste. Actinide complexes as well as adsorption on mineral surfaces have been treated. The investigation on actinide complexes in aqueous solution concentrated on complexes with small carboxylic acids and also ternary complexes including salt anions, which might appear in salt solutions of higher ionic strength. For the first time, actinide borate and organoborate complexes have been treated computationally. The investigation of actinide adsorption on clay mineral surfaces was focused on adsorption at the solvated reactive edge surfaces of smectites.

The tasks and goals of the project were divided into three major parts:

A Complexes in aqueous solution

- **Am(III) in aqueous solution**

The computational modeling of the Am(III) aqua ion and monohydroxide complexes covered some important aqueous species of Am and provided references for other Am(III) complexes and their reactions.

- **Complexation with carboxylic acids**

The goal of this topic was to characterize complexes of the most common oxidation states of actinides, exemplified by U(VI), Np(V), and Am(III), with small carboxylic acids which contribute to the soluble clay organic matter. Besides the commonly studied ligand acetate, formate and lactate are treated. Pertinent questions to be investigated were the isomers, coordination modes, and coordination numbers of these species, which are not easily accessible experimentally. This work contributes to the interpretation of pertinent EXAFS experiments, which is still under discussion [35,36]. A systematic comparison of

thermodynamic trends of these systems also helps to gain a mechanistic understanding beyond effective complexation constants.

- **Complexes in saline solutions**

Effects of finite ionic strength on actinide complexation, which are very rarely explored quantum chemically, are treated for the example of U(VI) acetate in NaCl solution. Long- as well as short-range effects are inspected.

- **Borate complexes**

Actinides borate complexes, which were essentially unknown at the begin of the project, are explored for the first time by quantum chemical calculations, in parallel with corresponding experimental efforts of the project partners to find such complexes. Stability and properties of model complexes are inspected to clarify if they might exist at low borate concentrations. This topic has been extended to borate ester complexes, as these species were suggested by a project partner as experimentally accessible model compounds for other borate complexes.

B Surfaces of clay minerals and adsorbed complexes

- **Clay mineral surfaces**

Earlier studies of the authors on actinide adsorption on neutral clay minerals are extended to the more important class of permanently charged clay minerals in this project. Models of the pertinent minerals montmorillonite and beidellite and their surfaces had to be developed. The project concentrated on the reactive edge surfaces. As a prerequisite of adsorption studies, structures, surface groups, surface energies and the deprotonation of edge surfaces were inspected, providing the background to model actinide adsorption.

- **U(VI) adsorption**

Adsorption of uranyl(VI) on various edge surfaces of model smectite minerals was studied. Pertinent questions to be answered are which adsorption sites exist and which are favorable, how does the adsorption depend on the mineral type, the permanent charge of the mineral, the isomorphous substitutions, the surface orientation, the protonation state of the surfaces, and the adsorbate coverage. To inspect these aspects, structure optimizations of adsorbed U(VI) for various mineral models, surface orientations and sites had to be carried out, as well as a structural and energetic characterization of the adsorption complexes. Besides these substrate related aspects also the coordination number and mode and the possible hydrolysis of the uranyl adsorbates had to be considered, to characterize various possible forms of adsorption complexes.

- **Np(V) adsorption**

Based on the experience with U(VI) the adsorption of Np(V) on a clay mineral was inspected for the first time by quantum chemical methods for the example of montmorillonite the goal to characterize differences and similarities compared to U(VI).

- **Adsorption of salt cations**

As an aspect of the effect of solutions with finite ionic strength on the adsorption of actinides on clay minerals the adsorption of Mg^{2+} and Ca^{2+} ions on model clay minerals was studied. Comparison with results for actinides aimed at gaining insight into a possible competition of actinide and salt cations for adsorption sites.

C Method development

Specific problems of periodic calculations of surface systems are the determination of adsorption energies for charged systems as well as a proper and efficient modeling of surface solvation. In the course of the project various strategies have been explored and promising ones like the estimation of deprotonation energies to calculate adsorption energies and the low temperature partial equilibration to achieve an equilibrated solvent structure have been developed to applicable computational schemes. In addition a PCM variant for surface solvation [37], published during the project time, has been inspected for its applicability to the systems pertinent to this project.

The project tasks included essentially quantum chemical modeling of actinide complexes in aqueous solution and at solvated surfaces. Pertinent challenges of these tasks are a proper treatment of the complex relativistic electronic structure of the actinides involved and to properly account for the solvent environment.

Electronic structure calculations on actinide complexes in solution were carried out by means of density functional methods. The accurate relativistic density functional Douglas-Kroll-Hess method [38,39] was employed in its scalar-relativistic form, as implemented in the parallel high-performance software PARAGAUSS [40] which was developed in our group. For geometry optimizations and energy calculations mainly the GGA functional according to Becke and Perdew (BP) [41,42] was used. Short-range chemical interactions with the aqueous solvent were modeled by explicit aqua ligands of the first coordination shell of the actinide ions [35,43,44]. In addition, a polarizable continuum model (PCM) [45] was used to account for long-range, mainly electrostatic solvation effects.

Surfaces of clay minerals have been modeled as periodic slabs, separated by vacuum space perpendicular to the surface which was chosen more than 1 nm wide, to avoid artificial interactions of neighboring slab instances. In this way, a three-dimensional periodicity of the model is achieved, permitting the application of well established methods for calculating the electronic structure of solids. The electronic structure is calculated by means of density functional theory. In this project the projector-augmented-wave (PAW) method [46,47] instead of pseudo potentials, as implemented in the program VASP (Vienna ab initio simulation package) [47-52], was used to represent the effect of core orbitals including relativistic effects. The valence one-electron wave functions are represented by plane waves augmented by local atomic contributions [53]. The exchange-correlation potential of the

generalized-gradient approximation (GGA) type [54] as suggested by Perdew and Wang (PW91) [55] has been applied. GGA functionals tend to overestimate bond lengths of heavy-element compounds, but provide reliable binding energies [54,56]. Solvation effects on mineral surfaces and adsorption complexes were described by adding one to two layers of water molecules on the surface. In this way at least the first coordination shell of adsorbed actinide species as well as of the mineral surfaces is modeled explicitly. As especially calculated energies depend on the arbitrary structure of the solvation layer, we developed a low temperature dynamic annealing procedure to solve this problem [57]. Alternatively one may apply a fully dynamic treatment, which is computationally rather costly and thus limits considerably the number of systems which can be treated.

A technical prerequisite for the large number of demanding calculations carried out in this project was the application of efficient high-performance software for computers with parallel architecture. For complexes in solution we used the parallel density functional package PARAGAUSS [40] on a local Linux cluster as well as at the high-performance facilities of the Leibniz Supercomputing Centre in Garching. Periodic slab model calculations as models of mineral surfaces have been treated with the parallel version of VASP [47-52], which also was used on local as well as central high-performance facilities. The Linux cluster of the group, used for carrying out the work of the project, comprised about 200 cores during the project time. This local resource was essential for the overall success of the project. More demanding calculations have been carried out at the SuperMuc facility of the Leibniz Supercomputing Centre in Garching, which supported the project with a generous allotment of computer time.

3 Development of the state of the art

In this section the state and development of computational approaches as applied to actinide complexes and adsorption on mineral surfaces is discussed. The developments of pertinent applications can be found in recent reviews [7,34,43,58]. New applied topics covered in this project are especially the complexation of actinides by borate and the adsorption on permanently charged clay minerals, as detailed in Section 4.

The most common though approximate method for quantum chemical modeling of actinide complexes is density functional theory. Relativistic effects are accounted for in most applications by replacing the core orbitals of the actinide atoms by a pseudopotential [59]. As a more accurate alternative efficient scalar-relativistic all-electron methods like the ZORA [60,61] and the Douglas-Kroll-Hess approach [38,39], which is used in this project, are available. Highly accurate four-component relativistic methods and methods including spin-orbit interaction self-consistently [62] are essentially restricted to small molecules due to their computational demand and are mainly necessary when excited states and spectra are considered. For actinide species with an open f-shell also correlation effects are of considerable importance [62]. On the other hand, ground state properties of actinide

compounds are accessible with reliable accuracy with the formally single reference density functional approach with reliable accuracy [63]. Thus, this approach can be regarded as efficient and reliable when more complex species have to be treated.

Modeling of actinide complexes in aqueous solution has to include a proper treatment of the solvent environment. The commonly accepted method to account for solvation effects is the embedding of a complex into a polarizable continuum model (PCM) of the solvent to account for long range electrostatic effects [43,64,65]. Short range chemical effects are covered by including explicit aqua ligands of the first coordination shell of metal centers into the quantum mechanical model. Despite long years of experience and development, PCM is still the a main source of uncertainties of energies when reactions of complexes are modelled [66,67], especially when charged species are involved. This motivates empirical approaches to achieve accurate complexation energies in aqueous solution [66]. More accurate results can be expected from an explicit treatment of the water solvent by periodic models and a fully dynamic approach [68]. This method is restricted in its applicability due to its high computational cost, which motivated approximate explicit models of the QM/MM type [69,70] as well as statistical models of the solvent environment [71] which were inspected recently by our group [72,73]. Albeit absolute solvation energies of charged species are difficult to achieve, relative energies of species and reactions as determined by the PCM approach are often reliable and useful.

As in other fields of surface science, like heterogeneous catalysis, quantum chemical modeling of adsorption is most commonly carried by means of periodic supercell models applying electronic band structure methods. Either pseudopotentials or the PAW approach [46,47] approach are applied to account for the core electrons and related relativistic effects of heavy elements. Solvation effects of minerals in contact with an aqueous solution can be modeled by including a limited number of water molecules into the periodic model. If a complete solvation layer or more is modelled explicitly, this introduces a large number of soft degrees of freedom into the model, making geometry optimization difficult and results, especially energies [57], to some extent dependent on the arbitrary structure of the solvation layer. This problem may be overcome by a dynamical treatment of the system. Due to its computational demand, such an approach for the modeling of actinide adsorption until now is mainly applied at the force-field level [74,75] and only vary rarely quantum mechanically [76,77]. As an efficient alternative we developed a low temperature annealing protocol [57] and applied it successfully to the adsorption of U(VI) and Np(V) on montmorillonite (Section 4.2.1 and 4.2.2). Nevertheless, models with a limited number of water molecules to represent the solvent are approximate, as they cover short-range chemical effects of solvation and miss the long-range electrostatic contributions. For modeling long-range solvation effects on solid surfaces recently the PCM approach has been extended to this class of systems [37]. Despite some successful applications of this method [78,79], our exploratory calculations for U(VI) adsorption at montmorillonite (Section 4.3.2) show also shortcomings of this approach,

Table 1: Gibbs free energy of aqua ligand addition (in kJ/mol) and average bond distances (in pm) to aqua ligands Am-O of the Am(III) aqua ion in water compared to experimental data.

	Ref.	n	ΔG	Am-O
Calc.		6	-8	244
		7	+2	245
		8	-0	247
		9	+20	251
		10		257
Exp.	82	7.4		247
	84	7.6		248
	83	9.6		245
	85	10.1		247

related to missing short-range interactions with the solvent. A combined use, as is commonly done for complexes in solution (see above), has still to be explored.

4 Results

4.1 Actinide Complexes

4.1.1 Am(III) in aqueous solution

The Am(III) aqua ion

The Am(III) aqua ion has been studied as an important reference for various complexes as well as a test case for the performance of the method applied. Interestingly there seem to be until now no accurate quantum chemical calculations for this species, which dominates the Am(III) speciation for $\text{pH} < 5$ [80]. An earlier DFT study employing pseudopotentials only gas phase geometries were determined and energies were corrected for solvation effects in single point fashion [81]. This study suggests a coordination number (CN) of 8 for the Am^{3+} aqua complex, while experimental results suggest values between 7 and 10 [82-85]. By analogy to the lanthanides, which show the same oxidation state, $\text{CN} = 8$ or 9 is expected [86-88].

Our calculated results for Am(III) aqua complexes with 6-10 aqua ligands surrounded by a PCM medium are collected in Table 1. The energies of addition of an aqua ligand are slightly exothermic for $\text{CN} = 6$, endothermic for $\text{CN} = 9$ and close to zero for $\text{CN} = 7$ and 8 . These results are compatible with $\text{CN} = 7-9$, suggesting the coexistence of these coordination numbers. Measured average Am-O distances of 245-248 pm [82-84] fit better to $\text{CN} = 7$ and 8 than to $\text{CN} = 9$. Thus, in agreement with our energy results, the calculated geometries favor the lower part of the experimentally determined interval of 7-10 for the CN of Am(III).

Table 2: Gibbs free energy of aqua ligand addition (in kJ/mol) and geometry parameters^a (distances in pm) of Am(III) monohydroxide in water compared to experimental data.

n	ΔG	Am-O _H	Am-O _w	Am-O _{av}
4	+8	210	249	241
5	+1	213	250	244
6	+6	213	254	248
7	+20	213	258	252
8		218	259	255

^a Bond lengths of hydroxide ligand Am-O_H, bond lengths to aqua ligands Am-O_w, average Am-O bond lengths Am-O_{av}.

Am(III) hydroxide

The first hydroxide species of Am(III), Am(OH)²⁺, is expected in solution at around neutral pH [89]. To the best of our knowledge, this species has been characterized until now neither spectroscopically nor computationally. As the competition between the hydroxide and the aqua ligands suggests a lower CN than for the aqua ion, we modeled Am monohydroxide complexes, including their first solvation shell explicitly, for CN = 4-8 (Table 2). Two structures for each coordination number have been generated by abstracting different protons of the corresponding aqua complex with the same coordination number. The Gibbs free energies of addition of an aqua ligand (Table 2) allow tentatively to exclude the species with CN = 9 and 8. For lower CN small energies of water addition have been calculated, which show no clear trend. Thus, a tendency of lowering of the CN due to bond competition is visible in our results, but a more careful search for isomers for the lower CNs is necessary to determine a reasonable estimate of the coordination number. The structure of the complexes Am(OH)²⁺ is characterized by a short Am-O_H bond of 210-213 pm length and bonds to aqua ligands which are about 10-13 pm longer than in the aqua complexes. Averaging over all Am-O bonds yields distances of 248-255 pm for CN = 6-8 (Table 2), which are by 4-8 pm longer than the corresponding values of the aqua complexes with the same CN (Table 1). Thus, the onset of hydrolysis should be visible in EXAFS experiments at pH values above 5 due to a slight increase of the average Am-O distance.

4.1.2 Complexation with carboxylic acids

Complexation of actinide ions with small carboxylic acids has been inspected as these reactive acids form a part of the soluble organic content of clays, which has been shown e.g. for the relevant formations of Callovo-Oxfordian [14] and Opalinus clay [15]. Acetic acid is the most common one. Formic acid, propionic acid and lactic acids have been found in smaller concentrations [14,15]. As these acids are well known to form complexes with actinides, which contribute to the overall solubility of these elements, we systematically studied complexes for U(VI), Np(V) and Am(III), covering a set of important oxidation states. Our study concentrates on mono- and dicarboxylate complexes, as these species are the more important ones at sour to weakly basic pH conditions and at the low ligand concentrations

Table 3. Complexation energies ΔG (in kJ/mol) of U(VI), Np(V), and Am(III) of mono- and diformate complexes with mono- and bidentate ligand coordination and coordination number CN.

Complex	U(VI)		Np(V)		Am(III)	
	CN	ΔG	CN	ΔG	CN	ΔG
mono	5	-88	5	-32	8/9	-78/-75
bi	5	-81	5	-33	8/9	-72/-70
mono-mono, trans	5	-157	5	-93	8/9	-127/-128
mono-bi, trans	5	-161	5	-86	8/9	-133/-130
bi-bi	5/6	-136/-145	4/5	-81/-77	8/9	-136/-146

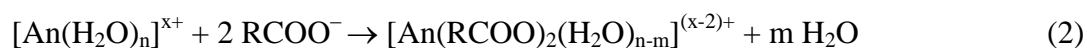
found in clay formations [14, 15]. Available complexation constants refer to these complexes as effective species whose isomers, coordination numbers and structures are commonly unknown. The question of possibly coexisting isomers or varying coordination numbers has not yet been investigated experimentally. With our computational studies we thus contribute to a more detailed knowledge about simple actinide carboxylate complexes, which is a necessary prerequisite for a thorough understanding and prediction of their thermodynamic properties under various conditions.

Comparing the complexation of a set of similar ligands like small aliphatic carboxylic acids, one expects in general similar species and thermodynamic properties for a specific actinide oxidation state, varying essentially with the charge of the metal ion. The complexation strength, as characterized by complexation energies ΔG , should follow the general trend $AnO_2^+ < An^{3+} \leq AnO_2^{2+}$ according to the charges of these actinide ions [90] and assuming a predominantly ionic bonding.

Formiate and Acetate

We calculated model complexes of formiate and acetate, assuming for U(VI) and Np(V) the common equatorial coordination number 5 and inspected coordination numbers of 8 and 9 for Am(III), which are probable ones according to our calculations as well as experimental results and the comparison with lanthanide ions [88] (see Section 4.1.1). Mono- and bidentate coordination modes (Fig. 1) are compared for the carboxylate ligands in mono- and dicarboxylate complexes.

Tables 3 and 4 collect the complexation Gibbs free energies according to the reaction equations



for mono- and dicarboxylate complexes, respectively, with $R = H$ for formiate and $R = CH_3$ for acetate. An represents uranyl(VI), neptunyl(V), and Am(III) ions with charges $x = 2, 1,$ and $3,$ respectively. n is the number of aqua ligands of the actinide ions, 5 for the actinyls and

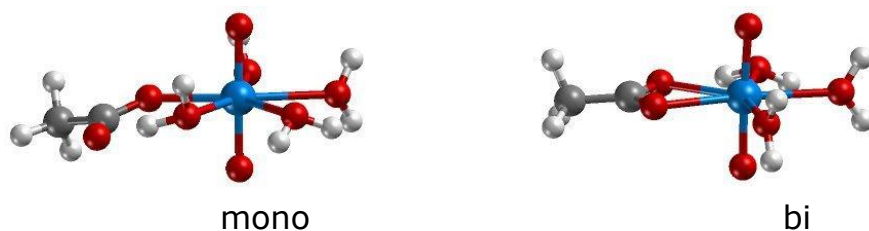


Figure 1: Uranyl(VI) monoacetate with monodentate (mono) and bidentate (bi) ligand coordination

Table 4. Complexation energies ΔG (in kJ/mol) of U(VI), Np(V), and Am(III) of mono- and diacetate complexes with mono- and bidentate ligand coordinations and coordination number CN.

Complex	U(VI)		Np(V)		Am(III)	
	CN	ΔG	CN	ΔG	CN	ΔG
mono	5	-98	5	-51	8/9	-90/-82
bi	5	-99	5	-45	8/9	-105/-86
mono-mono, trans	5	-178	5	-99	8/9	-143/-143
mono-bi, trans	5	-176	5	-99	8/9	-150/-137
bi-bi	5/6	-166/-176	5/6	-95/-71	8/9	-160/-156

8 or 9 for Am(III), and m designates the number of aqua ligands replaced by carboxylates, where a monodentate coordinated ligand contributes 1 and a bidentate coordinated one 2.

The complexation energies for formate follow the effective charges of the actinide ions (Table 3). The largest energies are calculated for U(VI), slightly lower ones for Am(III) and considerably lower ones for Np(V), for both, mono- and diformate complexes. U(VI) monoformate shows a slight preference for monodentate ligand binding, confirming earlier calculations and an EXAFS experiment of the project partner Helmholtz-Zentrum Dresden-Rossendorf [91]. The same trend is calculated for Am(III), independent of the coordination number, while mono- and bidentate coordinated monoformate complexes of Np(V) are degenerate. These trends do not hold always for the dicarboxylates. For U(VI) diformate isomers with one or two monodentate coordinated ligands are preferred compared to a species with two bidentate ligands, even if one takes into account that the small bite angle of the carboxyl group allows an increase of the coordination number of this complex from 5 to 6 (Table 3). For Np(V) we find a preference for monodentate formate binding, while for Am(III) there is a weak tendency to bidentate coordination.

Acetate complexes yield in general a little higher complexation energies than formate complexes (Table 4). This trend is in line with the higher proton binding of acetic acid ($pK_a = 4.8$) compared to formic acid with a pK_a of 3.8. Again, comparison of U(VI), Am(III), and Np(V) complexes shows that the complexation energies follow the effective charges of the

Table 5. Ranges of complexation constants $\log\beta_n$ of U(VI), Np(V), and Am(III) formate and acetate complexes with one and two ligands from various experiments.^a

Complex	U		Np		Am	
	$\log\beta_1$	$\log\beta_2$	$\log\beta_1$	$\log\beta_2$	$\log\beta_1$	$\log\beta_2$
formate	1.6 ^b -1.9 ^c	2.6 ^b -3.1 ^c	-	-	2.54 ^h	4.02 ^h
acetate	2.4 ^d -2.9 ^e	4.1 ^c -5.5 ^e	1.0 ^f -1.9 ^g	1.6 ^f -3.1 ^g	1.8 ^h -2.4 ^h	3.2 ^h -3.8 ^h

^a References to largest and smallest values are given. ^b Ref. 95. ^c Ref. 96. ^d Ref 97. ^e Ref 98. ^f Ref. 99. ^g Ref. 100. ^h Ref. 80.

actinide ions, being highest for U(VI), slightly lower for Am(III) and considerably lower for Np(V). The results collected in Table 4 show for U(VI) monoacetate that mono- and bidentate complexes are energetically degenerate. Also for the diacetate, all combinations of mono- and bidentate ligand coordination yield about the same stability. EXAFS experiments have been interpreted to show bidentate coordination for U(VI) acetate [36,92,93] and are supported by IR measurements [36], which have been complemented by density functional calculations. Hints for monodentate acetate coordination in fresh probes [93], which convert with time to bidentate coordination, support our finding that complexes with these two coordination modes are close in energy. For the U(VI) diacetate with bidentate ligand coordination a change of the coordination number from 5 to 6 is favorable, due to the small bite angle of the carboxyl group. For Np(V) there is a more clear trend to monodentate coordination, for mono- as well as diacetate (Table 4), in disagreement with the results of an EXAFS experiment (see also below) [94]. Am(III), on the other hand, shows a clear preference for bidentate acetate binding, independent of the coordination number and in agreement with a recent EXAFS experiment of the project partner Universität Heidelberg [83]. According to our results, acetate tends more to bidentate coordination than formate.

Comparison of calculated and experimental complexation energies is hampered by an overestimation of calculated reaction energies, which is most probable due to the comparison of results achieved by a polarizable continuum model for species of varying charge. Nevertheless, calculated relative complexation energies for formate and acetate as well as all three actinide ions treated should be well comparable with trends found experimentally, as this error should cancel out. To compare our results we collected ranges of experimentally determined stability constants $\log\beta_1$ and $\log\beta_2$ (Table 5) [80,95-100]. Only results for actinide formate and acetate complexes in perchlorate solutions of low ionicity have been taken into account. The results for acetate follow the effective charge of the actinide ions, yielding results for $\text{NpO}_2^+ < \text{Am}^{3+} < \text{UO}_2^{2+}$ in good agreement with our calculated results (Table 3). Only for Am(III) monoacetate with CN = 8 we obtain a complexation energy which slightly exceeds the one of U(VI) monoacetate, while the experimental results yield a lower one. This experimental trend for monoacetate is reproduced by our results for CN = 9. For formate, in line with the calculated results, lower complexation constants compared to acetate have been measured than for U(VI) (Table 5). While our calculations yield also lower complexation energies for Am(III) formate, the experimental values for Am formate complexes are

Table 6. Geometry parameters^a of U(VI), Np(V), and Am(III) formate (Fo) complexes (in pm) with mono- and bidentate ligand coordination and coordination number CN.

Complex		CN	An-O _t	An-O _c	An-O _w	An-O _{av}	An-C
U(VI) aqua		5	179.1		245	245	
U(VI)Fo	mono	5	180.2	231	247	244	340
	bi	5	179.9	244	243	244	282
U(VI)Fo ₂	mono-mono, trans	5	181.2	236	248	243	342
	mono-bi, trans	5	181.1	232/247	244	243	343/284
	bi-bi	5	180.4	245	248	246	283
		6	180.7	249	251	250	287
U(VI)Fo ₃	mono-mono-mono	5	182.1	237	247	241	346
	bi-bi-bi	6	181.6	250		250	287
Np(V) aqua		5	183.3		255	255	
Np(V)Fo	mono	5	183.5	250	260	258	346
	bi	5	183.8	254	258	256	289
Np(V)Fo ₂	mono-mono, trans	5	185.0	251	255	252	351
	mono-bi, trans	5	184.7	251/255	254	254	350/290
	bi-bi	5	184.8	257	256	256	292
	bi-bi	4	184.4	254		254	289
Am(III) aqua		8			247	247	
		9			251	251	
Am(III)Fo	mono	8		238	252	250	339
	mono	9		243	254	252	344
	bi	8		249	253	252	285
	bi	9		250	252	252	286
Am(III)Fo ₂	mono-mono, trans	8		246	252	250	346
	mono-mono, trans	9		246	255	253	344
	mono-bi, trans	8		251/245	254	252	345/288
	mono-bi, trans	9		251/248	256	254	348/287
	bi-bi, trans	8		251	250	251	287
	bi-bi, trans	9		252	254	253	288

^a Actinyl bond length An-O_t, bond to carboxyl oxygen An-O_c, averaged bond to aqua ligands An-O_w, average over An-O bond to all ligands An-O_{av}, distance to carboxyl carbon An-C.

comparable to the highest values measured for acetate. These complexation constants are also higher than for U(VI) formates, in contrast to the calculated results for Am formate complexes. For these reasons we regard the complexation constants for Am formate to be too high.

For the discussion of calculated geometries of An carboxylate complexes in relation to experimental results, a corresponding view on the performance of DF calculations for the aqua complexes of the actinide ions is helpful as a guideline. A direct comparison to experiment shows for the actinide aqua complexes that GGA calculations, as usual, tend to slightly overestimate bond lengths compared to EXAFS results. For the uranyl(VI) aqua

complex with the established CN of 5 the uranyl bond length of 179 pm (Table 6) is calculated, slightly larger than the experimental values of 176-178 pm [36,93,101]. The calculated average equatorial bond length $U-O_{av}$ of the aqua ligands of 245 pm (Table 6) exceeds the experimental results of 240-241 pm [36,93,101] by about 4 pm. The neptunyl(V) aqua complex with five aqua ligands shows an actinyl bond length of 183 pm, in good agreement with the varying experimental determinations of 182-185 pm [94,101-103]. On the other hand, $Np-O_{av}$ of 255 pm again overestimates the EXAFS results of 249-252 pm [94,101-103] by a few pm. Although our calculated average $Am-O_w$ distances fit better to experiment for CN = 7 and 8 than for CN = 9 and also consideration of dehydration energies supports a slightly lower CN (see Section 4.1.1), the common overestimation of $An-O_w$ distances in other calculations suggests CN = 8 and 9 as most reasonable coordination number for Am(III).

Structures of actinide mono- and diformate complexes are compared for U(VI), Np(V), and Am(III) in Table 6. The actinyl bond lengths of U(VI) and Np(V) complexes increase due to complexation slightly, by about 1 pm per ligand. This effect is a little stronger for U(VI) than for Np(V), in line with the higher complexation energies for U(VI). Actinide-carboxyl bonds $An-O_c$ are shorter for mono- than for bidentate carboxyl coordination as the essentially ionic attraction between these two species is distributed over two coordinative bonds in case of bidentate coordination. $An-O_c$ bonds of monodentate coordinated ligands are shorter than the bonds to aqua ligands, $An-O_w$, while the $An-O_c$ bond lengths of bidentate coordinated formate are rather similar to $An-O_w$ (Table 6). Average $An-O_{av}$ distances, as often measured by EXAFS, vary by a few pm at most, showing no clear trend in dependence of the number of formate ligands. The known trend of $An-O_{av}$ to increase with the CN [35,104] and to be independent of the coordination mode is confirmed for the U(VI) and Np(V) complexes where different CN have been inspected (Table 6). For Am(III) species with CN = 8 and 9 this effect is small, up to 4 pm at most. Thus, $An-O$ distances do not provide easily detectable signatures to discriminate the formate coordination mode. The only geometrical feature which clearly reflects the ligand coordination mode is the $An-C$ distance. For bidentate ligands it amounts to about 280-290 pm, while longer distances of about 340 to 350 pm are calculated for monodentate coordinated ligands (Table 6). There are small variations of $An-C$ distances for the three actinide ions inspected. The smallest values are determined for U(VI) and the longest for Np(V) while Am(III) tends to show intermediate results.

In a combined IR and computational study [91] the coordination of formate to U(VI) was identified to be preferentially monodentate, based on the analysis of vibrational frequencies of the carboxyl group. EXAFS results of the same study yield a $U-O_t$ bond length of 177 pm and an equatorial $U-O$ distance of 239-241 pm, showing a weak tendency to decrease with increasing pH. These values are in good agreement with our results (Table 6) for the energetically preferred monodentate coordination of formate. If only monodentate formate coordination is considered, we also found a weak trend of decreasing $An-O_{av}$ from 245 pm for the U(VI) aqua ion to 244 pm for monoformate, to 243 pm for diformate and

Table 7. Geometry parameters^a of U(VI), Np(V), and Am(III) acetate (Ac) complexes (in pm) with mono- and bidentate ligand coordination and coordination number CN.

Complex		CN	An-O _t	An-O _c	An-O _w	An-O _{av}	An-C
U(VI) aqua		5	179.1		245	245	
U(VI)Ac	mono	5	180.5	229	247	243	341
	bi	5	180.2	242	246	244	283
U(VI)Ac ₂	mono-mono, trans	5	181.6	232	250	243	342
	mono-bi, trans	5	181.4	233/246	245	243	338/286
	bi-bi	5	181.1	243	249	244	283
		6	181.4	247	253	249	287
U(VI)Ac ₃	mono-bi-bi	5	182.4	225/246		242	342/285
	bi-bi-bi	6	182.2	248		248	288
Np(V) aqua		5	183.3		255	255	
Np(V)Ac	mono	5	183.7	251	256	255	345
	bi	5	184.4	253	256	255	291
Np(V)Ac ₂	mono-mono, trans	5	185.2	250	254	252	352
	mono-bi, trans	5	185.2	247/255	254	253	347/292
	bi-bi	5	185.4	254	257	254	291
	bi-bi	6	185.4	258	261	259	295
Am(III) aqua		8			247	247	
		9			251	251	
Am(III)Ac	mono	8		236	250	248	343
	mono	9		242	253	252	343
	bi	8		245	253	251	284
	bi	9		249	256	254	288
Am(III)Ac ₂	mono-mono, trans	8		241	254	251	342
	mono-mono, trans	9		248	256	254	349
	mono-bi, trans	8		245/249	253	251	349/286
	mono-bi, trans	9		245/251	257	255	352/287
	bi-bi, trans	8		249	251	250	287
	bi-bi, trans	9		250	256	254	289

^a Actinyl bond length An-O_t, bond to carboxyl oxygen An-O_c, averaged bond to aqua ligands An-O_w, average over An-O bond to all ligands An-O_{av}, distance to carboxyl carbon An-C.

finally to 241 pm for the triformate complex with CN = 5. As such a trend is not observed for the other actinides inspected (Table 6), this agreement with experiment has to be taken with due caution. To the best of our knowledge, no structural information is available for Np(V) formate complexes in the literature. In the course of this project, our project partner University of Heidelberg planned an EXAFS experiment on Am(III) formate, which will be carried out with our support in the end of 2016.

Calculated structures of actinide acetate complexes yield a rather similar picture as for formate (Table 7). Actinyl bond lengths increase by about 1 pm per coordinated acetate

ligand. An-O_c bond lengths are considerably shorter than An-O_w bonds for monodentate coordination and similar to An-O_w for bidentate coordination. This tendency is more pronounced for U(VI) than for Np(V) (Table 7). Average equatorial An-O bond lengths An-O_{av} are independent of the ligand coordination mode. They increase with the coordination number. Again, this trend is nicely seen even for the small change from CN = 8 to CN = 9 for Am(III) (Table 7). An-C distances of 280-290 pm for monodentate coordinated ligands and of 340-350 pm for bidentate coordinated ligands (Table 7) are the only trustworthy geometrical feature to discriminate the coordination modes experimentally, as for formate. Structural differences between formate and acetate complexes are small. In line with the higher ligand binding energy of acetate (Tables 3 and 4), the actinyl bonds of acetate complexes are by 0.2 to 1 pm longer and the An-O_c bonds by 1-4 pm shorter than for formate complexes (Tables 6 and 7).

According to various experiments the coordination of acetate to U(VI) is regarded as bidentate, which is best confirmed by measured short U-C distances of about 290 pm in EXAFS experiments [36,92,93] and the splitting of symmetric and asymmetric vibrational modes of the carboxyl group of acetate [36,105], as determined in IR experiments. Thus, we preferentially compare our calculated geometries of species with bidentate coordination to EXAFS results. Calculated U-O_t bond lengths of 179-182 pm for complexes with 0-3 acetate ligands are as usual somewhat longer than the corresponding EXAFS results of 176-179 pm [36,92,93]. Only in one of these experiments the expected increase of the uranyl bond lengths with increasing number of acetate ligands is obtained [36], in agreement with our computational results. U-O_{av} has been measured to 241-247 pm [36,92,93]. While in one of these studies no correlation of U-O_{av} with increasing pH is seen [93], another reports an increase of U-O_{av} from 241 to 247 pm when the number of ligands increases from 0 to 3 [36]. This result agrees with our calculated values of 242-245 pm for species with CN = 5 and 248-249 pm for species with CN = 6 (Table 7) if an increase of the CN with increasing number of ligands is assumed, which is supported by our calculated complexation energies. Calculated U-C distances of 283-288 pm with smaller values for CN = 5 and longer ones for CN = 6, are regarded to be in good agreement with EXAFS results, taking into account that this distance is not a direct bond. In Ref. 92 U-C distances of 291-287 pm, decreasing with increasing pH, are reported. Although the absolute values are close to the calculated results, this finding is in contrast to an expected slight increase of U-C assuming an increase of CN with increasing number of ligands (Table 7). Other studies report U-C distances of 288 to 292 pm, with no clear trend with increasing number of acetate ligands [36,93]. There are speculative interpretations of aging effects observed for U(VI) acetate solutions [93] to point towards initially monodentate complexes which change with time to bidentate ones. Taking into account the small energy differences calculated here (Table 4) that does not seem impossible and might be a hint on the coexistence of various isomers. Thus, although U(VI) acetate can be regarded as a well studied system, there are still open questions like the preferred

coordination number of various species and the possible coexistence of isomers, as suggested by our calculations, which are a challenge for future experiments.

For Np(V) acetate only a single EXAFS experiment carried out by our project partner Helmholtz-Zentrum Dresden Rossendorf is available [94]. At low pH the bond length of the neptunyl aqua complex has been determined to 183 pm, in very good agreement to our result of 183 pm. With increasing pH the Np-O_t bond length increases due to coordination of acetate ligands to 185 pm for a solution with about 50% contribution of the triacetate species. Also this increase parallels nicely the calculated results, which show an increase of Np-O_t of 2 pm for the diacetate complex. An-O_{av} is measured independent of the pH to 251 pm, thus somewhat shorter than the calculated results of 256 and 257 pm for the bidentate coordinated mono- and diacetate complexes (Table 7). This confirms our general result of the independence of An-O_{av} from the number of acetate ligands [35,104]. In contrast to our complexation energies (see above), bidentate acetate coordination is inferred from the EXAFS results by fitting a weak feature as a Np-C distance of 290-293 pm [94], which is in very good agreement with our calculated result of 291 pm for bidentate complexes (Table 7). Taking into account the weakness of this EXAFS feature compared to Np(VI) [94], the calculated weak preference of Np(V) acetate complexes for monodentate coordination, as well as the very small calculated geometry differences for An-O_t and An-O_{av} between mono- and bidentate coordinated complexes (Table 7), a contribution of both complexation modes seems most plausible. Further investigations, favorably by vibrational spectroscopy, are necessary to clarify this issue.

The structure of Am(III) acetate complexes has recently been inspected by our project partner Universität Heidelberg by means of EXAFS [83]. Spectra measured from pH = 1 to pH = 6 reflect the formation of Am acetate species with up to three ligands. For pH = 6 still Am diacetate is the dominating species according to speciation calculations [83]. Average Am-O bond lengths of 247 pm increasing to 249 pm together with a CN of 10 have been measured. These bond lengths are as usual shorter than our calculated ones of 250 to 254 pm for the preferred bidentate acetate coordination for CN = 8 and 9. Compared to the Am aqua ion we calculated an increase of Am-O_{av} of about 3 pm due to acetate coordination, which is in line with the increase of 2 pm comparing the EXAFS spectra at low and higher pH [83]. Bidentate acetate coordination is identified in the measurements by resolving an Am-C distance of 278-284 pm, which is in reasonable agreement with the calculated values for bidentate ligand coordination of 284-289 pm. For all geometry parameters we obtained a tendency to increase with increasing CN, thus there is a marginally better agreement with experiment for CN = 8 than for CN = 9 (Table 7). Overall, our relative energies and EXAFS results agree on bidentate acetate coordination for Am(III) and also the geometry parameters of the complexes coincide satisfactorily with the experiment. The only uncertainty left is the preferred coordination number of Am(III) acetate complexes. Our model assumption of CN =

8 or 9 is in agreement with the experimental result of 10 ± 2 and an increase of the CN in the model calculations would worsen the agreement of geometry parameters with experiment.

In most cases our calculated preferred species agreed with experimental determinations although our energy results show that one has to consider an equilibrium of isomers and different coordination numbers in general. As various isomers of actinide carboxylates will have at least a little different thermodynamic properties, this aspect seems to be of interest when for a thorough and transferable thermodynamic modeling of actinide complexation.

Lactate

Lactate complexes have been studied as lactic acid forms a common small organic ligand present in clay organic matter [14,15]. This ligand is also of interest as an exemplary case of the α -hydroxy carboxylic acids, which offer more complexation modes to metal ions than aliphatic monocarboxylic acids. Besides mono- and bidentate coordination to the carboxyl group also chelate complexation involving in addition the hydroxyl group are possible (Fig. 2). Open questions are the mode of complexation as well as a possible a deprotonation of the hydroxyl group due to complexation, as suggested in contrast to earlier work by a recent work of the project partner Helmholtz-Zentrum Dresden-Rossendorf on Am(III) and Eu(III) lactate [106]. We concentrate our calculations on U(VI) and Np(V) monolactate as the most relevant complexes at low concentrations and considered also some structural models of U(VI) dilactate.

Calculated complexation energies of U(VI) monolactate for various ligand coordination modes show that monodentate, bidentate, and chelate coordination are essentially degenerate with a weak tendency to twofold coordination of the ligand (Table 8). In agreement with the lower pK_a of lactic acid of 3.9 compared to acetic acid ($pK_a = 4.8$), the complexation energies of about 65 kJ/mol are lower than for acetate, where about 100 kJ/mol have been obtained (Table 4). On the other hand, measured complexation constants $\log\beta_1$ of lactate of 2.4-3.4 are comparable with the ones obtained for acetate, $\log\beta_1 = 2.4-2.9$ [107]. This apparent disagreement might be explained by three energetically degenerate isomers of U(VI) lactate compared to two for acetate, which increases the effective complexation constant of lactate. A possible deprotonation of the OH group of the chelate U(VI) monolactate complex requires 62 kJ/mol and thus is improbable at acidic conditions. This finding is in contrast to a recent NMR and IR study, supported by calculations of vibrational frequencies, on Eu(III) monolactate [106], but agrees with an earlier suggestion based on TRLFS [108]. Taking into account that the effective charge of the Eu(III) ion should be comparable or even marginally smaller than the one of U(VI) [90], a deprotonation of the hydroxyl group of monolactate complexes is regarded as improbable. For U(VI) dilactate we calculated various coordination modes of the two ligands to be rather close in energy, with a slight preference for species with at least one monodentately coordinated ligand (Table 8).

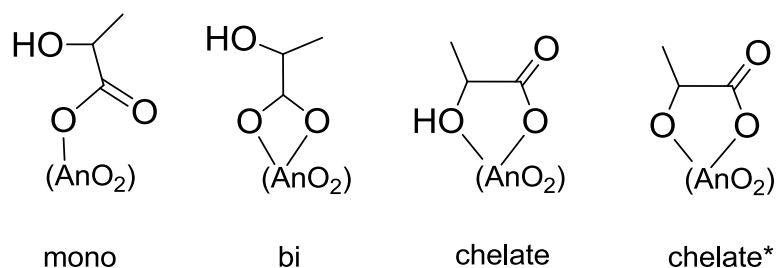


Figure 2: Complexation modes of lactate to actinyl ions: Monodentate (mono), bidentate (bi), chelate and chelate with deprotonated hydroxyl group (chelate*).

Table 8: Gibbs free energy of lactate complexation (kJ/mol) for various coordination modes^a of U(VI) and Np(V) with an equatorial coordination number of 5.

Species	Coordination	U(VI)	Np(V)
AnLac	mono	-63	-17
	bi	-65	-28
	chel	-67	-18
	chel*	-5	+112
AnLac ₂	mono-mono, cis	-120	
	mono-bi, trans	-126	
	mono-chel, trans	-123	
	bi-bi	-110	
	bi-chel	-102	
	chel-chel	-114	

^a Coordination modes: mono = monodentate, bi = bidentate, chel = chelate, chel* = chelate, deprotonated.

Qualitatively similar results are obtained for the complexation energies of Np(V) monolactate. The energies for various complexation modes of about 20-30 kJ/mol (Table 8) are again considerably below the values obtained for acetate of about 50 kJ/mol (Table 4), in line with the lower pK_a of lactic acid compared to acetic acid (see above). In contrast to U(VI) there is a weak preference of about 10 kJ/mol for bidentate coordination for Np(V) (Table 8). Reported complexation constants logβ₁ for Np(V) lactate of 1.4-2.0 tend to be larger than for acetate (logβ₁ = 0.7-2.0) [107], which was recently confirmed by our project partner INE Karlsruhe. This disagreement can most probably not be resolved by a differing number of isomers for lactate and acetate, as the calculated complexation energies for various isomers differ more than for U(VI) (Tables 4 and 8). Thus, the qualitative disagreement between the calculated complexation energies and measured complexation constants for lactate and acetate for Np(V) as well as for U(VI) needs further consideration. Due to the lower charge of neptunyl(V) compared to uranyl(VI) the deprotonation of the hydroxyl group of the monolactate complexes is even more improbable for Np(V) (Table 8).

Table 9: Geometry parameters^a of U(VI) and Np(V) lactate complexes (in pm) for various coordination modes^b with an equatorial coordination number of 5.

Species		An-O _t	An-O _c	An-O _w	An-O _{eq}	An-C	An-C _d
UO ₂ Lac	mono	180	231	246	243	337	467
	bi	180	244	244	244	283	435
	chel	180	238	246	243	342	454
	chel*	183	228	253	243	327	431
Exp. ^c		177		239	352		
NpO ₂ Lac	mono	184	245	256	254	343	476
	bi	184	256	256	256	293	445
	chel	184	250	258	255	345	482
	chel*	186	241	263	254	327	395

^a Actinyl bond length An-O_t, bond to carboxyl oxygen An-O_c, averaged bond to aqua ligands An-O_w, average over equatorial An-O bonds to all ligands An-O_{eq}, distance to nearest carboxyl carbon An-C and to distant carboxyl carbon An-C_d. ^b Coordination modes: mono = monodentate, bi = bidentate, chel = chelate, chel* = chelate, deprotonated. ^c Ref. 109.

Structural parameters of U(VI) and Np(V) monolactate complexes, supporting our energy results, are collected in Table 9. Actinyl bond lengths of 180 pm for U(VI) and 184 pm for Np(V) are by 1 pm longer than for the corresponding aqua complexes, as for other carboxylates (Tables 6 and 7). Only for the twofold deprotonated ligand an increase by about 3 pm is calculated, in line with the stronger interaction due to the higher charge of that ligand. The weak variation of the actinyl bond lengths for singly deprotonated lactate reflects the near energetic degeneracy of various coordination modes. Monolactate provides again an example showing that the commonly measured average equatorial An-O distance An-O_{eq} is essentially independent of the coordination mode, which is valid even for the twofold deprotonated lactate ligand (Table 9). Thus, as for other carboxylates, An-C is the only commonly measured geometry parameter appropriate for differentiation of coordination modes. It is short, about 280 pm and 290 pm for U(VI) and Np(V), respectively, for bidentate coordination, and about 330 - 345 pm or longer for the other coordination modes (Table 9). Comparison with the only available EXAFS result for U(VI) lactate [109] shows the typical overestimation of U-O_t in our calculations. U-O_{av} with 239 pm is measured a little shorter than for acetate (see above) in agreement with our calculated values of about 243 pm, which are also slightly shorter than for acetate (about 246 pm, Table 7). Comparison of the measured U-C distance of 352 pm with our results excludes definitely bidentate coordination and is best comparable with the chelate coordination, calculated at 342 pm. This result can be compared tentatively also to an EXAFS experiment of our project partner Universität Heidelberg on Am(III) lactate [110], where independent of the pH Am-C = 341-343 pm and the second nearest Am-C distance Am-C_d of 432-436 pm have been measured. Although the radius of Am(III) is by about 25 pm larger than for U(VI) [111], we demonstrated for acetate, that An-C distances for both actinide ions are comparable (Table 7). Thus, due to An-C bidentate coordination can also be excluded for Am(III) although the measured An-C_d fits to the lower

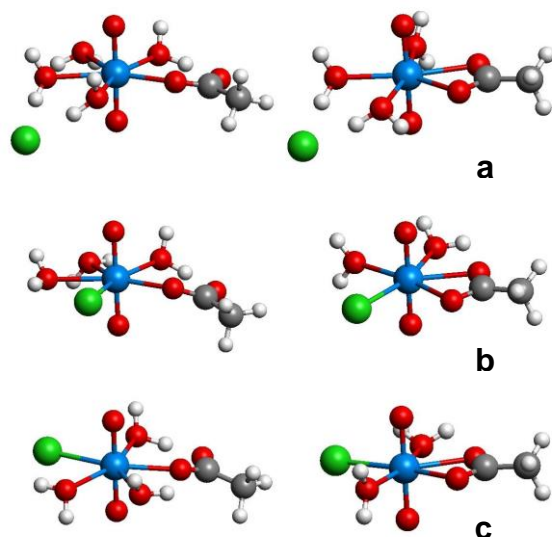


Figure 3. Structures of ternary uranyl(VI) acetatochloride complexes: a) chloride outer sphere b) chloride inner sphere cis c) chloride inner sphere trans. Left and right columns show complexes with mono- and bidentate acetate coordination, respectively.

values calculated (Table 9). Taking into account the relatively large uncertainty of this latter long distance as well as the relatively similar distances calculated for various coordination modes (Table 9), a differentiation of coordination modes based on $An-C_d$ seems to be not trustworthy.

4.1.3 Acetate in saline media: Ternary acetato chloride complexes

The formation of and the equilibria between complexes are modified in saline media due to modified solvent properties as well as due to direct interactions with dissolved ions of the salt compared to a pure water solvent environment. At the macroscopic scale these effects are accounted for in a cumulative way by activity coefficients [1,112], which are determined by the purely electrostatic Debye-Hückel model [113] at very low salt concentrations and by more sophisticated models (SIT, Pitzer) [114,115] at higher concentrations. The basic phenomena at the microscopic level may be divided into effects due to changes of the solvent properties and direct interactions with salt ions. The first group essentially includes the stabilization of charged complexes in the field of counter ions of the saline medium and the lowering of the dielectric constant of aqueous solutions with increasing ionicity as a result of the lower orientational polarizability of water in the solvation shell of salt ions.

For the complexation of actinide ions by anionic ligands commonly a slight decrease of the complexation constant at very low ionicity followed by an increase with increasing ionicity is observed [107,116]. The first effect arises due to the stabilization of the reactant ions by counter ions of the solution, as described by the Debye-Hückel model [113]. The latter one stems from the decreasing solvation energy of the reactants due to the lowering of the dielectric constant of the saline medium with increasing salt concentration.

In this project we inspected two effects of salinity on the complexation equilibria of actinide complexes, the lowering of the dielectric constant as well as the possibility of direct interactions with the salt ions, which may lead to new equilibria and species in the system. As

Table 10. Calculated geometry parameters^a (in pm) of ternary uranyl monoacetate monochlorate complexes $\text{UO}_2\text{CH}_3\text{COOCl}(\text{H}_2\text{O})_n$ with CN = 5 with mono- (mono) and bidentate (bi) acetate and outer sphere (out) as well as inner sphere cis and trans chloride coordination. Energies ΔG of chloride coordination according Eq. 3 (in kJ/mol).

Complex		U-O _t	U-Cl	U-O _c	U-O _w	U-O _{eq}	U-C	ΔG
acetate	mono	180.5		229	247	243	341	
	bi	180.2		242	245	244	283	
	exp. ¹⁸	177				241		
acetatochloride								
	mono out	180.7	442	229	247	244	340	-66
	bi out	180.4	446	242	244	244	283	-65
	mono cis	181.1	270	231	251	246	338	-60
	mono trans	181.0	271	237	249	246	341	-66
	bi cis	180.9	269	244	247	246	284	-65
	bi trans	180.9	270	244	247	245	284	-72

^a Uranyl bond length U-O_t, bond lengths of chlorine ligand U-Cl, bond to carboxyl oxygen U-O_c, averaged bond to aqua ligands U-O_w, average over U-O bond to all ligands U-O_{eq}, distance to nearest carboxyl carbon U-C.

an exemplary and well studied system of relevance in this cooperative project we have chosen the complexation of uranium(VI) with acetate in a NaCl solution.

To inspect the possible formation of ternary acetatochloride complexes we chose model monoacetate complexes $\text{UO}_2\text{CH}_3\text{COO}(\text{H}_2\text{O})_n$ with CN = 5 and mono- ($n = 4$) and bidentate ($n = 3$) acetate coordination and exchange an aqua ligand by a chloride ion to form an inner sphere chlorate complex. For comparison also outer sphere coordination of the chloride ion to the aqua ligands of the acetate complexes is considered. The complexation energies of chloride coordination according to the reaction



are rather similar for various types of acetatochloride complexes (Table 10). Chloride binds in outer sphere fashion to a monoacetate complexes with about 65 kJ/mol. Inner sphere complexes with chloride in trans position are marginally more stable for bidentate acetate coordination (72 kJ/mol) and comparable for monodentate acetate coordination (Table 10). Thus, our model calculations show that the formation of ternary acetatochloride complexes seems to be thermodynamically possible. This complexation has to be regarded as weak, as isomers with inner and outer sphere chloride complexation are energetically close. Interestingly, the equilibrium between isomers with mono- and bidentate acetate coordination is shifted towards bidentate coordination due an inner sphere chloride ligand. The energy difference between bi- and monodentate isomers amounts to 1 kJ/mol in favor of bidentate coordination for monoacetate and increases to 6 kJ/mol for the ternary complexes with chloride in the trans position (Table 10).

Table 11. Comparison of ΔG (in kJ/mol) of coordination of acetate in mono- (mono) or bidentate (bi) fashion and chloride as outer (out) or inner sphere (in) ligand in cis or trans position to a uranyl(VI) monoacetate complex with bidentate acetate coordination.

Complex ^a		CN = 5	CN = 6
acetate	mono-mono	-79	
	mono-bi	-77	-60
	bi-bi	-67	-77
chloride			
	out	-65	
	in cis	-65	
	in trans	-72	

To inspect the long range effect of the decreasing dielectric constant ϵ of salt solutions of increasing ionicity, we compared complexation energies calculated with $\epsilon = 78.4$ for a pure water solvent to results obtained with $\epsilon = 60$, corresponding to a 2 M NaCl solution [117]. In line with experimental observations [107], the increased salt concentration increases the energies of anionic ligand coordination to cationic complexes due to lower solvation energies of charged species. For the formation of monoacetate and monochloride complexes of uranyl, where the charge of the complex lowers from +2 to +1 an increase of 8 kJ/mol is calculated. For the reaction of uranyl monoacetate to acetatochloride or diacetate, where the charge of the complexes changes from +1 to 0, we determine an increase of only 2 kJ/mol.

In Table 10 we compare geometry parameters of ternary uranyl acetatochloride complexes to uranyl monoacetate. The effect of outer sphere coordination of chloride is marginal, as expected, not exceeding 0.4 pm for any parameter. Due to inner sphere coordination the terminal uranyl bond U-O_t is elongated by 0.5 to 0.7 pm due to the stronger donating capability of chloride compared to an aqua ligand. The U-Cl bond in the monodentate acetate complex of about 270 pm is by nearly 2 pm longer than in the bidentate isomer, inline with the lower chloride complexation energies of this species. Both U-O bonds to acetate as well as to aqua ligands elongate slightly due to the bond competition with the chloride ion. As a result the average equatorial U-O distance U-O_{eq} increases by about 2 pm for the inner sphere complexes. Comparably small changes are calculated for the U-C distance (Table 10). Thus, inner sphere chloride coordination yields only small changes of the geometry of the complexes compared to monoacetate, which make a direct identification by EXAFS very challenging, taking also into account that several isomers might coexist.

To shed some more light on the question if ternary uranyl(VI) acetatochloride complexes might exist, we compare calculated model reaction energies of the formation of acetatochloride and diacetate taking bidentate monoacetate as reactant (Table 11). A second acetate ligand is bound by up to about 80 kJ/mol to monoacetate and all variants of mono- and bidentate acetate coordination are calculated to be essentially degenerate if one considers also

six-fold coordination in the case of bidentate acetate coordination of both ligands. These energies are a little larger than for chloride coordination, which amounts to 72 kJ/mol for the most favorable isomer with bidentate acetate coordination and chloride in trans position (Table 11). Thus, while thermodynamically possible, the formation of ternary acetatochloride complexes is most probable in chloride solutions at low acetate concentrations comparable to the uranium concentration. These conditions can be fulfilled in saline pore waters with rather low organic content.

4.1.4 Borate and Boratester complexes

Borate may contribute to actinide complexation under final repository conditions and influence actinide mobility [19,20]. It is introduced to repositories as part of the nuclear inventory and by borosilicate glasses used to immobilize and dispose hazardous waste [18]. Borate is also a minor component of sea salt and thus present in salty ground waters, as they are found e.g. in deep clay formations of northern Germany [17]. At the beginning of the project no studies on actinide borate complexes were available and also the complexation with other metal ions has been studied only rarely [118]. The goal of this project task was the computational inspection of the complexation abilities of borate and related ions at low concentration conditions in comparison to well characterized ligands. Besides the borate itself also borate esters have been considered as these products of the reaction of borate with carboxylic acids, which contribute to clay organic matter, may also be relevant and have been experimentally studied by the project partners Helmholtzzentrum Dresden-Rossendorf and TU Dresden [119].

Comparison of Ligands and Model Complexes

To support the interpretation of our results on borate and borate ester complexes we inspected pertinent properties of these ligands in comparison to perchlorate as a known non-complexing ligand and acetate as a commonly studied ligand of intermediate complexation strength. As mainly the ability to form coordination complexes as a donor ligand are of interest here, we also characterized the donor ability by model complexes with sodium, Na^+L^- , without including explicit aqua ligands of the cation.

The HOMO energy of borate and borate esters of -5.3 to -5.4 eV lies between the corresponding values for acetate of -4.6 eV and perchlorate of -6.4 eV (Table 12). Thus, it is to be expected that borates and their esters are weaker donor ligands than acetate, but considerably stronger than perchlorate. This trend is confirmed by the energy of the oxygen 1s levels, which serve as a local probe of the electrostatic potential. Accumulation of electronic charge on an atom will lead to a destabilization of the 1s core level. Borate and borate esters show values of the O 1s energies between acetate and perchlorate, for the free anion as well as in sodium complexes (Table 12). Mullikan charges, on the other hand, of coordinating oxygen atoms of borate of -0.57 *e* are even slightly higher than for acetate (-0.53 *e*), while borate esters yield a marginally lower values (-0.52 *e* for lactatoborate and -0.50 *e* for

Table 12: Comparison of the electronic structure of borate, lactatoborate (LacB), and salicylatoborate (SalB) anions with perchlorate and acetate ions as well as for the corresponding sodium complexes: HOMO energy, core level energies of O and Na 1s (in eV) and atomic charges (in e).

	ClO_4^-	BOH_4^-	LacB(OH)_2^-	SalB(OH)_2^-	CH_3COO^-
Ligand					
HOMO	-6.39	-5.27	-5.44	-5.34	-4.64
O 1s	-511.33	-509.32	-509.89	-510.01	-508.90
Charge O	-0.43	-0.57	-0.52	-0.50	-0.53
Complex					
O 1s	-512.23	-510.14	-510.56	-510.67	-509.88
Na 1s	-1035.07	-1034.03	-1034.86	-1034.31	-1034.15
Charge O	-0.43	-0.57	-0.52	-0.50	-0.53
Charge Na	+0.76	+0.72	+0.75	+0.76	+0.68

Table 13: ΔG (in kJ/mol) of complexation of boric acid with U(VI) and Am(III) with outer sphere (outer) and monodentate (mono) ligand coordination for coordination numbers (CN) of 5 for U(VI) and 8 and 9 for Am(III).

CN	$\Delta G(\text{U})$	$\Delta G(\text{Am})$	
	5	8	9
outer	+20	+20	+14
mono	+44	+31	+42

salicylatoborate). All these negative charges are higher than for perchlorate, which yields a value of $-0.43 e$. The same trends are confirmed by inspection of model complexes with sodium (Table 12). The Na 1s level is raised due to ligation more strongly for borate than for acetate, which borate esters yield values between acetate and perchlorate. Charges of coordinating O centers for borates resemble more the calculated value for acetate than for perchlorate. Also the charge of the sodium ion in the complex reflects some charge donation from borate, although lower than for acetate, while the charges calculated for perchlorate and borate esters are very similar (Table 12). These model results show that borate is a promising ligand for actinide complexation and that ester formation should reduce the complexation strength.

Borate Complexes

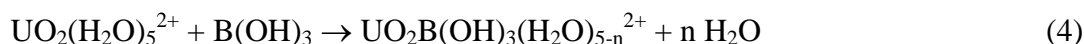
Boric acid B(OH)_3 in aqueous solutions is known to form a variety of borate multinuclear species with increasing pH provided the borate concentration exceeds 25 mM [118]. At lower concentration only the monoborate anion B(OH)_4^- is formed at a pH above 7. In this first computational study on actinide borate complexes in aqueous solution we concentrate on monoborate complexes of the form AnB(OH)_4^x which should be most relevant at low borate concentrations and medium pH. Although there are no direct hints in the literature, boric acid may form besides the Lewis anion B(OH)_4^- also a Brønstedt anion BO(OH)_2^- by release of a

Table 14: ΔG (in kJ/mol) of complexation of U(VI) and Am(III) with monoborate for complexes with outer sphere (outer) and inner sphere monodentate (mono), bidentate (bi), and tridentate (tri) ligand coordination with coordination numbers (CN) of 5 for U(VI) and 8 and 9 for Am(III).

CN	$\Delta G(\text{U})$	$\Delta G(\text{Am})$	
	5	8	9
outers	–	-78	-76
mono	-146	-112	-108
bi	-81	-105	-95
tri	-73	–	–

water molecule. Until now the Brønstedt anion has only been observed in the gas phase [120] and it is suggested as possible adsorbed species [121]. With increasing pH hydrolysis competes with actinide complexation. Thus, we also inspect the possible formation of ternary hydroxoborates for U(VI), as its hydrolysis starts already at $\text{pH} = 3$.

We started our investigation of actinide-borate complexes by inspection of a possible complexation of boric acid $\text{B}(\text{OH})_3$ with U(VI) or Am(III) aqua ions. This species dominates at acidic pH. Not unexpectedly, outer and monodentate inner sphere coordination of the neutral and unpolar boric acid ligand shows endothermic Gibbs free energies of complexation, calculated according to the reaction



for U(VI) and analogous for Am(III), with $n = 0$ for outer sphere and $n = 1$ for monodentate inner sphere boric acid coordination, are collected Table 13. These energies are more endothermic for inner sphere coordination, where boric acid replaces an aqua ligand, than for outer sphere coordination. Thus, boric acid binds weaker than an aqua ligand. These results show that complexation of actinides at lower pH by boric acid does not occur.

Uranyl(VI) borate complexes have been modeled with mono-, bi, and tridentate coordination of the borate ligand in the equatorial plane of uranyl (Fig. 4). For comparison also outer sphere coordination of borate was inspected, but no complex of this type could be stabilized. Instead, deprotonation of an aqua ligand of uranyl was observed and the proton coordinated to borate, yielding an outer sphere complex of uranyl monohydroxide with boric acid. This result does not come as a surprise as the deprotonation constant of the uranyl aqua complex (deprotonation constant -5.2 [122]) deprotonates at lower pH than the boric acid ($\text{pK}_a = 9.2$ [118]), thus favoring proton transfer from the uranyl aqua complex to borate instead of complexation of the borate ligand. Inner sphere uranyl(VI) borate complexes with mono- bi-, and tridentate coordination of the borate ligand show a decreasing Gibbs free energy of formation with increasing number of borate-uranyl bonds (Table 14). Thus, monodentate coordination of borate, replacing an aqua ligand, yields the most favorable complex. The

Table 15. Geometry parameters^a (in pm) and coordination number (CN) of uranyl(VI) monoborate complexes with mono-, bi-, and tridentate borate coordination:

Complex ^a	CN	U-O _t	U-O _B	U-B	U-O _w	U-O _{eq}
mono	5	180.2	233	365	247	244
bi	5	180.5	246	302	243	244
tri	6	180.9	256	283	244	250

^a Uranyl bond length U-O_t, U-O bond lengths to borate ligand U-O_B, distance to boron U-B averaged bond lengths to aqua ligands U-O_w, average over U-O bond to all ligands U-O_{eq}.

replacement of a second aqua ligand in the complex and the formation of a second coordinative bond of borate is unfavorable.

Geometry parameters of the uranyl monoborate complexes show a slightly increasing average uranyl bond U-O_t by less than 1 pm with increasing number of contacts to borate oxygens, reflecting a growing charge donation (Table 15). In line with the decreasing Gibbs free energy of complex formation, the bond lengths U-O_B between U and oxygens of borate increases from 233 pm for monodentate coordination to 256 pm for tridentate coordination (Table 15). These bond lengths are comparable to the ones to aqua ligands for the bidentate species and tend to be longer for the tridentate complex. In line with the increasing coordination number of the borate ligand to uranyl, the distances U-B decrease considerably, from 365 pm for the monodentate complex to 283 pm for the tridentate one. The average equatorial U-O bond lengths U-O_{eq} depends, as commonly observed (see above), essentially on the coordination number of the complex. It amounts to 244 pm for the five-coordinated mono- and bidentate species and increases to 250 pm for the six-coordinate tridentate species (Table 15). Thus, this quantity, which is commonly measured by EXAFS, is not helpful for identifying the structure of uranyl monoborate complexes. For this aim U-B as well as the relatively short U-O_B bond of the preferred monodentate complex are more suitable.

An(III) ions carry an effective charge comparable to actinyl(VI) species [90]. Thus we expect Am(III) monoborate complexes to exhibit a similar energy of complexation as for U(VI). In contrast to U(VI) we were able to optimize outer sphere complexes of Am(III) with the borate ion. This is explained by the lower first hydrolysis constant of Am(III) of -6.4 [80] of compared to -5.2 [122] for uranyl(VI), which corresponds to a pK_a still lower than for boric

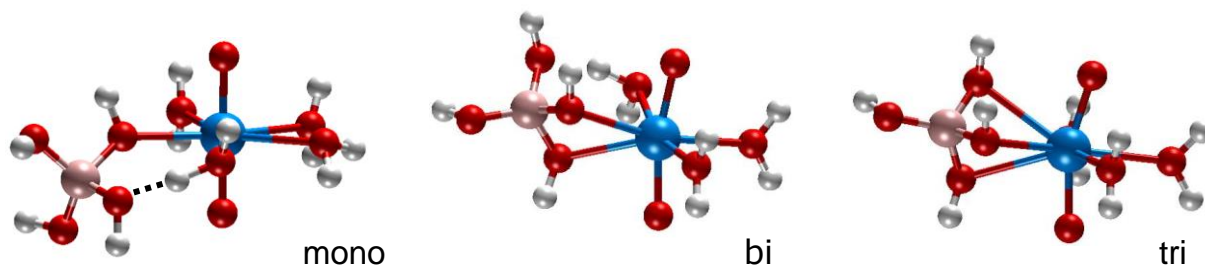


Figure 4: U(VI) monoborate complexes with monodentate, bidentate, and tridentate ligand coordination.

Table 16. Geometry parameters^a (in pm) of americium(III) monoborate complexes with outer sphere, inner sphere monodentate, and inner sphere bidentate borate coordination and coordination numbers 8 and 9.

Complex ^a	CN	Am-O _B	Am-B	Am-O _w	Am-O _{av}
outer	8		457	249	248
	9		469	251	251
inner mono	8	240	364	250	249
	9	244	368	254	253
inner bi	8	243	309	251	249
	9	246	311	253	252

^a Am-O bond lengths to borate ligand Am-O_B, distance Am to boron Am-B, averaged Am-O bond to aqua ligands Am-O_w, average over all Am-O bonds Am-O_{av}.

acid, but sufficiently close to allow an at least metastable minimum at the potential energy surface. In our model calculations, the outer sphere Am(III) borate species are by about 77 kJ/mol more stable than the well separated ions (Table 14) due to electrostatic attraction. Inner sphere borate complexes yield as expected higher complexation energies of -95 to -112 kJ/mol and thus are calculated to be less stable than the most stable U(VI) monoborate isomer (-146 kJ/mol). As for U(VI), monodentate borate coordination is preferred (Table 14), although bidentate isomers are energetically close. Also the energy differences between eight- and nine-coordinated species are small, 4 and 10 kJ/mol for the mono- and the bidentate isomer, respectively, with a slight preference for CN = 8 (Table 14). Thus, our model calculations suggest the existence of Am(III) monoborate complexes in solution with a preferred CN of 8 and most probably the existence of isomers and species with neighboring coordination numbers.

Geometry parameters of Am(III) borate complexes are collected in Table 16. Am-O bond lengths to borate, Am-O_B increase slightly with increasing coordination of the borate ligand as well as with the overall CN of Am(III). The shortest of these bonds of 240 pm is calculated for the most stable monodentate structures. For all complexes Am-O_B is at most by 10 pm shorter than bonds to aqua ligands, Am-O_w. Averaged Am-O bonds averaged over all ligands, Am-O_{av}, depend essentially on the CN and are even similar for outer and inner sphere borate coordination. They are by about 3 pm shorter for CN = 8 than for CN = 9 (Table 16). Similar as for other complexes discussed so far, only the Am-B distance discriminates the coordination modes of borate. It amounts to about 310 pm for bidentate coordination and increases to about 365 pm for monodentate coordination (Table 16).

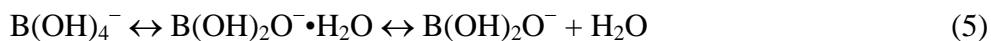
As accurate absolute energies of complexation are hard to calculate, we compared our energies for Am(III) monoborate complexes to those of monoacetate and monoperochlorate complexes (Table 20). This allows to confirm the thermodynamic stability of borate complexes by relating the energies of complexation to those of well known species. The complexation energy of Am(III) borate in monodentate coordination of -112 kJ/mol slightly

Table 17. Comparison of the geometry parameters (see Table 15, in pm) and complexation energies (in kJ/mol) of uranyl(VI) monoborate complexes with monodentate ligand coordination of the Lewis anion B(OH)_4^- and the Brønsted anion $\text{B(OH)}_2\text{O}^-$ in equatorial (eq) and axial (ax) orientation.

Complex ^a	CN	U-O _t	U-O _B	U-B	U-O _w	U-O _{eq}	ΔG
B(OH)_4^-	5	180.2	233	365	247	244	-146
$\text{B(OH)}_2\text{O}^-$ eq	5	181.2	219	341	250	244	-149
$\text{B(OH)}_2\text{O}^-$ ax	5	181.9	217	331	251	244	-146

exceeds the one for the most stable bidentate coordinated acetate species of -105 kJ/mol. For monoperochlorate we obtain vanishing or slightly positive Gibbs free energies of complexation. This result qualitatively confirms the expectation that perchlorate does not complexate and supports the qualitative reliability of our approach. Thus, monoborate complexes of U(VI) and Am(III) are thermodynamically stable and their complexation energy should be a little larger than for acetate.

We also considered the possible existence of the Brønsted anion $\text{B(OH)}_2\text{O}^-$ of the boric acid in solution. This species has until now only been found in the gas phase [120] and but not in solution. We inspected the energies of the model equilibrium reaction



of water dissociation from the Lewis anion to form the Brønsted anion via an intermediate explicit aqua complex in solution. Interestingly, this simple model yields the aqua complex of the Brønsted anion as the most stable species. In contrast to a mass spectrometry experiment in the gas phase [120], the Lewis anion is calculated to be about 50 kJ/mol more stable than the Brønsted anion. This difference decreases to about 10 kJ/mol in solution, showing that the Brønsted anion might be thermodynamically accessible in complexes.

As the unprotonated oxygen of the Brønsted anion represents a favorable coordination center, we compared U(VI) complexes with monodentate $\text{B(OH)}_2\text{O}^-$ to the most favorable monodentate one for B(OH)_4^- (Table 17). Independent of equatorial or axial orientation of the ligand plane, uranyl complexes with Lewis and Brønsted anions are of very similar stability. The exchange of a water ligand of the solvated uranyl(VI) ion with an borate anion is exothermic by nearly 150 kJ/mol. The comparison of the geometries of these complexes reflects the better donor capability of $\text{B(OH)}_2\text{O}^-$, leading to slightly elongated uranyl bond lengths U-O_t by 1-2 pm compared to the complex with the Lewis borate. Also the coordinating bonds of borate oxygens to U are different. Their lengths amount to nearly 220 pm for $\text{B(OH)}_2\text{O}^-$ compared to 233 pm for B(OH)_4^- (Table 17). As the coordination number of all complexes is 5, U-O_{eq} is the same for all complexes and calculated to 244 pm. Thus, a distinction of Lewis and Brønsted monoborate uranyl complexes by EXAFS should be

Table 18. Comparison of geometry parameters^a (in pm) and complexation energies (in kJ/mol) of uranyl(VI) monohydroxide monoborate complexes with the Lewis anion B(OH)₄⁻ (outer sphere, mono- and bidentate ligand coordination) and the monodentate coordinated Brønsted anion B(OH)₂O⁻ in equatorial (eq) and axial (ax) orientation.

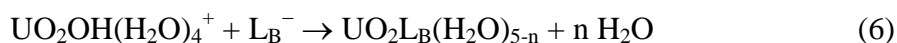
Complex ^a		CN	U-O _t	U-O _H	U-O _B	U-B	U-O _w	U-O _{eq}	ΔG
B(OH) ₄ ⁻	outer	5	182.7	217		511	250	243	-22
	mono	5	182.5	218	244	370	252	244	-38
	bi	5	182.5	217	247	313	252	243	-58
B(OH) ₂ O ⁻	eq	5	183.4	222	224	346	257	243	-96
	ax	5	184.2	221	222	332	257	242	-91

^a Bond lengths of hydroxide ligand to uranium U-O_H, for other parameters see Table 15.

difficult, but might be possible by means of the U-B distances, which amount to 365 pm for B(OH)₄⁻ and to about 330-340 pm for B(OH)₂O⁻.

Hydroxoborate Complexes

As uranyl(VI) hydrolysis starts already at the low pH of about 3, complexation by borate anions competes with hydrolysis. Thus, besides uranyl borate complexes, we also inspected possible complexes of uranyl monohydroxide with borate anions. For the ligand arrangement in the complexes we choose trans configurations, as it is expected that cis configurations are less stable due to repulsion of the anionic ligands. Complexation energies, calculated as the exchange of an aqua ligand of uranyl monohydroxide by borate for inner sphere complexes,



With n being the number of aqua ligands replaced by borate, are considerably lower than for uranyl borate complexes (Tables 14 and 19). For monodentate complexation of B(OH)₄⁻ the complexation energy decreases from -146 to -38 kJ/mol due to hydroxide coordination. This decrease is weaker for bidentate coordination, where the complexation energy drops from -81 kJ/mol to -58 kJ/mol, resulting in bidentate coordination to be more favorable for the ternary complex in contrast to monoborate. For B(OH)₄⁻, inner sphere complexes are somewhat more stable than the outer sphere one, by 16 kJ/mol for monodentate and 36 kJ/mol for bidentate coordination, respectively (Table 18). Complexes of uranyl monohydroxide with the Brønsted anion B(OH)₂O⁻ show a complexation energy of slightly more than 90 kJ/mol and thus are calculated to be more favorable than complexes with the Lewis anion.

The increased stability of the B(OH)₂O⁻ complexes compared to B(OH)₄⁻ complexes is reflected also in their geometry. The bond U-O_H of uranium to the hydroxide ligand is by 3-5 pm longer for the Brønsted anion complexes than for the Lewis anion complexes due to weaker bond competition of the latter ligand. In line with this trend, also the bond to aqua ligands, U-O_w, are by 5 pm longer for the Brønsted anion complexes (Table 18). As in the monoborate complexes, the U-O_B bonds between uranium and the borate ligands are longer

Table 19. Geometry parameters (see Table 16, in pm) and complexation energy ΔG (in kJ/mol) of americium(III) lactatoborate (LacB) and salicilatoborate (SalB) complexes with CN = 8 with monodentate and bidentate ligand coordination compared to monoborate complexes.

Complex ^a		Am-O _B	Am-B	Am-O _w	Am-O _{av}	ΔG
B(OH) ₄ ⁻	mono	240	364	250	249	-112
	bi	246	311	253	252	-105
LacB	mono	242	367	252	251	-60
	bi	247	309	250	249	-46
SalB	mono	245	363	250	249	-88
	bi	249	312	248	248	-36

for B(OH)₄⁻ (Table 18). Their increase due to the presence of the hydroxide ligand amounts to 11 pm for the monodentate B(OH)₄⁻ complex, to 1 pm for the bidentate one and to 5 and 1 pm for the two Lewis anion complexes. U-O_{eq}, calculated as 242-244 pm for the ternary complexes, is essentially unaffected by hydrolysis or the type of the borate anion. This is another interesting example showing that U-O_{eq} reflects the coordination number of the complex and is not sensitive to other changes (see above). The distance U-B, which might be helpful for an experimental discrimination of various uranyl monoborate species, increases only slightly, by 1-11 pm, due to the presence of hydroxide in the ternary complexes. The differences of this parameter between the two borate ligands and their coordination modes stay unaffected (compare Tables 15, 17, and 18).

Borate Ester Complexes

Boric acid is known to react with carboxylic acids to form borate esters [123]. Thus borate esters are of some interest as possible ligands for actinide complexation under conditions of final repositories when natural organic matter is present together with boric acid or borate. Difficulties to characterize Eu borate complexes at lower borate concentration and precipitation at higher concentrations [124] motivated to suggest borate esters also as model compounds for other borate complexes [119]. This approach has been used by the project partners TU Dresden and Helmholtz-Zentrum Dresden-Rossendorf to estimate the complexation strength of borate ligands [119].

We studied the complexation of lactatoborate and salicilatoborate with Am(III) as an exemplary case to complement the experimental and computational studies of the project partners on Eu(III) organoborates [119]. Mono- and bidentate ligand coordination to Am(III) have been modelled for the probable coordination number of 8 (Table 19). Ligand substitution Gibbs free energies for lactato- and salicilatoborate yield a preference for monodentate coordination, which is stronger than for monoborate. Compared to monoborate, complexation energy is weaker for the organoborates (Table 19). This trend is reflected also by the Am-O_B bonds to the borate ligand. These bonds are longer for the organoborates by up to 5 pm compared to the monoborate ligand (Table 19). The absolute values of Am-O_B for bidentate complexes of 246-249 pm are similar to calculated results for Eu(III) monoborate and

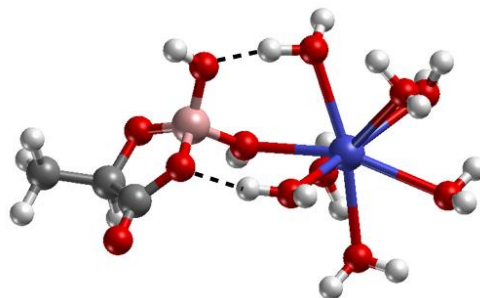


Figure 5: Am(III) lactatoborate with monodentate ligand coordination.

Table 20: Comparison of Am(III) complexation energies (in kJ/mol) of borate, organoborates, acetate, and perchlorate for mono- and bidentate ligand coordination for CN = 8.

	mono	bi
acetate	-90	-105
borate	-112	-105
lactatoborate	-60	-46
salicylatoborate	-88	-36
perchlorate	0	+20

organoborates of 243-256 pm [119]. The corresponding Am-B distances vary only slightly (Table 19). As for borate, they are longer, about 365 pm, for monodentate ligand coordination, and shorter, about 310 pm, for bidentate ligand coordination. The average Am-O_w bonds to aqua ligands as well as the average bond lengths to all oxygen centers of the first coordination sphere, Am-O_{av}, are very similar for borate and organoborates. Thus, these structural parameters accessible to EXAFS seem to be too similar to distinguish monoborate and organoborate complexes, although the complexation energies vary notable (Table 19). As absolute complexation energies are difficult to calculate, we compare in Table 20 calculated ligand substitution energies with corresponding energies of the well known ligands perchlorate and acetate. This comparison suggests that monoborate complexation is of comparable strength as acetate, while organoborates yield lower complexation energies. As their substitution energies are well below the values obtained for perchlorate, they should form complexes, in agreement with the work of our project partners [119], but weaker ones than acetate and borate. Comparison of our results to corresponding calculations for Eu(III) complexation [119], applying large core pseudopotentials to account for relativistic effects, shows some differences. For Eu(III) energy differences between various coordination modes of the ligands are claimed to be much smaller [119] than for Am(III) (Table 19). In addition, from Eu-O_B bond lengths variations of up to 10 pm it is concluded that monoborate, polyborate, and organoborates should complexate with essentially the same strength. On the other hand, our results show that smaller variations of bond lengths of up to 5 pm can go along with appreciable energy changes (Table 19). Thus, with respect to geometry aspects, organoborate complexes may well serve as models for monoborate complexes, but a weaker metal-ligand interaction has to be taken into account, especially when complexation constants of related species are inferred.

4.2 Adsorption of actinides on clay minerals

Our computational investigation of actinide adsorption on clay minerals concentrated on the adsorption on edge surfaces of the common class of dioctahedral 2:1 smectite clay minerals like montmorillonite, the main mineral component of bentonite. This type of minerals also forms a considerable fraction of the mineral content of clay formations, which are considered as possible host formations for final repositories for highly radioactive waste [125]. Furthermore, it has been shown that clay minerals are essentially responsible for the adsorption capability of clays with respect to actinides [7,126].

2:1 clay minerals like smectites consist of a sheet of alumina octahedra sandwiched between two sheets of silica tetrahedral [127,128]. The inert silica sheets form the basal (001) surfaces of clay mineral layers, while the more reactive edge surfaces, featuring a pH dependent variable charge, are essentially perpendicular to these surfaces. Depending on the permanent charge of the layers, charge balancing counter ions and a variable amount of water is intercalated between the layers. Actinide adsorption on clay minerals is considered to proceed via two mechanisms, depending on pH conditions [7]. At low pH actinide ions are adsorbed as outer sphere species between the layers, replacing counter ions. With increasing pH, edge surfaces are get negatively charged due to increasing deprotonation of aluminol and silanol groups. This allows inner sphere adsorption of actinide ions at increased pH. Our study of actinide adsorption on clay mineral surfaces concentrated on inner sphere adsorption at edge surfaces, corresponding to the main process at moderately acidic to basic pH conditions [7], which are relevant for a final repository in clay formations.

As structure and properties of clay mineral surfaces at the atomic scale are so far not well understood, we started our studies by characterization of the edge surfaces of model minerals and then proceeded to the modeling of adsorbed actinide ions in order to determine preferred sites and structures of adsorption complexes. With these calculations we aimed at a contribution to the speciation and thermodynamics of actinide ions at clay mineral surfaces. The detailed information obtained is very useful to improve and extend current thermodynamic models [8-10], which have been constructed essentially empirically. Pertinent questions to be approached are the number, type and properties of favorable adsorption sites, the speciation and properties of adsorbed actinide ions and their dependence on the type clay mineral, the surface orientation, structure and charge.

4.2.1 Edge surfaces of charged clay minerals

Mineral models

In the present project we concentrated on dioctahedral 2:1 type phyllosilicates [129]. For smectites to be modelled the mineral layers contain charged substitutions (typically Si^{4+} substituted by Al^{3+} or Al^{3+} substituted by Mg^{2+} , Fe^{2+}), generating the permanent layer charge, and solvated counter ions, e.g. Na^+ , K^+ , Ca^{2+} , between the layers, respectively [127,128]. We constructed model clay minerals with the stoichiometric formula $\text{Na}_l(\text{Si}_{4-n}\text{Al}_n)$

Table 21. Lattice parameters of monoclinic 2:1 smectite model minerals $\text{Na}_l(\text{Si}_{8-n}\text{Al}_n)(\text{Al}_{4-m}\text{Mg}_m)\text{O}_{20}(\text{OH})_4$: pyrophyllitic model (Pyro, $l, n, m = 0, ,$), beidellitic model (Beid, $l, n = 0.25, m = 0$), montmorillonitic model (Mont, $l, m = 0.25, n = 0$) one. Lattice vectors in pm, angles in degrees.

Mineral	a	B	c	β
Pyro	1047.7	903.0	1309.2	99.2
Beid	1047.6	903.7	1323.4	99.1
Mont	1050.8	905.2	1330.6	97.2

$(\text{Al}_{2-m}\text{Mg}_m)\text{O}_{10}(\text{OH})_2$, where l corresponds to the permanent layer charge per formula unit (f.u. = half unit cell), and n and m are the number of substitutions in tetrahedral and octahedral sheets per f.u., respectively. The two types of charged substitutions studied are the tetrahedral substitution of Si^{4+} by Al^{3+} , corresponding to $l = 0.25, n = 0.25, m = 0$, called further on beidellitic model, and the exchange of octahedral Al^{3+} by Mg^{2+} ($l = 0.25, n = 0, m = 0.25$), which we refer to as montmorillonitic model. These two mineral models correspond to ideal beidellite, which is the end-member of the smectites with only tetrahedral charge, and to ideal montmorillonite, which is the end member with only octahedral charge. As we chose a single substitution per $2 \times 1 \times 1$ unit cell, our models correspond to a layer charge q of -0.25 . As an uncharged reference we use the neutral mineral pyrophyllite, $l, m, n = 0$, with a water monolayer between the layers. These three mineral models of ideal pyrophyllite with an artificial water interlayer, of beidellite, and montmorillonite, can also be considered as local

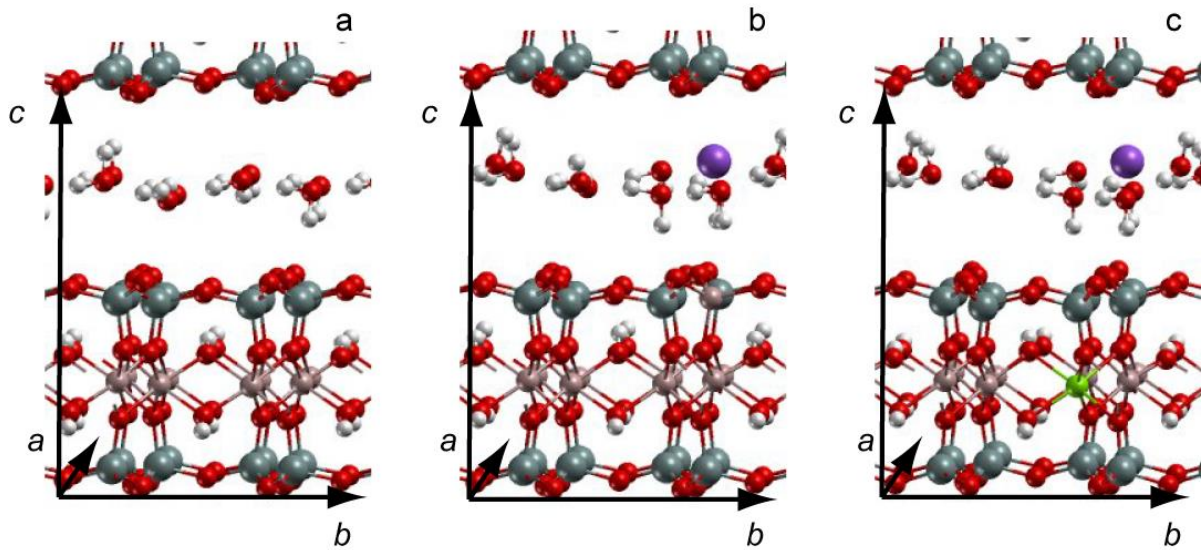


Figure 6. Optimized bulk structures of monoclinic 2:1 smectite model minerals: (a) neutral pyrophyllitic model with water interlayer, (b) beidellytic model with substitution in the tetrahedral layer, Na^+ counterion and interlayer water, (c) montmorillonitic model with substitution in the octahedral layer, Na^+ counterion and interlayer water. Color coding: red – O, grey – Si, brown – Al, green – Mg, violet – Na, white – H.

models of a generic smectite, representing regions without substitutions or the environment of a tetrahedral or octahedral substitution, respectively. For all the model clay minerals a monoclinic lattice was chosen, as it is the most common one.

The optimized bulk structures of all three mineral models are shown in Fig. 1 and the optimized lattice parameters are collected in Table 21. The lattice parameters of all three models are very similar, except for the c vector defining the distance between the mineral layers. The neutral pyrophyllitic model exhibits the shortest c vector of 1309 pm, as it accommodates only water between the layers. Beidellitic and montmorillonitic models exhibit by about 20 pm longer c vectors of 1323 and 1330 pm, respectively, due to presence of Na^+ counterions in the interlayer. These bulk models were used to create the edge surface models.

Edge surfaces

Crystal growth theory predicts (100), (010), (± 110), and (± 130) edge surfaces for 2:1 clay minerals [130-132]. White and Zelazny determined (110) and (010) edge surfaces to be favorable using periodic bond chain (PBC) theory [133]. Kuwahara studied dissolution of smectites by means of in-situ AFM and detected dissolution on (010) and (110) surfaces [134]. Thus, mainly (010) and (110) surfaces are to be expected for smectites. In addition, (100) and (130) might exist. Ideal structures of all four low index edge surface orientations have been studied computationally for pyrophyllite [33]. Each edge surface orientation of pyrophyllite exhibits a single preferred termination [33]. We assume that the charged dioctahedral 2:1 clay minerals exhibit edge surfaces with the same structure as determined for pyrophyllite, even when substitutions and interlayer counter ions are present close to the surface.

In this project we studied the three edge surfaces (010), (110), and (100). Their structures are shown in Fig. 7. We cut the bulk beidellitic and montmorillonitic crystal models parallel to these surfaces in such a way, that the substitution is always in the second outermost cation position from the surface. This position of the defect we define as “inner”. The models of edge surfaces with charged substitutions directly on the surface are created from the models with inner substitution by moving the substitution to the surface while keeping the position of the counter ion Na^+ . This position of the substitution we refer to as a surface substitution.

For these models of edge surfaces surface energies in the gas phase were estimated according to

$$E = (E_{\text{surf}} - E_{\text{bulk}} - 10 E_{\text{H}_2\text{O}})/2A, \quad (7)$$

where E_{surf} is the total energy of the surface, E_{bulk} the total energy of the bulk structure, $E_{\text{H}_2\text{O}}$ the total energy of a water molecule, and A is the surface area in \AA^2 . We needed 8 water molecules to saturate dangling bonds at the surfaces to achieve a proper hydroxylation of the surfaces. In addition two water molecules were added to the interlayer, preserving the hydration of the Na^+ counter ion. Table 22 shows the surface energies corrected in addition by

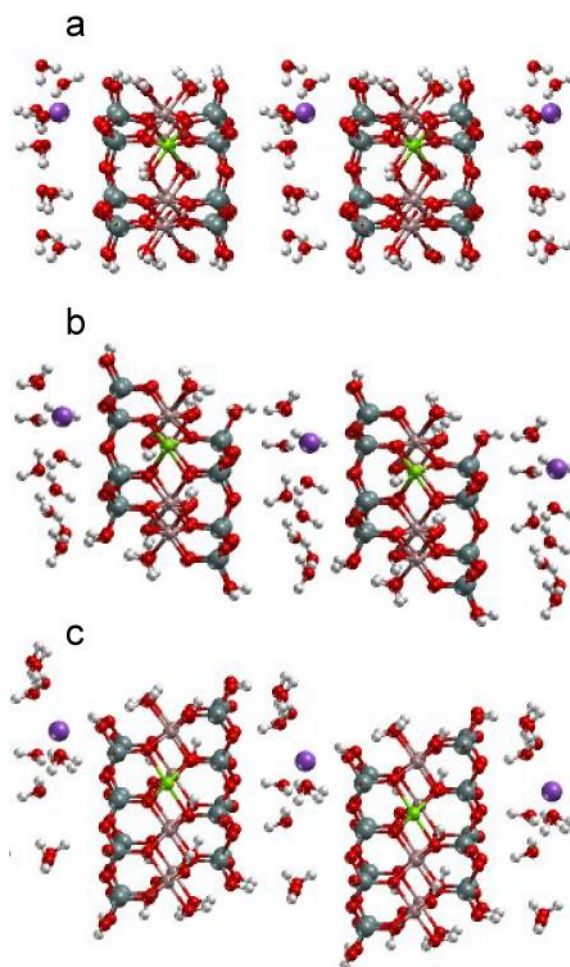


Figure 7. Structures of three orientations of edge surfaces of model smectites for the example of the montmorillonite model with inner substitution: (a) (010), (b) (110), (c) (100). The unit cell contains a single mineral layer together with a layer of interlayer water. The figure shows at least two unit cells in c direction to visualize the layers stacking. For color coding see Fig. 6.

a solvation correction for the 10 saturating water molecules, estimated at 29 kJ/mol for each [135]. (110) is the most stable edge surface orientation for pyrophyllite and montmorillonite. The beidellitic mineral model exhibits (110) and (100) surfaces of similar stability, except for one of the two possible surface substitutions (Table 22), where (100) is preferred. For montmorillonite, surface or inner position of the substitution does not affect the relative stability of the various edge surface orientations. Our results for pyrophyllite are in qualitative agreement with earlier results [33], even though our model contains interlayer water. This finding supports the transferability of the relative surface stability to other mineral models. For the (130) surface of pyrophyllite a surface energy of 5.7 meV/\AA^2 has been calculated [33], which shows that this edge surface orientation is less stable than the ones chosen here.

Edge surfaces exhibit various surface groups (Figure 7), as listed in Table 23: SiOH , $\text{AlOH}_2^{+1/2}$, $\text{AlOH}^{-1/2}$, $\text{AlSiO}^{-1/2}$, and Al_2OH . $\text{AlOH}_2^{+1/2}$ is present on all surfaces. $\text{AlOH}^{-1/2}$ exists only on the (010) surface (Figure 7), while the other two surfaces, (110) and (100), exhibit a so-called mixed oxygen center O_m , coordinating to an Al and a Si atom and leading to the surface group $\text{AlSiO}_m^{-1/2}$. Al_2OH groups are usually situated rather deep below the

Table 22. Surface energies (in $\text{meV}/\text{\AA}^2$) of bare edge surfaces of smectite model minerals pyrophyllite (Pyro), beidellite (Beid), and Montmorillonite (Mont) for inner (not labeled) (see Fig. 7) and surface (s) positions of the substitutions in the permanently charged minerals.

Mineral	(010)	(100)	(110)
Pyro	7.49	1.57	0.36
Pyro ^a	5.4	1.9	1.6
Beid	10.85	8.66	8.94
Beid-s1 ^b	10.10	7.21	11.68
Beid-s2 ^c	12.02	9.43	8.30
Mont	8.80	6.91	3.33
Mont-s	9.69	8.94	4.08

^a Ref. 33; ^b upper Si is substituted; ^c lower Si is substituted.

surface, so we do not consider these groups as relevant for adsorption, and do not discuss them further. Partial charges of oxygens of all possible surface groups of the protonated as well as partially deprotonated surfaces, as derived from Pauling's bond valence theory [136], are in collected Table 23.

Considering metal ion adsorption, surface solvation must be taken into account, as it was proven to play a crucial role for the edge surface of kaolinite [137]. Therefore, all calculations were carried out with 1-2 water layers consisting of 16 water molecules per unit cell, to solvate the edge surfaces. In most cases surface solvation does not affect the surface groups, but there are few exceptions. In case of beidellite with surface substitution of the upper Si (s1) (Fig. 7) by Al on the (110) surface, a proton from the neighboring AlOH_2 surface group moves to the AlOAl group created due to substitution, leading to an AlOHAl group. In case of the (010) surface due to solvation a proton of an AlOH_2 surface group may

Table 23. Surface groups and corresponding formal charges (e) of oxygen centers of edge surfaces of 2:1 smectite models for neutral as well as partially deprotonated surfaces. For montmorillonite (Mont) and beidellite (Beid) only the additional groups appearing due to surface substitution are listed.

Surface	Mineral	Groups	Charge
(010), (110), (100)	all	$\text{SiOH}; \text{SiO}$	0; -1
		$\text{AlOH}_2; \text{AlOH}; \text{AlO}$	1/2; -1/2; -3/2
	Mont	$\text{MgOH}_2; \text{MgOH}; \text{MgO}$	1/3; -2/3; -5/3
	Beid	$\text{AlOH}; \text{AlO}$	-1/4; -5/4
(110), (100)	all	AlSiO_m	-1/2
	Mont	MgSiO_m	-2/3
	Beid	$\text{AlOHAl}; \text{AlOAl}$	+1/4; -3/4

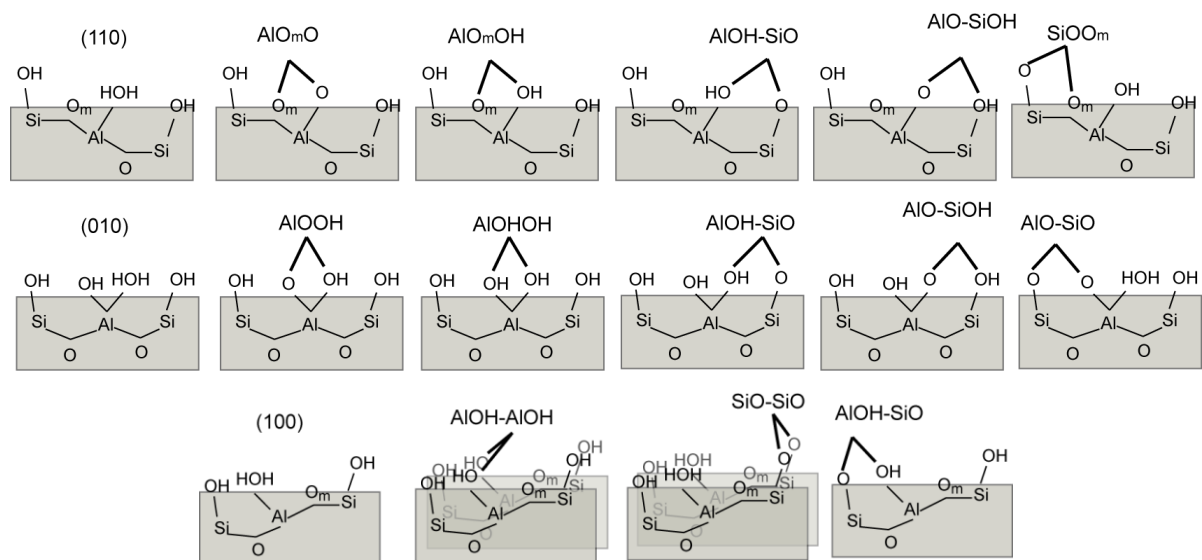


Figure 8. Unsubstituted adsorption sites on (110), (010), and (100) edge surfaces of model smectites.

protonate a neighboring AlOH group. Thus, the solvated surface does not exhibit an ordered arrangement of AlOH and AlOH₂ groups.

4.2.2 U(VI) adsorption

Adsorption sites

We studied bidentate inner-sphere adsorption of uranyl [129] as in experiments this type of adsorption was postulated [138,139]. The possibility of monodentate adsorption complexes we inspected exemplary when comparing U(VI) and Np(V) adsorption (Section 4.2.3). To avoid a charged unit cell, the surface is always doubly deprotonated. Two oxygen centers of the surface were chosen as adsorption site if they are closer than 340 pm. For larger distances between oxygens we did not obtain bidentately coordinated adsorbed species. We studied three types of adsorption sites: aluminol sites, mixed sites, and silanol sites. Aluminol (silanol) sites are those that include only aluminol (silanol) groups. The mixed sites comprise an aluminol group and a neighboring silanol group, AlO(H)-SiO(H). If the substitution is not on the surface (inner variant) then the available adsorption sites are the same for pyrophyllite and permanently charged mineral models. The adsorption site is regarded as different when surface substitutions are involved in the site, because they lead to more negative charges of neighboring surface oxygens.

Adsorption on (010) and (110) edge surfaces was studied in detail for various adsorption sites, as shown in Fig. 8. The (100) surface, considered as less probable, exhibits sites similar to the ones at the (110) surface and in addition long-bridge sites, which are not available on (010) and (110) edge surfaces. Therefore we inspected three sites on the (100) surface, two characteristic only for this surface, AlOH-AlOH and SiO-SiO, and AlOH-SiO, which is also present on the other edge surfaces (Fig. 8).

Table 24. Adsorbed species and their coordination numbers for various unsubstituted sites for bidentate uranyl adsorption on edge surfaces of dioctahedral 2:1 clay mineral edge surfaces.

(010)			(110)			(100)		
Site	Adsorbate	CN	Site	Adsorbate	CN	Site	Adsorbate	CN
Aluminol								
AlOOH	UO ₂ ²⁺	5	AlO _m O	UO ₂ ²⁺	5	AlOH-AlOH	UO ₂ ²⁺	4
AlOHOH	UO ₂ ²⁺	5	AlO _m OH	UO ₂ OH ⁺	5			
	UO ₂ OH ⁺	5						
Mixed								
AlOH-SiO	UO ₂ OH ⁺	5, 4	AlOH-SiO	UO ₂ ²⁺	5, 4	AlOH-SiO	UO ₂ ²⁺	5
AlO-SiOH	UO ₂ ²⁺	4	AlO-SiOH	UO ₂ ²⁺	5, 4			
SiO-AlO	UO ₂ ²⁺	4						
Silanol								
			SiOO _m	UO ₂ OH ⁺	5	SiO-SiO	UO ₂ ²⁺	4

Adsorbed species

The initial structures of adsorption complexes of UO₂²⁺ were constructed in such a way that the uranyl moiety exhibits two contacts to the surface and coordinates three aqua ligands in the first solvation shell, thus exhibiting the most common uranyl coordination number of 5. In many cases this arrangement was preserved during structure optimization and the surface complexes converged to five-fold coordinated uranyl adsorbed in bidentate fashion (Table 24). Besides we observed changes of the coordination number from 5 to 4 or deprotonation of an aqua ligand of uranyl and coordination of that proton to a neighboring surface AlOH^{-1/2} group to form AlOH₂^{+1/2} [129]. As a result, uranyl monohydroxide is obtained as adsorbate. It was shown computationally that the AlOH^{-1/2} group is a good proton acceptor [140-142]. The pK_a value of the uranyl(VI) aqua complex in solution is about 5.2 [122,143], while the intrinsic pK_a of the AlOH₂^{+1/2} surface group was estimated at 5.5 and higher, depending on the edge surface orientation [144]. Thus, the uranyl ion is inclined to deprotonate if there is an AlOH^{-1/2} surface group nearby. The observed lowering of the CN occurs due to the release of an aqua ligand of the first coordination shell of uranyl to the “solution” during structure optimization. This is commonly observed for sites where the two surface O_s centers coordinating to uranyl are more than 300 pm apart. This long O_s-O_s distance leads to an increase O_s-U-O_s angle, which decreases the space available for coordination of aqua ligands. Adsorption sites with a rather long O_s-O_s distance are mixed AlO(H)-SiO(H) sites and long bridge sites on (100) surfaces, SiO-SiO and AlOH-AlOH. For some sites we were able to model both coordination numbers 4 and 5 or hydrolyzed as well as non-hydrolyzed adsorbed uranyl (Table 24). Note that the coordination number may change for uranyl as well as for uranyl monohydroxide adsorbates.

Detailed comparison of exemplary complexes on various mineral models

In almost all cases the optimized adsorbed species are the same for the same type of site on an edge surface for various model minerals. Also the characteristic structural parameters of complexes adsorbed on a specific site vary only slightly between the various mineral models [129]. An exemplary comparison is given in Table 25 for the AlOOH site at the (010) surface and the AlO_mOH site at the (110) surface, together with their cation substituted variants, MgOOH and MgO_mOH on surface substituted montmorillonite, and for the AlOAlOH site on surface substituted beidellite.. For the AlOOH site on the (010) surface, the uranyl bond U-O_t varies between 185 and 188 pm for all five mineral models without substitution of the Al site cation, leading to an average of 186 pm and a mean absolute deviation of about 1 pm. Similar small variations are calculated for the two bonds of U to the surface, U-O_s , of 203 and 241 pm on average. Here the longer and thus weaker bond shows slightly stronger variations than the short one (Table 25). Also the average equatorial U-O bond U-O_{eq} and the U-Al distance differ only marginally for the various mineral models. While substitutions distant from the adsorption site have only a small effect on geometric parameters of the adsorption complex, substitution of the site cation yields stronger changes. Surface substitution of montmorillonite changes the AlOOH site to MgOOH . As an effect of this site cation substitution the uranyl bond of 190 pm is longer than for other mineral models because the site oxygens are more negative (Table 23), leading to a stronger interaction with uranyl. This bond strengthening is also reflected in the short and long U-O_s bonds to the surface, which shorten by 5 and 9 pm, respectively, compared to the average for unsubstituted sites for the U-O bonds to the surface. All other geometry parameters listed in Table 25 still are close to the values for the AlOOH site. The second example, the AlO_mOH site on the (110) surface, where uranyl monohydroxide is calculated as adsorbate (Table 24), yields similar trends. The mean absolute deviations (MAD) from the average of U-O_t , the shorter of the U-O_s bonds (233 pm on average), the U-O_H bond, U-O_{eq} , and U-Al are at most 2 pm. Larger MADs are observed for weak bonds, like the longer of the U-O_s bonds (259 pm on average) with an MAD of 6 pm and the bond lengths to aqua ligands with $\text{MAD} = 9$ pm. Site cation substitution again leads to noticeable changes of the adsorption complex. For the AlOAlOH site on surface substituted beidellite, the two bonds U-O_s to the surface are rather similar, 237 and 239 pm, while they differ for unsubstituted sites by 26 pm on average (Table 25). This rather symmetric bidentate uranyl monohydroxide surface complex also shows a relatively long uranyl bond of 184 pm and a rather short U-Al distance of 336 pm. Similar changes of geometry are obtained for the MgO_mOH site, although with a stronger uranyl binding with $\text{U-O}_t = 181$ pm, being slightly below average. This short uranyl bond can essentially be traced back to a weaker binding of the hydroxo ligand, which features a U-O_H bond length of 230 pm, 4 pm longer than the average for unsubstituted sites (Table 25). For all other sites inspected, similar results have been obtained when comparing adsorption complexes for a specific site for various mineral models [129]. Also comparison of experimentally determined geometry parameters of

Table 25. Structural parameters (in pm)^a of uranyl adsorption complexes of exemplary sites on (010) and (110) edge surfaces of 2:1 clay mineral models. In addition averaged parameters for all surfaces without substitution as well as the corresponding mean absolute deviations are given.

Site	Surf. ^b	Mineral	U-O _t	U-O _s ^c	U-O _H	U-O _w	U-O _{eq}	U-Al/Mg	
AlOOH	(010)	Pyro	185	204	239	260–270	247	325	
		Beid	186	203	243	252–269	245	323	
		Beid s1	186	203	243	255–267	246	322	
		Beid s2	186	203	240	252–272	245	322	
		Mont	188	202	238	246–261	241	325	
Aver. (MAD)			186(1)	203(0)	241(2)	260(5)	245(1)	323(1)	
MgOOH		Mont s	190	198	232	249–267	241	326	
AlO _m OH	(110)	Pyro	182	237	268	224	240–248	243	353
		Beid	183	233	259	226	238–253	242	349
		Beid s1	183	230	262	226	239–256	243	351
		Mont	181	232	247	225	263–265	246	352
Aver. (MAD)			182(1)	233(2)	259(6)	226(1)	251(9)	244(1)	351(1)
AlOAlOH		Beid s2	184	239	237	229	242–253	240	336
MgO _m OH		Mont s	181	229	238	230	266–270	247	348

^a Average terminal uranyl bond length U-O_t, bond lengths U-O_s to surface oxygen centers, U-O_H bond length to OH ligands, bond lengths U-O_w to aqua ligands, average equatorial U-O bond length U-O_{eq}, U-Al and U-Mg distances to the nearest surface Al and Mg centers.

^b Surface models, Pyro – pyrophyllitic, Beid – beidellitic, Mont – montmorillonitic, s = surface substitution, s1 and s2 on the beidellite (110) surface label substitution of the upper and lower Si, and on the (010) surface left and right Si, respectively, see Fig. 8.

^c The order of U-O_s bonds follows the site designation.

uranyl(VI) adsorbed on clay and related minerals, as measured by EXAFS, are similar and not characteristic for the various clay and related minerals [145].

Thus, the structures of uranyl adsorption complexes on edge surfaces of smectite model minerals seem to be essentially determined by the type of the adsorption site and independent of the type of mineral. This similarity holds also for different edge surface orientations, as exemplified by the few cases of sites which are present on different surface orientations, e.g. the site AlO-SiOH on (010) and (110) edge surfaces [129]. These preliminary observations show that we reasonably can discuss in the following structures averaged over minerals instead of individual complexes. Surface cation substitution at an adsorption site affects adsorption complexes stronger than the variation of the mineral due to distant cation substitutions or the surface orientation. Thus, complexes at substituted sites are separately discussed as their geometric parameters tend to lie outside the range of variation determined for unsubstituted sites.

Adsorption at unsubstituted sites

In Table 26 geometry parameters of U(VI) adsorption complexes on (010), (110) and (100) edge surfaces of 2:1 dioctahedral clay minerals, averaged over various mineral models, and

Table 26. Averaged structural parameters^a of uranyl adsorption complexes on various sites of (010), (110) and (100) edge surfaces of various smectitemodel minerals. For comparison computational data for the solvated uranyl ion, as well as experimental data for montmorillonite are given. In parentheses the MAD is noted for calculated data and the coordination number for experimental ones.

Site	CN	U-O _t	U-O _s ^b	U-O _H	U-O _w	U-O _{eq}	U-Al ^c	U-Si ^c	E _{form}
UO ₂ (H ₂ O) ₂₀ ²⁺	5	183				240			
(010)									
AlOOH	5	186 (1)	203 (0)	241 (2)		260 (5)	245 (1)	323 (1)	165 (19)
AlOHOH	5	182 (0)	227 (1)	237 (1)		251 (4)	244 (1)	344 (1)	184 (39)
	5	184 (0)	238 (2)	240 (1)	219 (2)	258 (3)	243 (1)	348 (1)	144 (34)
AlO-SiO	4	187 (1)	205 (1)	224 (1)		246 (5)	230 (1)	337 (3)	151 (15)
AlOH-SiO	4	185 (1)	239 (4)	220 (2)	218 (3)	248 (3)	231 (2)	345 (3)	168 (26)
	5	184 (1)	245 (3)	228 (3)	221 (4)	260 (8)	243 (1)	353 (6)	151 (9)
AlO-SiOH	4	186 (0)	199 (0)	249 (5)		245 (4)	235 (0)	361 (4)	164 (28)
(110)									
AlO _m O	5	185 (1)	256 (6)	202 (1)		257 (5)	246 (1)	328 (1)	207 (23)
	4 ^d	185	235	202		261	240	329	212
AlO _m OH	5	182 (1)	259 (6)	233 (2)	226 (1)	251 (9)	244 (1)	351 (1)	164 (42)
SiOO _m	5	182 (0)	230 (3)	257 (4)	225 (2)	261 (7)	247 (0)	310 (2)	170 (31)
AlOH-SiO	4	183 (0)	227 (2)	217 (2)		245 (6)	233 (2)	359 (1)	127 (35)
	5	183 (1)	229 (3)	218 (1)		259 (9)	245 (1)	362 (1)	121 (20)
AlO-SiOH	4	185 (0)	199 (1)	246 (2)		247 (3)	235 (1)	376 (8)	144 (33)
	5	186 (1)	200 (1)	255 (3)		255 (6)	244 (2)	381 (6)	145 (34)
(100)									
AlOH-AlOH	4	182 (0)	230 (6)	233 (4)		235 (5)	233 (1)	380 (3)	36 (8)
SiO-SiO	4	185 (0)	217 (2)	218 (2)		242 (3)	230 (1)	354 (1)	92 (22)
AlOH-SiO	5	183 (1)	233 (5)	221 (5)		255 (7)	244 (2)	360 (6)	71 (25)
Exp.	pH								
Ref. 10	8	180(2.2)	230(3.1)			248(2.9)	239(6.0)	309(0.9)/328(0.9)	
Ref. 182	7	180(2.0)	232(2.8)			248(2.1)	234(5.0)	342(0.2)	
Ref. 139	6.6	179(2.3)	229(2.1)			247(2.1)	238(4.2)	331(0.6)	
Ref. 150	6.4	178(2.0)					236(6.2)	343(0.6)	
Ref. 138	5	177(2.0)	230(3.0)			248(2.7)	239(5.7)		
UO ₂ ²⁺ [101]	4	176(2)				241(5)			

^a Average terminal uranyl bond length U-O_t, bond lengths U-O_s to surface oxygen centers, U-O_H bond length to OH ligands, bond lengths U-O_w to aqua ligands, average equatorial U-O bond length U-O_{eq}, U-Al and U-Si distances to the nearest surface Al and Si centers. ^b The order of U-O_s bonds follows the site designation. ^c Only the relevant U-Al/Si distances for comparison with experiment, shorter than 370 pm or the shortest one are noted. ^d Only for montmorillonitic model.

their MADs are collected. For all sites inspected, the same type of adsorption complex was obtained by geometry optimization for various mineral models. A single exception represents the site AlO_mO on the (110) surface. For this site optimizations converged to five-coordinated UO₂²⁺ for pyrophyllite and beidellite, while a four-coordinated species was obtained for montmorillonite. Its five-coordinated congener turned out to be 21 kJ/mol less stable [129].

For most geometry parameters for various sites the MAD is rather small, amounting to a few pm only (Table 26). Larger MAD values are calculated for U-O_w bonds, for the longer

U-O_s bond lengths and for some U-Al/Si distances. The larger MADs of U-O_w bonds of up to 9 pm reflect the strong variation of individual U-O_w bonds between 235 pm and 295 pm, where the longest bonds show also the strongest variation between the different mineral models [129]. For U-O_s bond lengths the largest MADs are calculated for those ones which are longer than about 250 pm. This trend is understandable as for weaker and thus longer bonds a stronger variation of their lengths can be expected. A similar trend is found for the U-Al/Si distances. The longest ones of more than 365 pm for the AlOH-SiO site on the (110) and (100) surfaces show the largest MAD (Table 26). For the various surface complexes the uranyl bonds vary between 182 and 187 pm, U-O_s bonds between 199 and 259 pm, U-O_H bonds between 218 and 226 pm, U-O_w between 245 and 261 pm, and U-Al/Si distances between 323 and 381 pm. All these variations are considerably larger than the corresponding MADs determined for these geometry parameters. This result supports that the geometry of adsorption complexes is essentially determined by the sites and varies only slightly for different mineral models, as has been shown in detail for exemplary cases above. Thus, in the following we will characterize various adsorption complexes referring to geometries averaged over various mineral models. A corresponding average over surface orientations is less useful, as different surface orientations commonly exhibit different sites (Table 24).

The uranyl bonds of complexes at sites involving an AlO^{-3/2} surface group are longer, 185-187 pm, than for other adsorption complexes due to rather strong bonds U-O_s between uranyl and the AlO^{-3/2} group. The corresponding U-O_s bonds are also the shortest ones calculated, 199-205 pm (Table 26). For other sites inspected, involving a SiO⁻¹ group, but no AlO^{-3/2} group, uranyl bonds of 182 to 185 pm are obtained, together with U-O_s bonds of 217–230 pm. Sites involving none of these rather negatively charged groups yield relatively short U-O_t bonds of 182-184 pm and typically long U-O_s bonds of up to 259 pm (Table 26).

The U-O_s bond lengths to various surface groups correlate with the Pauling charges of the surface centers O_s involved (Table 23) [146]. Fig. 9 shows this correlation graphically for various sites of all smectite models inspected. At $q = -0.5 e$ the scattering of U-O_s bond lengths is wider than for other charges. The data exceeding the general trend stem from bonds to O_m centers of the (110) surface. Although the formal charge of O_m is $-1/2 e$ (Table 23), U-O_m bonds are longer, 256–259 pm, compared to typical values of 230–240 pm for AlOH^{-1/2} groups (Table 26), which carry the same formal O_s charge. As shown by ab initio molecular dynamics simulations, O_m is a weak proton acceptor [147]. Thus, the O_m center is expected to be less reactive compared to other O_s centers of similar formal charge and should exhibit weaker and longer bonds to uranyl. We confirmed this expectation by means of a refined effective charge analysis [57] using Bader charges [148] of the O_s atoms and empirical measures for the strengths of their bonds [149], which yields slightly different values for various O_s centers carrying the same empirical Pauling charge [57]. With this analysis we calculate charges of $-0.1e$ to $-0.4 e$ for AlOH groups and a little lower values of $-0.05 e$ to $-$

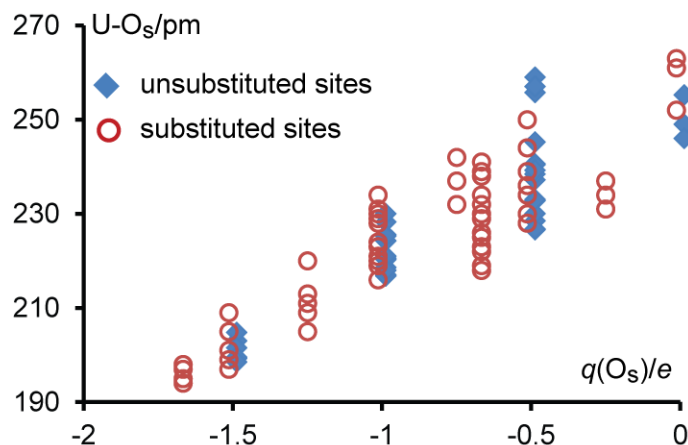


Figure 9. Calculated U-O_s bond lengths to surface oxygen centers of adsorption complexes of uranyl (VI) on pyrophyllitic, beidellitic, and montmorillonitic clay mineral (010), (110), and (100) edge surfaces as a function of the formal charge q of the surface oxygen centers O_s. Filled diamonds mark bonds of unsubstituted sites. Open circles represent the corresponding bonds for complexes at substituted sites. Overlying symbols are slightly shifted horizontally for easier discrimination.

0.25 e for O_m centers of unsubstituted sites, supporting the lower reactivity of these latter O_s centers.

The average equatorial U-O bond lengths U-O_{eq}, which are often measured by EXAFS, are calculated shorter, 230–240 pm, for four-coordinated and longer, 243–247 pm, for five-coordinated species due to bond competition (Table 26). The difference of U-O_{eq} between four- and five-coordinated adsorbates is larger than the MADs of this parameter. This shows that this parameter essentially depends on the CN and only weakly on the mineral, the surface orientation, or the adsorption site. This finding is already well known for actinide complexes [35,104] (Section 4.1.2)

As the U-O_s bonds, also U-Al/Si distances depend on the type of site. The shortest U-Al/Si distance, 310 pm, is calculated for the silanol site of the (110) surface (Table 26). U-Al distances of uranyl adsorbed on AlOOH sites of (010) surfaces and AlO_mO sites of (110) surfaces are similar, 323 pm and 328 pm, respectively. For adsorption complexes on AlOHOH sites on (010) surfaces and AlO_mOH sites on (110) surfaces, U-Al distances increase to 344 pm and 351 pm, respectively. The U-Si distance for uranyl adsorbed on deprotonated silanol groups varies between 337 and 362 pm. In all other cases, also for the long-bridge sites on the (110) surface, the U-Al/Si distances are longer.

Adsorption at substituted sites

Surface substitutions involving a site cation modify this adsorption site by increasing the formal charge of the O_s centers, see Table 24. For substituted sites the same species have been optimized as adsorbates as for the unsubstituted sites [129]. Due to substitution of the cation at an adsorption site, some of the U-O_s bonds shorten considerably [129]. As an example we mention U-O_s bonds of AlOH-AlO sites on beidellitic models of (110) and (010) surfaces.

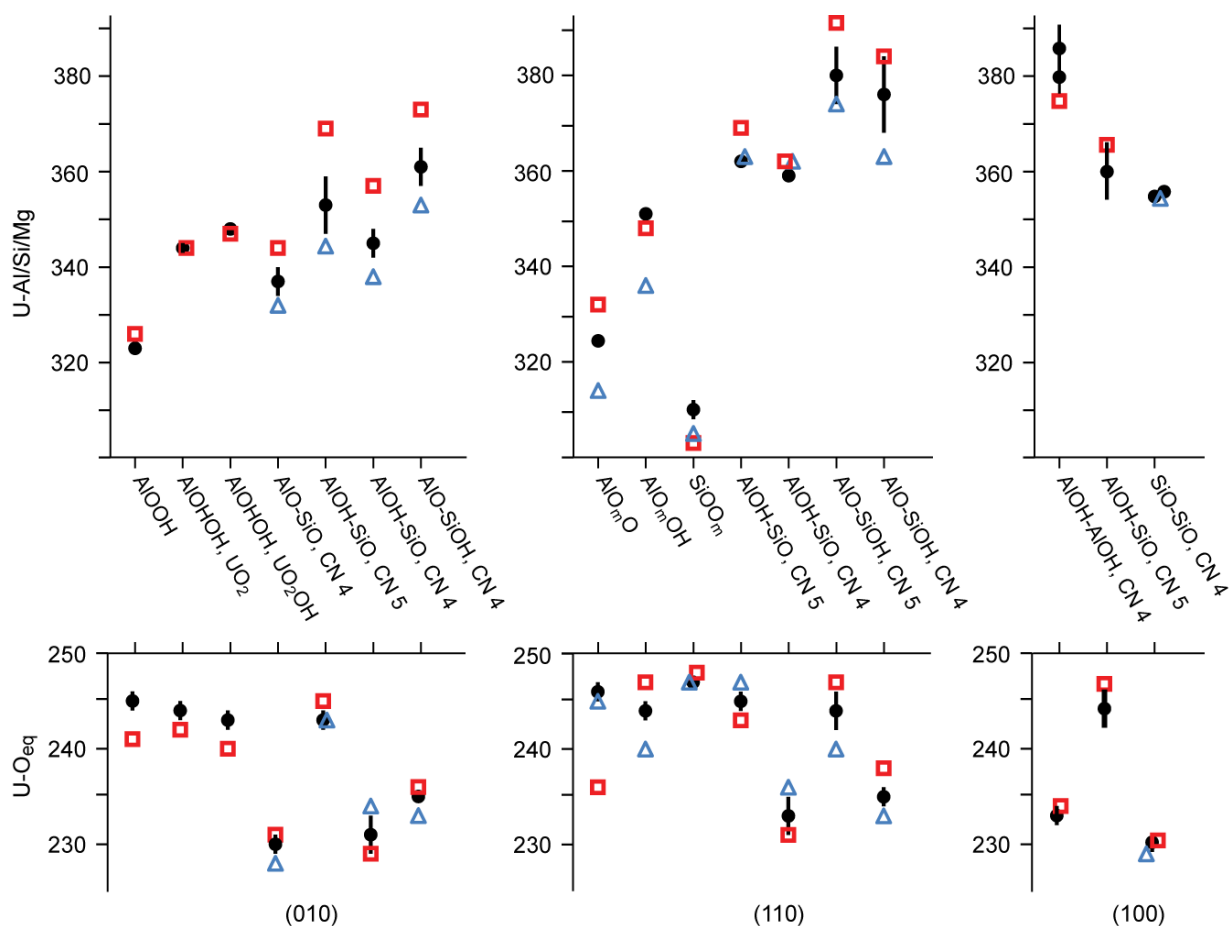


Figure 10. Average values of U-Al/Si and U-O_{eq} of uranyl(VI) adsorbed at various edge surfaces of smectite model minerals. Filled circles (black) mark averaged results for unsubstituted sites of various mineral models. Their MADs are shown as vertical bars. Open blue triangles and red squares mark results for substituted sites at beidellite and montmorillonite, respectively.

Due to the larger formal charge of O_s of the AlO^{-5/4} group, the U-O_s bonds to this surface group shorten to 205–211 pm, compared to the averages of 217–228 pm for corresponding unsubstituted SiO⁻¹ groups (Table 26). As for the unsubstituted sites, the U-O_s distances show in general a correlation with the formal charge of the oxygen centers of surface groups involved. (Fig. 9). The coefficients R² for separate linear fits of unsubstituted and substituted sites are 0.81 and 0.84, respectively. Also the slopes of the trend lines are very similar, 34.9 pm/e and 34.2 pm/e. Thus, the effect of site cation substitution on the rather ionic U-O_s bonds is essentially rationalized by the change of the formal charge of the site surface oxygen centers.

Effects of surface substitution on the structural parameters U-O_t and U-O_{eq} are rather small [129]. U-O_t mainly elongates by 1–2 pm due to substitution at the surface, as a result of a stronger interaction with the more negative site oxygen atoms (see above). The U-O_{eq} values change by at most 4 pm as consequence of surface substitutions (Fig. 10). As for unsubstituted sites, longer U-O_{eq} values are calculated for CN = 5 than for CN = 4. Variations due to the

type of mineral, surface orientation or site are smaller (Fig. 10). The only apparent exception shown in Fig. 10 for the substituted site MgO_mO on the montmorillonite (010) surface results is due to a coordination number of 4 for this specific site, as already observed for its unsubstituted analog AlO_mO (Table 26).

Effects of site substitutions on U-Al/Si/Mg distances vary with the site (Fig. 10). For aluminol sites the U-Al/Mg distance changes only slightly due to montmorillonitic substitution, by 4 pm at most. For the mixed sites the effect of the site substitution is typically larger, up to 16 pm, and opposite in sign for beidellitic and montmorillonitic models. When uranyl is adsorbed on $\text{MgO}(\text{H})\text{-SiO}(\text{H})$ sites of montmorillonite, the U-Si distances elongate due to substitution (Fig. 10). As an effect of the increased O_s charge of the $\text{MgO}(\text{H})$ group, the corresponding U- O_s bond shortens compared to the one to the aluminol group $\text{AlO}(\text{H})$. To balance this shortening, the second bond to the surface, U- O_s to $\text{SiO}(\text{H})$, elongates, which also entails an elongation of U-Si. For the beidellitic type of substitution, the substitution induced U-Al distances shorten compared to U-Si due to the considerable shortening of the U- O_s bonds to the aluminol groups replacing the silanol groups. For the example of U-Al/Si/Mg distances, Fig. 10 nicely illustrates again that geometry parameters for substituted sites are commonly outside the range determined for unsubstituted sites for various mineral models.

Thus, the main effect of cationic substitutions at the adsorption sites is a shortening of U- O_s bonds to O_s centers bound to substituted cations. Concomitant structural changes are an elongation of U- O_t and a shortening of corresponding the U-Al/Si/Mg distances. As these geometry changes, especially for the U-Al/Si/Mg distances, are in some cases large, the substituted sites contribute considerably to the range of geometry parameters of adsorbed uranyl on smectites that is to be expected.

Energies

We estimated the relative stabilities of the various adsorption complexes via their formation energies, calculated according to



Thus, E_{form} measures the energy of the exchange of two surface protons by the adsorbed uranyl.

Calculated formation energies of various adsorption complexes on the same surface vary by up to about 100 kJ mol^{-1} [129] (Table 26). The systems under study exhibit many soft degrees of freedom, especially in the water overlayer and due to bending modes of surface groups. This results in total energies which are rather sensitive to structural details, like the arbitrary arrangement of water molecules in the solvation layer. Thus, formation energies yield only a rough estimate and have to be interpreted with caution. To facilitate a comparison, we use formation energies for sites that are averaged over various minerals (Table 26), similar to our approach to geometry parameters.

All formation energies are positive, as they include the twofold deprotonation of the adsorption site (Table 26). This deprotonation energy is higher than the adsorption energy in absolute value, as the binding of two protons is more flexible than the coordination of the uranyl ion to the surface. The average values of E_{form} vary between 144 kJ/mol and 184 kJ/mol for the sites on the (010) surfaces. For the more open (110) surface the energy values fall into the wider interval from 121 kJ/mol to 212 kJ/mol. Thus, both surfaces provide sites of similar complex formation energies (Table 26). Lower energies are calculated for exemplary sites on the (100) surface, varying between 36 and 91 kJ/mol. As lower formation energies are pointing to more favorable sites, one may consider AlOH₂OH, AlO-SiO, and AlOH-SiO sites on the (010) surface, the AlOH-SiO site on the (110) surface and the AlOH-AlOH site on the (100) surface as candidates for preferred adsorption sites, which includes uranyl and uranyl monohydroxide as adsorbates on the (010) surface. (Table 26). A refinement of formation energies by a dynamic approach is discussed in a later subsection for the example of the (110) surface of smectite mineral models.

To classify sites one may in addition to the formation energies also refer to the intrinsic pK_a values of various OH groups on edge surfaces of 2:1 clay minerals, that were recently estimated for the (010) and (110) surfaces [140,142]. SiOH and AlOH₂^{+1/2} groups were shown to be the most acidic surface groups on (010) surfaces, both with pK_a values of about 7. The pK_a of a AlOH^{-1/2} surface group was estimated at 22.4. The acidity of the substituted surface groups MgOH₂^{+1/3} and AlOH^{-1/4} were calculated higher by at least 3 pK_a units than those of the corresponding aluminol and silanol surface groups.¹⁵ Thus, unsubstituted sites with SiO⁻ and AlOH^{-1/2} groups are more likely on the (010) surface. Similarly, AlOH₂^{+1/2} surface groups on (110) surfaces exhibit the lowest pK_a , ~5.5, while silanol groups show an acidity constant of ~7.^{13, 15} Thus, SiOH and AlOH₂^{+1/2} groups will most probably deprotonate first, while AlO^{-3/2} surface groups are expected to be much less likely. For the (100) surface no acidity constants were calculated, but the similarity of the surface groups compared to other surface orientations allows to assume the same order of deprotonation of various groups. Thus, first AlOH-AlOH sites, then AlOH-SiO, and then SiO-SiO sites are expected to appear with increasing pK_a . Taking together formation energies and site deprotonation energies, AlO_mOH, AlOH₂OH, AlOH-AlOH, AlOH-SiO, and SiO-SiO sites can be regarded as the more probable ones on various edge surfaces of smectites.

Comparison to experiment

Montmorillonite is the most commonly studied 2:1 clay mineral in experiments on uranyl adsorption [10,138,139,150,151]. To the best of our knowledge there are no experimental studies on U(VI) adsorption on pyrophyllite or beidellite. Thus, we compare our results on smectite models with EXAFS studies on montmorillonite that have been carried out in N₂ or Ar atmosphere to avoid complexes with carbonate [10,138, 139, 150,151] (Table 26).

As GGA functionals tend to overestimate bond lengths, differences are reproduced more accurately than absolute bond lengths. Thus, we compare our results for adsorption

complexes of uranyl with uranyl in solution, optimized at the same level of theory, but with the second solvation shell included explicitly in the model aqua complex. For solvated uranyl(VI) we calculated U-O_t bonds of 183 pm, overestimating the experiment, and an U-O_{eq} value of 240 pm, in agreement with experiment (Table 26). In EXAFS experiments the elongation of U-O_t bonds due to adsorption is determined to 1–4 pm [10,138,139,150]. We calculated an elongation of U-O_t by up to 4 pm (Table 26), where the longest bonds are obtained when uranyl is bound to an AlO^{-3/2} surface group, in good agreement with experiment.

Average equatorial U-O bond lengths U-O_{eq} of 234 to 239 pm were measured by EXAFS [10,138,139,151]. These values are a little shorter than the experimental results for solvated uranyl of 241 pm [101], which fits very well our calculated result (Table 26). As discussed above, U-O_{eq} mainly depends on the coordination number. We calculated typical ranges of 230-235 pm for CN = 4 and of 243-247 pm for CN = 5 (Table 26). These results are shorter for CN = 4 and longer for CN = 5 than the experimental range and suggest a mixture with CN = 4 prevailing. In some EXAFS experiments [10,138,139,151], two equatorial U-O distances have been fitted [10,138,139,151]. The shorter one of about 230 pm is commonly attributed to U-O bonds to the surface, while the longer one of about 248 pm is assigned to bonds to aqua ligands (Table 26). Our results show rather short U-O bond lengths of about 200 pm to AlO groups, which are thus improbable due to their high deprotonation energy (see above). Bonds to SiO groups are calculated to 215-230 pm. Bonds to AlOH groups amount to 227-245 pm. Both are compatible with the shorter measured U-O bonds. On the other hand, U-O_H bonds of 218-225 pm have been calculated (Table 26), which fit as well. Longer U-O bonds, in the range of the experimental result of about 248 pm, have been calculated for SiOH groups, O_m centers, as well as for aqua ligands (Table 26). Thus, the current interpretation of available EXAFS results is extended by our results, in agreement with earlier findings for uranyl adsorption on kaolinite [137].

Useful structure parameters for discriminating sites are the distances between U and the surface cations, Al, Si, or Mg. Experimentally these rather long distances, measured by various groups at ~310 pm and between 330 and 345 pm [10,139,150,151], are not easy to interpret. Taking into account that U-Al/Si distances do not represent chemical bonds, that they are in a region of multiple scattering, and that U-Al/Si distances are experimentally not always observed, there is some uncertainty. The shortest distance from uranium to a cation, ~310 pm, was calculated for uranyl adsorption at silanol SiOO_m sites on (110) surfaces (Table 26) or for their substituted analogue AlO_{Al}O. This value is in agreement with the experimental result of 309 pm [10]. The measured distances of around 330 pm can be interpreted as U-Al distances for uranyl adsorbed at aluminol sites, AlO_mO or AlOOH (Table 26), which are regarded as less probable (see above). According to our model results, distances between U and surface cations of 340–350 pm correspond to U-Al for adsorption on AlOH₂ sites of the (010) surface or AlO_mOH sites of the (110) surface or to U-Si for adsorption on mixed

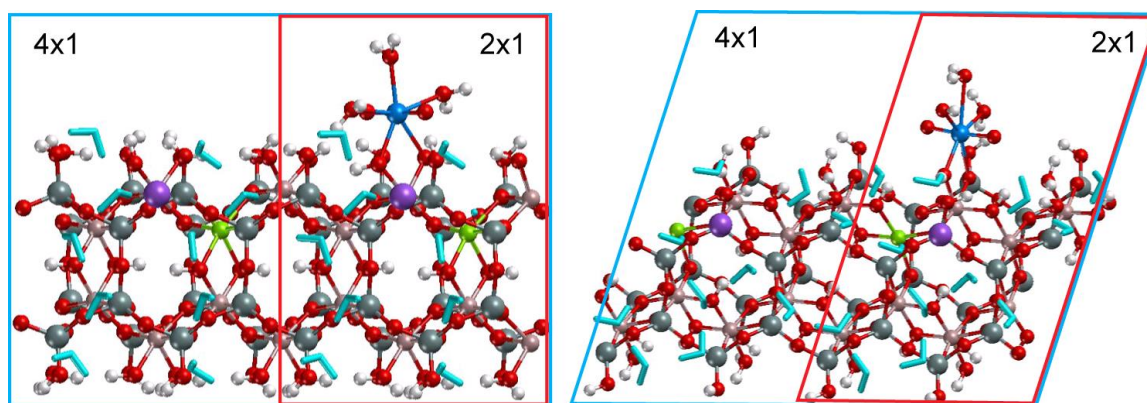


Figure 11. Exemplary adsorption complexes on the AlOH(OH) site of the (010) surface (left) and the AlO_mOH site of the (110) surface (right) of montmorillonite with inner substitution. 2×1 and 4×1 surface unit cells are marked by red and blue boxes, respectively. Interlayer water is represented as stick model and water of the solvation layer is omitted for clarity. Uranium is represented blue, for the color coding of other elements see Fig. 6.

AlOH-SiO sites of (010) surfaces. Also U-Si for the SiO-SiO site at the (100) surface with 354 pm close to that range (Table 26).

Thus, the best agreement with experiment exhibit calculated data for complexes adsorbed on sites that involve AlOH^{1/2}, O_m, and/or SiO(H) surface groups. Coexistence of adsorption complexes with CN = 5 and 4 is suggested with a prevalence for CN = 4 to be in agreement with experimental U-O_{eq} values. The experimentally observed U-Al/Si distances are reproduced well for uranyl adsorbed on edge sharing Si tetrahedral (SiO_mO) and Al octahedral sites (AlO(H)OH, AlO_mO). Also U-Si distances calculated for adsorption complexes at AlOH-SiO and SiO-SiO sites are close to experimental findings. From this comparison we conclude that several adsorption sites, largely determined by the deprotonation state of the surface, are available for uranyl(VI) adsorption. Thermodynamic models of actinide adsorption at clay mineral surfaces, assuming essentially the existence of strong and weak adsorption sites [8,10], seem to be an approximation only, as according to our calculations a larger set of sites at various edge surface orientations should exist.

Effect of coverage

For the most probable sites determined by optimization we tested the effect of coverage by varying the unit cell size. As the properties of adsorption complexes depend only weakly on the smectite model, we chose the montmorillonite model with inner defects as example. On the (010) surface AlOH(OH) and AlOH-SiO sites and on the (110) surface AlO_mOH, SiOO_m, and AlOH-SiO sites were investigated as examples. The 2×1 surface unit cells, where the first surface lattice vector is a combination of the bulk vectors *a* and *b* and the second one is *c*, with an area of about 10×13 Å², as used in our survey study on uranyl adsorption on edge surfaces of smectites, were doubled along the mineral sheets, resulting in 4×1 surface unit cells with an area of about 20×13 Å². In this way the distance between the adsorbates along the mineral sheet is doubled (Fig. 11).

Table 27. Comparison of structural parameters (see Table 26, in pm) and formation energies (in kJ/mol) of uranyl(VI) adsorption on edge surface models of montmorillonite with inner substitutions for 2×1 and 4×1 surface unit cells and a layer charge of $-0.25 e$ for exemplary surface complexes.

Surface/Site	Adsorbate	Cell	U-O _t	U-O _s ^a	U-O _H	U-O _{eq}	U-Al/Si	E _{form}
(010)								
AlOH _{OH}	UO ₂ ²⁺	2×1	182	227/237		241	346	128
		4×1	185	228/239		242	345	144
AlOH-SiO	UO ₂ OH ⁺	2×1	185	234/242	217	240	349	101
		4×1	185	237/237	217	241	348	95
	UO ₂ ²⁺	2×1	183	252/219	228	244	361	136
		4×1	183	250/213	221	246	357	138
		4×1	182	235/230		244	364	108
(110)								
AlO _m OH	UO ₂ OH ⁺	2×1	181	247/232	226	247	352	213
		4×1	181	247/231	228	246	352	98
SiOO _m	UO ₂ OH ⁺	2×1	182	225/261	229	248	311	221
		4×1	184	223/252	230	245	306	160
AlOH-SiO	UO ₂ ²⁺	2×1	183	225/219		245	359	160
		4×1	184	224/216		247	362	68

^a The order of U-O_s bonds follows the site designation.

Structural parameters and formation energies of uranyl adsorbed at various sites are collected in Table 27 for the two surface unit cells chosen. The main structural parameters of the adsorption complexes in most cases do change only marginally when comparing results obtained with 2×1 and 4×1 unit cells. Increased uranyl bonds for the AlOH_{OH} site on the (010) surface and the SiOO_m site on the (110) surface as well as shortened U-O_H bonds for the AlOH-SiO site on the (010) surface due to the larger unit cell size are traced back to a rearrangement of the solvation layer. The strongest change of the structure of adsorbed uranyl is observed for the (010) surface on the AlOH-SiO site. While in the smaller unit cell only uranyl monohydroxide had been obtained as adsorbate, in the larger one also UO₂²⁺ was successfully optimized. This new adsorbate for this site is calculated to be slightly more stable, by 30 kJ/mol.

Formation energies calculated for both unit cells of the (010) montmorillonite edge surface model are similar. They differ by at most 16 kJ/mol for the same site when the unit cell size is doubled. On the (110) surface the results for the 4×1 unit cell are lower, by about 60–100 kJ/mol, than for the 2×1 unit cell. Taking into account the strong variation of formation energies due to the arbitrary structure of the solvation layer, at best a tendency to stronger adsorption for lower coverage may be inferred, in line with an electrostatic repulsion of the adsorbates.

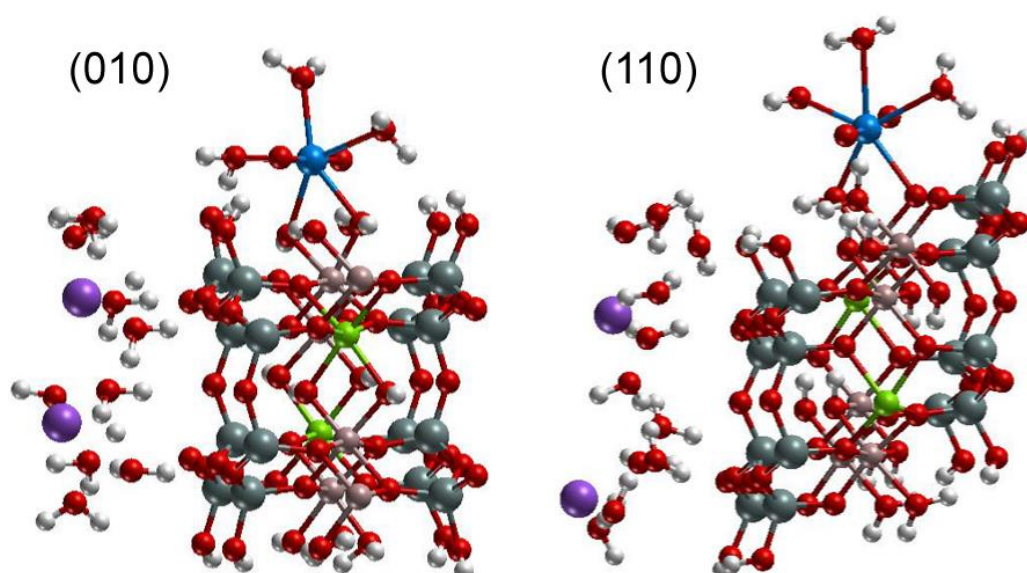


Figure 12. Adsorption complexes of uranyl on aluminol sites of (010) and (110) montmorillonite model surfaces with inner octahedral substitutions and a layer charge $q = -0.5 e$. Water molecules of the solvation layer are omitted for clarity.

Variation of layer charge

In order to test how the charge of the mineral layer affects the adsorption of uranyl we created two types of surface models with a layer charge $q = -0.5 e$ to compare the results for an exemplary set of adsorption complexes on montmorillonite to the corresponding findings in our survey study based on smectite models with a layer charge of $-0.25 e$. To achieve an increased layer charge, we substituted in the first model one more inner Al^{3+} cation by Mg^{2+} and introduced a second Na^+ counter ion in the interlayer space. We inspected the effect of the layer charge for exemplary more likely sites of the (010) and (110) surfaces with inner substitutions. Fig. 12 shows exemplary slab models with $q = -0.5 e$.

For all adsorption complexes at the same site for the layer charges $q = -0.25 e$ and $-0.5 e$ the inspected geometry parameters and formation energies are in most cases very similar (Table 28). The largest geometry changes of a few pm are obtained for longer and thus weaker U-O_s bonds, e.g. for UO_2^{2+} at the AlOH_2OH site of the (010) surface and for UO_2OH^+ at the SiOO_m site of the (110) surface, as well as for some U-Al/Si distances, which do not represent chemical bonds. Also the formation energies typically vary by about 10 kJ/mol or less. This weak perturbation of the adsorption complexes due to a change of the layer charge results from the fact, that the additional charge introduced has been placed well below the surface and relatively far from the adsorbate (Fig. 12). These findings support the validity of our results achieved with mineral models with a layer charge of $-0.25 e$.

As a second example, we introduced a tetrahedral substitution of Si^{4+} by Al^{3+} on the surface of our montmorillonite models. The negative charge of this substitution was neutralized by a proton adsorbed on the surface leading to an additional AlOH_2 surface group. Fig. 13 shows exemplary optimized adsorption complexes with various positions of

Table 28. Comparison of structural parameters (see Table 26, in pm) and formation energies (in kJ/mol) of uranyl(VI) adsorbed on a edge surfaces of montmorillonite with one ($q = -0.25 e$) or two ($q = -0.5 e$) inner octahedral substitutions (Fig. 12).

Surface/Site	Adsorbate	q	U-O _t	U-O _s ^a	U-O _H	U-O _{eq}	U-Al/Si	E _{form}
(010)								
AlOH-OH	UO ₂ ²⁺	-0.25	182	227/237		241	346	128
		-0.5	182	228/244		241	346	82
	UO ₂ OH ⁺	-0.25	185	234/242	217	240	349	101
		-0.5	185	235/242	217	240	348	108
AlOH-SiO	UO ₂ OH ⁺	-0.25	183	252/219	228	244	361	136
		-0.5	184	252/218	227	243	357	124
(110)								
AlO _m OH	UO ₂ OH ⁺	-0.25	181	247/232	226	247	352	213
		-0.5	181	246/232	226	247	349	212
SiOO _m	UO ₂ OH ⁺	-0.25	182	225/261	229	248	311	221
		-0.5	182	228/258	229	248	309	218
AlOH-SiO	UO ₂ ²⁺	-0.25	183	225/219		245	359	160
		-0.5	183	226/217		245	360	161

^aThe order of U-O_s bonds follows the site designation.

Table 29. Comparison of structural parameters (see Table 26, in pm) and formation energies (in kJ/mol) of uranyl(VI) adsorbed on a montmorillonite (010) model surface with inner and surface octahedral substitution ($q = -0.25 e$) with a model surface with an additional tetrahedral substitution ($q = -0.5 e$) (Fig. 13).

Site	Ads./CN	q	U-O _t	U-O _s ^a	U-O _H	U-O _{eq}	U-Al/Si/Mg	E _{form}
Inner subst.								
AlOH-OH	UO ₂ ²⁺ /5	-0.25	182	227/237		241	346	128
		-0.5	183	224/229		242	343	97
	UO ₂ OH ⁺ /5	-0.25	185	234/242	217	240	349	101
		-0.5	185	230/239	217	241	348	99
AlOH-SiO	UO ₂ OH ⁺ /5	-0.25	183	251/227	227	246	364	167
		-0.5	185	261/218	232	245	362	127
AlOH-SiO	UO ₂ OH ⁺ /4	-0.25	186	235/217	224	230	351	139
		-0.5	187	237/210	226	230	354	140
Surf subst.								
MgOH-OH	UO ₂ ²⁺ /5	-0.25	183	222/230		242	344	182
		-0.5	184	222/227		242	345	106
	UO ₂ OH ⁺ /5	-0.25	186	230/234	219	240	347	175
		-0.5	186	226/233	219	240	348	129
MgOH-SiO	UO ₂ OH ⁺ /5	-0.25	183	239/234	226	245	369	180
		-0.5	184	252/219	234	244	369	146
MgOH-SiO	UO ₂ OH ⁺ /4	-0.25	186	226/220	224	229	357	165
		-0.5	187	233/214	223	230	356	107

^aThe order of U-O_s bonds follows the site designation.

substitutions inspected. Table 29 collects structural parameters and formation energies for the two sites inspected, the AlOH-OH site and the AlOH-SiO site, together with their surface substitution induced analogs AlOH-AIO, MgOH-OH, MgOH-SiO and MgOH-AIO.

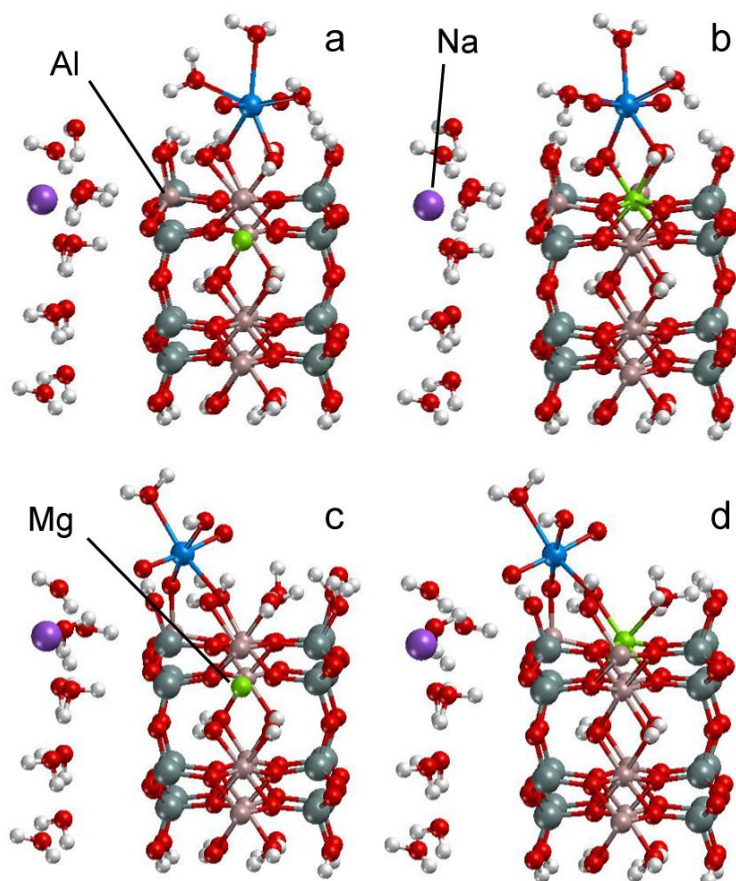


Figure 13. Exemplary adsorption complexes of uranyl on montmorillonite (010) surfaces with an additional beidellitic substitution. Adsorption on (a) AlOH-OH site, surface with deep substitution; (b) MgOH-OH site, surface substitution; (c) AlOH-AlO site, deep substitution; (d) MgOH-AlO site, surface substitution. Water molecules of the solvation layer are omitted for clarity.

Comparison of the geometry parameters shows only small variations for the sites AlOH-OH and MgOH-OH due to the introduction of the tetrahedral surface substitution, as this substitution does not modify the chemical groups forming the sites. Uranyl bonds $U-O_t$ vary by at most 1 pm, $U-O_s$ bonds by up to 3 pm, $U-O_H$ bonds to OH ligands by less than 1 pm, and $U-O_{eq}$ by at most 1 pm (Table 29). Even the shorter $U-Al/Si/Mg$ distances essentially stay constant. The only notable effect of the increased negative layer charge is a tendency to lower formation energies and thus more stable adsorption, by up to about 80 kJ/mol (Table 29). When the tetrahedral substitution modifies the adsorption site, which leads from the sites AlOH-SiO and MgOH-SiO to AlOH-AlO and MgOH-AlO, typical effects of the negatively charged defect introduced by the substitution are observed. The bonds to the AlO group replacing the SiO group shorten by up to 16 pm. These stronger bonds to the surface lead to longer uranyl bonds, by up to 2 pm, and longer bonds to OH ligands, by up to 6 pm, due to bond competition. $U-O_{eq}$ stays essentially unaffected, as this averaged parameter depends mainly on the coordination number (see above). Interestingly, $U-Al/Si/Mg$ distances are affected only marginally. As for the sites on mineral models without surface substitution

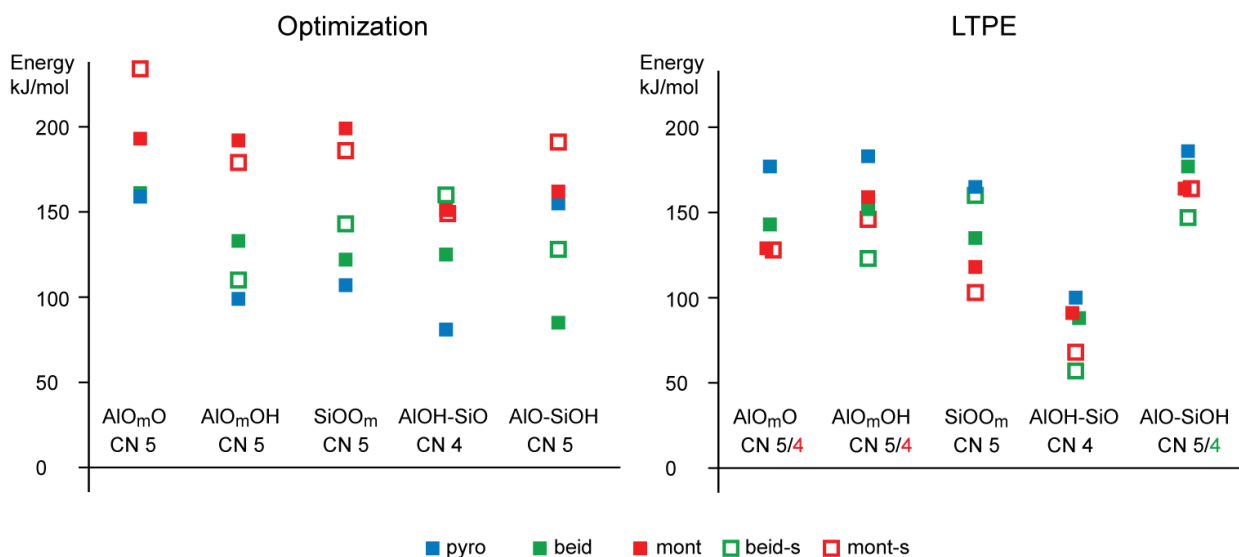


Figure 14. Formation energies of uranyl adsorption complexes at various sites of (110) edge surfaces of smectite mineral models (filled squares: pyro = pyrophyllite; beid = biedellite; mont = montmorillonite; open squares: s = surface substituted) as determined by optimization (left) and low temperature partial equilibration (right).

(Table 28), a tendency to lower formation energies is calculated when comparing results for surface models with $q = -0.25 e$ and $-0.5 e$. Contrary to expectation, this stabilization of the adsorption complex due to a second surface substitution is not stronger than for unsubstituted sites. Thus, although these results confirm the general expectation that a more negative surface binds uranyl more strongly, the effect of a local substitution on the formation energy is hidden due to the arbitrary structure of the explicit solvation layer, as will be shown in the next subsection.

Equilibration of the solvation layer and improved energies

As discussed above, energies of adsorption complexes on solvated surfaces, as determined by simple geometry optimization, show fluctuations due to the arbitrary structure of the explicit solvation layer [129]. To overcome this problem we developed a low temperature partial equilibration procedure [57] (LTPE, Section 4.3.1), circumventing a fully dynamic treatment, which is computationally rather costly. This approach to achieve an approximately equilibrated solvent structure allows an efficient and systematic study of various adsorption complexes. To validate this new approach, we inspected uranyl(VI) adsorption on the (110) edge surface of model smectite minerals as an exemplary case and compared the results to those obtained by conventional optimization.

We used the optimized adsorption complexes discussed above as initial structures for the LTPE procedure. We confirm most of the adsorbed species obtained earlier for the five sites treated on five models of the (110) surface (Fig. 14), with only a few exceptions [57]. A change from UO_2OH^+ to UO_2^{2+} as adsorbate appeared for the tetrahedrally substituted site $\text{AlOO}(t)$ of beidellite. Substituted sites in some cases showed changes of the CN of the adsorbate from 5 to 4. As a result, $\text{CN} = 4$ is as common as $\text{CN} = 5$ for adsorption on the

substituted sites of 2:1 model smectites [57]. This trend is explained by a stronger bonding of the adsorbate to the substituted sites, which leads to a weakening of the aqua ligand bonds. Structural parameters of adsorption complexes obtained by the LTPE procedure are very similar to the ones determined by optimization. Uranyl bonds changed typically by less than 1 pm, U-O_{eq} by 2 pm at most, and other parameters, like the soft bonds to water ligands or U-Al/Si/Mg distances, by at most 5 pm when averages over mineral models are compared [57]. Thus, these more accurate exemplary calculations confirmed the essential finding, that structural characteristics are mainly determined by the type of site and rather independent of the type of mineral and also support the interpretation of EXAFS results as given above.

In Fig. 14 we compare formation energies of uranyl adsorption as determined by optimization without and with equilibration by means of LTPE. Results of simple optimization show no clear trends [129]. There is only a weak tendency for formation energies on pyrophyllite to be lower than for charged minerals, which contradicts the expectation that negatively charged surfaces should bind cations stronger. Also substituted sites, which are more negative, show no enhanced binding for uranyl compared to others (Fig. 14). Equilibration of the solvation layer by LTPE leads to formation energies showing clearly the influence of electrostatics on uranyl binding. The highest formation energies (weakest binding) are determined for the neutral pyrophyllite surface. Unsubstituted surfaces of montmorillonite and beidellite yield as expected by up to 34 kJ/mol lower formation energies, which are rather similar (Fig. 14). For adsorption on substituted sites, a clear tendency to lower formation energies compared to unsubstituted ones is calculated with the exception of the AlOO(t) site (see below). Interestingly, comparing various sites, the AlOH-SiO site is favored on the (110) surface for all mineral models (Fig. 14).

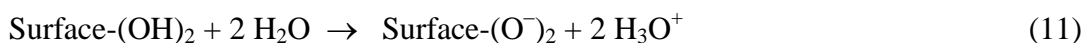
To rationalize this finding we estimated adsorption energies of uranyl on deprotonated (110) model surfaces of 2:1 smectites [57]. The adsorption energy E_{ads} of a uranyl aqua complex on a twofold deprotonated surface site is the reaction energy of the process



As Eq. (9) implies a charged unit cell, it cannot be used directly. Instead, we determine the adsorption energy of uranyl at various sites as the difference

$$E_{\text{ads}} = E_{\text{form}} - E_{\text{depr}} \quad (10)$$

where the site deprotonation energy E_{depr} is defined as the energy of the reaction



We estimate site deprotonation energies in a single point fashion by moving two protons of the surface of interest to one and the same preoptimized site at the bottom of the surface model. From these model energies we determine relative deprotonation energies with respect to the site with lowest deprotonation energy. To obtain absolute energies, we estimate the deprotonation energy of the reference site for each surface as the sum of group deprotonation

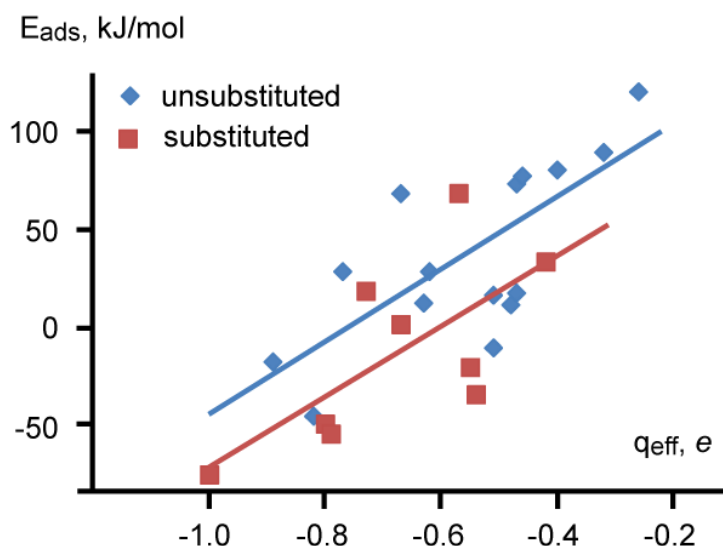


Figure 15. Uranyl(VI) adsorption energies on (110) edges surfaces of model smectites as a function of the effective charges of the corresponding adsorption sites.

Table 30. Calculated formation energies E_{form} and estimated site deprotonation and adsorption energies E_{depr} and E_{ads} (in kJ/mol) as well as effective charge q_{eff} (in e) of various adsorption sites on (110) edge surfaces of 2:1 model smectites.

Model	Site	E_{form}	E_{depr}	E_{ads}	q_{eff}	Site	E_{form}	E_{depr}	E_{ads}	q_{eff}
Pyro	AlO_mO	177	108	69	-0.68					
Beid		143	160	-17	-0.90					
Mont		129	174	-45	-0.83	MgO_mO	128	203	-75	-1.01
Pyro	AlO_mOH	183	62	121	-0.27					
Beid		152	62	90	-0.33	AlOOH(o)	123	89	34	-0.43
Mont		159	78	81	-0.41	MgO_mOH	146	77	69	-0.58
Pyro	SiOO_m	165	91	74	-0.48					
Beid		135	117	18	-0.48	AlOO(t)	160	158	2	-0.68
Mont		118	106	12	-0.49	SiOO_m	103	123	-20	-0.56
Pyro	AlOH-SiO	100	71	29	-0.63					
Beid		88	75	13	-0.64	AlOH-AlO	57	111	-54	-0.80
Mont		91	62	29	-0.78	MgOH-SiO	68	117	-49	-0.81
Pyro	AlO-SiOH	186	108	78	-0.47					
Beid		177	160	17	-0.52	AlO-AlOH	147	128	19	-0.74
Mont		164	174	-10	-0.52	MgO-SiOH	169	203	-34	-0.55

energies [57] as determined recently by an accurate first principles molecular dynamic approach [144]. Deprotonation energies estimated in this way are collected in Table 30.

Adsorption energies E_{ads} at specific sites are typically more endothermic for pyrophyllite than for montmorillonite and beidellite (Table 30), as expected due to the negative layer charge of the latter mineral models. For most mineral models, substituted sites

are calculated to be more favorable than their unsubstituted analogues (Table 30). These trends confirm the expectation that the binding of the uranyl ion to a clay mineral surface has a notable ionic character. Thus, the adsorption energies are expected to correlate with the charge of the adsorption site. To inspect this correlation, we estimated site charges by an extension of the Pauling scheme [57]. Instead of formal valences and bond strength values, as in the Pauling scheme, we used Bader charges [148] of the oxygen centers and an empirical measure for the cation-oxygen bond strength, borrowed from the bond-valence method [149]. These novel effective charges of oxygen centers allow to differentiate groups that are characterized by identical Pauling charges. Site charges (Table 30) are then determined by the sum of the effective charges of the oxygen centers of the groups involved. Fig. 15 illustrates the correlation between the effective site charges and the corresponding adsorption energies. This only weak correlation ($R^2 = 0.56$) may in part be due to the approximate way of estimating site deprotonation energies. The trend lines in Fig. 15 show that adsorption on substituted sites is about 30 kJ/mol more favorable compared to adsorption at unsubstituted sites, concomitant with the more negative charges of the former sites.

Two factors, easy deprotonation and a strong negative charge of the resulting adsorption site, lead to the most favorable adsorption complexes on (110) smectite surfaces. AlO_mOH and AlOH-SiO sites and their substituted analogues exhibit the lowest deprotonation energies of all surface models (Table 30). However, the effective charges of the AlOH-SiO sites are $\sim 0.3 e$ more negative than those of the AlO_mOH sites. This difference rationalizes the energy preference for adsorption at AlOH-SiO sites when a protonated surface is taken as reference (Fig. 13). Low adsorption energies are also calculated for AlO_mO and AlO-SiOH sites. Nevertheless, adsorption at these sites is improbable at about neutral pH conditions as the AlO group is involved, which might appear only at higher pH due to the high deprotonation energy needed to create it (Table 30).

The refined energy results for uranyl adsorption at the (110) edge surfaces of smectite model minerals allow also a slight improvement of our interpretation of experimental results. In general, substituted sites have to be regarded as favorable compared to their unsubstituted congeners. As Fig. 14 shows, formation energies of other substituted sites are rather close to the ones for the preferred AlOH-SiO site for the (110) surface for various mineral models. Taking into account that for other edge surface orientations other sites may be comparable in energy, still a set of sites, preferably including AlOH and SiO groups, will be occupied by adsorbed uranyl.

Adsorption at Fe surface substitutions

The well known strong variability of the composition of smectites is not only due to the number and distribution of charged substitutions of octahedral Al^{3+} by Mg^{2+} (montmorillonitic) and tetrahedral Si^{4+} by Al^{3+} (beidellitic), which have been considered so far. Also neutral and charged substitutions of Al^{3+} cations by Fe^{3+} (or Fe^{2+}) are rather common [127] and contribute to the variability of these clay minerals. Thus, long U-cation distances of

Table 31. Structural parameters^a (see Table 26, in pm) and formation energies E_{form} (in kJ/mol) for uranyl(VI) adsorption on various sites of (110) edge surfaces of montmorillonite without and with surface Fe^{3+} substitutions, as obtained from calculations with PCM solvation modeling.

Site	CN	U-O _t	U-O _s ^b	U-O _H	U-O _w	U-O _{eq}	U-Al/Fe	U-Si	E_{form}	
AlO _m O	5	183	251	208		255	245	333	69	
FeO _m O	5	183	246	210		255	244	335	48	
AlO _m OH	5	182	262	236	215	255	244	355	60	
FeO _m OH	5	183	256	237	215	255	244	357	54	
SiOO _m	5	182	226	260	225	255	244	308	42	
SiOO _m	5	182	229	252	225	256	243	308	30	
AlOH-SiO	4	183	228	217		243	233	354	33	
FeOH-SiO	4	183	226	218		242	232	356	25	
AlOH-SiO	5	183	231	217		256	243	356	50	
FeOH-SiO	5	183	230	218		256	243	360	20	
AlO-SiOH	4	185	199	247		247	235	379	374	100
FeO-SiOH	4	184	200	248		247	235	384	378	82
AlO-SiOH	5	185	200	261		255	245	383	390	106
FeO-SiOH	5	184	201	262		254	245	389	395	90

^a Average terminal uranyl bond length U-O_t, bond lengths U-O_s to surface oxygen centers, U-O_H bond length to OH ligands, bond lengths U-O_w to aqua ligands, average equatorial U-O bond length U-O_{eq}, U-Al/Fe and U-Si distances to the nearest surface cation centers. ^b The order of U-O_s bonds follows the site designation.

343 pm, as measured for uranyl adsorption on montmorillonite by EXAFS, have been interpreted as either U-Al [150] or U-Fe [151] distances. To inspect the influence of Fe^{3+} substitutions we considered the exemplary case of octahedral Fe^{3+} surface substitutions for the (110) edge surface of montmorillonite. In these calculations we applied a recently developed PCM model for surfaces [37] (Section 4.3.2) to treat surface solvation. To account for self-interaction errors of DFT in order to obtain the correct spin state of Fe ions, the DFT+U approach [152] is applied, using a U parameter of 4.5 eV.

Table 31 shows optimized geometry parameters and formation energies for adsorbed uranyl comparing sites without and with Fe^{3+} surface substitution. Overall, only small geometry changes are calculated. The largest changes are observed for U-O contacts to O_m centers, which shorten due to iron substitution by up to 8 pm. This effect may be rationalized by the higher electronegativity of Fe^{3+} compared to Al^{3+} , decreasing the ionic character of the Fe-O bond compared to Al-O, thus increasing the donor capability of O towards uranyl. In all cases, U-O_m bonds are the longer and thus weaker ones of the corresponding bidentate adsorption complexes. The other U-O_s bond for these sites elongates by up to 3 pm due to bond competition (Table 31). All other geometry parameters are essentially unaffected, showing that a neutral substitution only marginally affects the geometry of uranyl adsorption complexes. The measured U-Al/Fe distances of 343 pm of ambiguous assignment [150, 151]

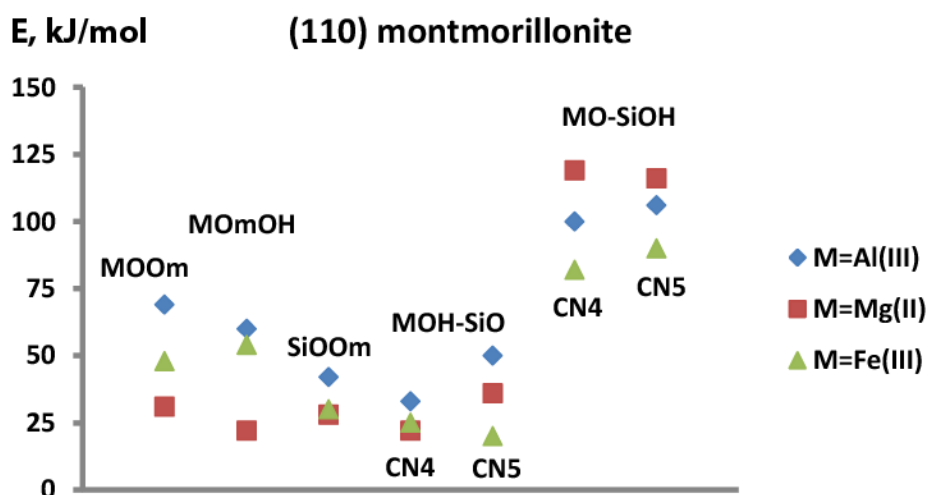


Figure 16. Formation energies of various uranyl(VI) adsorption complexes on the (110) surface of montmorillonite with surface solvation modeled by PCM. Compared are unsubstituted sites (blue diamonds) to sites including octahedral surface substitution by Fe(III) (red squares) and Mg(II) (green triangles).

may tentatively attributed to adsorption at (Al,Fe) O_m OH and (Al,Fe)OH-SiO sites, although our calculated values are by about 10 pm larger (Table 31). According to our calculations, distances to octahedral Al and Fe cations can hardly be distinguished experimentally, as U-Fe only weakly increases compared to U-Al by up to 5 pm (Table 31).

In Fig. 16 we compare formation energies of uranyl adsorption complexes for unsubstituted sites, Mg substituted sites, and sites including the neutral iron substitution. For all sites we observe a stabilization of the complexes due to iron substitution, supporting a strengthening of the bond to uranyl. In most cases this stabilization is weaker for Mg substituted sites, which show increased effective charges (Table 30). The opposite effect of Fe and Mg substitution for the MO-SiOH site is not yet understood. Interestingly, the AlOH-SiO site stays the preferred one after modification due to iron substitution. Only the weak preference for the coordination numbers 4 or 5 changes.

For comparison we also calculated uranyl adsorption at various sites of the (110) edge surface of montmorillonite with an octahedral iron substitution below the surface. For this case geometry variations of the adsorption complexes were negligible in comparison to substitution at the surface. Also the changes of the formation energies for each site were calculated to be smaller, at most 8 kJ/mol, than for sites including substituted iron. These results again confirm that uranyl adsorption essentially depends on the type of site.

To summarize, iron substituted sites at smectite edge surfaces may well be favorable sites, but show no characteristic geometry features for discrimination by EXAFS. Thus, further experimental and computational efforts are worthwhile to study this strengthening effect of iron substitutions on actinide adsorption as it is of interest for the choice of

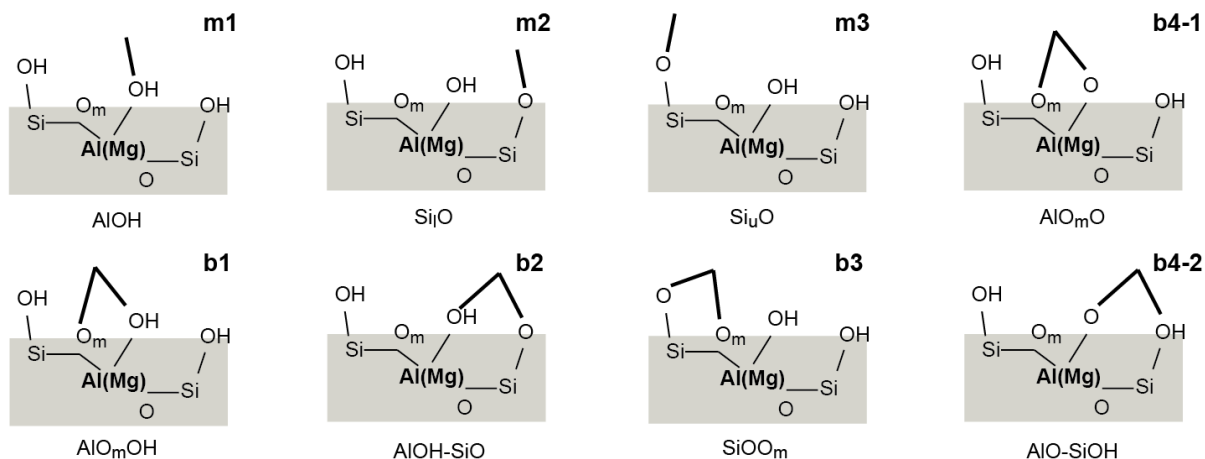


Figure 17. Schematic representation of monodentate (**m**, first row) and bidentate (**b**, second row) adsorption sites studied at the (110) edge surface of montmorillonite.

bentonites to be used in final repositories and relates to effects of waste container corrosion on actinide mobility.

4.2.3 Np(V) adsorption

Besides the experimentally and computationally most commonly studied actinide U(VI), forming the main constituent of radioactive waste, we extended our computational investigations of actinide adsorption also to Np(V) [145], forming the neptunyl ion NpO_2^+ , which is the most common oxidation state of Np under environmental conditions and Np is of interest with respect to safety considerations for final repositories of highly active radioactive waste as its long-lived isotope Np^{237} contributes to the radiotoxicity for long storage times [153]. Various batch experiments on different minerals have been undertaken [9,154-158]. Speciation and structural characterization of adsorbed Np(V) on clay and related minerals is limited to FTIR experiments on gibbsite [159,160] and EXAFS studies on gibbsite [160] and kaolinite [161,162]. Batch experiments showed that Np(V) starts to adsorb at higher pH and adsorbs weaker compared to U(VI) [154], in line with its lower charge. Results of EXAFS studies of Np(V) adsorption on gibbsite and kaolinite were interpreted to show inner sphere adsorption complexes [160,162], although not always Np-Al/Si distances were resolved. There is the common expectation, that adsorption of Np(V), although weaker, is otherwise similar to U(V). In thermodynamic models, adsorption at aluminol and silanol sites was suggested [8,9].

In this project, we carried out the first computational study on Np(V) adsorption on a mineral surface [145]. We choose the montmorillonite (110) edge surface for a mineral model with the permanent layer charge of $-0.25 e$ as an exemplary substrate system, as it allows comparison with our results for uranyl(VI) adsorption (Section 4.2.2), including accurate formation energies, as achieved by the LTPE approach (Section 4.3.1) [57]. Surfaces with surface and subsurface substitution of octahedral Al^{3+} by Mg^{2+} are modeled. In this study we considered again a partially deprotonated surface, which is reliable as the adsorption of Np(V) on montmorillonite starts at pH = 7 [154]. The same five adsorption sites on the (110) surface for bidentate adsorption as for U(VI) have been inspected (Fig. 17). In addition, we also

Table 32. Adsorbed species, coordination numbers (CN) and relative energies E_{rel} (in kJ/mol) for mono- and bidentate adsorption of UO_2^{2+} and NpO_2^+ at various sites on (110) edge surfaces of montmorillonite. For site designations see Fig. 17.

Surface/Site	U(VI)			Np(V)		
	Adsorbate	CN	E_{rel}	Adsorbate	CN	E_{rel}
Unsubst.						
AlOH	m1	UO_2OH^+	4	85	NpO_2OH	4 41
AlO_mOH	b1	UO_2OH^+	5	68	NpO_2^+	4/5 86/98
Si_lO	m2	UO_2OH^+	5	13	NpO_2OH	4/5 0/61
AlOH-SiO	b2	UO_2^{2+}	4/5	0/16	NpO_2^+	4/5 15/24
Si_uO	m3	UO_2OH^+	5	23	NpO_2OH	4 36
SiOO_m	b3	UO_2OH^+	5	27	NpO_2^+	4/5 80/85
AlO_mO	b4-1	UO_2^{2+}	5	38	-	
AlO-SiOH	b4-2	UO_2^{2+}	4/5	73/73	NpO_2^+	4 127
Subst.						
MgOH	m1	UO_2OH^+	4	104	NpO_2OH	4 22
MgO_mOH	b1	UO_2OH^+	4	78	$\text{NpO}_2\text{OH}/\text{NpO}_2^+{}^a$	4/5 71/97
Si_lO	m2	UO_2OH^+	5	21	NpO_2OH	4/5 0/81
MgOH-SiO	b2	UO_2^{2+}	4	0	NpO_2^+	4 26
Si_uO	m3	UO_2OH^+	5	31	$\text{NpO}_2^+/\text{NpO}_2\text{OH}$	4/4 52/60
SiOO_{Mg}	b3	UO_2OH^+	5	35	NpO_2^+	4 59
MgO_mO	b4-1	UO_2^{2+}	4	60	-	
MgO-SiOH	b4-2	UO_2^{2+}	4/5	69/96	NpO_2^+	4 143

^a four-coordinated NpO_2OH and five-coordinated NpO_2^+

investigated monodentate adsorption complexes. Possible sites are formed by AlOH and SiO groups. For the SiO groups, we distinguish upper and lower variants, SiO_u and SiO_l , according to their position on the (110) surface (Fig. 17). Geometry optimizations aiming at monodentate adsorption complexes at AlO sites were not successful. All attempts to achieve such structures resulted in bidentate adsorption complexes at AlO_mOH or AlO-SiOH sites.

The types of Np(V) and U(VI) adsorbates together with their coordination numbers and relative formation energies as determined for various sites at the unsubstituted and the substituted (110) surface of montmorillonite are listed in Table 32. In contrast to U(VI), where we were able to find adsorption complexes at all possible sites, no stable adsorption complex could be optimized for the AlO_mO site for Np(V). Instead, a proton from a neighboring SiOH group is attracted by the AlO group of the site, leading to a bidentate species at an AlO_mOH site [145]. This difference between U(VI) and Np(V) may be explained by the higher positive charge of uranyl(VI), which compensates more effectively the negative charge of the AlO group. As already discussed above, U(VI) frequently adsorbs as uranyl monohydroxide. For monodentate sites only monohydroxide has been obtained as adsorbate. The type of adsorbate determined does not change due to surface substitution (Table 32). Four- and five-coordinated

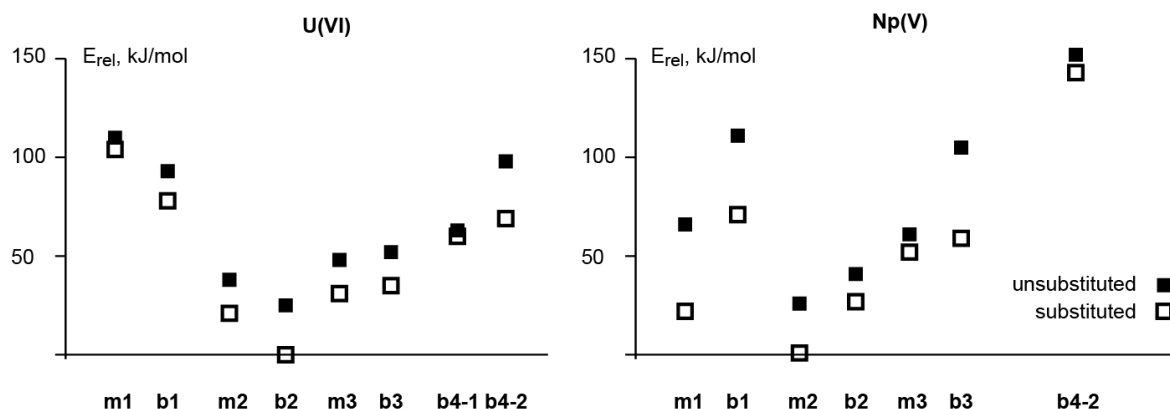


Figure 18. Comparison of relative energies of formation of adsorption complexes of U(VI) and Np(V) on the (110) edge surface of montmorillonite. For the site designations see Fig. 17.

complexes are found, with a tendency to more frequent four-coordinate species on the substituted surface. For Np(V) formation of monohydroxide on the surface is found to be less common than for U(VI), in agreement with the higher hydrolysis constant of Np(V) compared to U(VI) [163]. Due to the lower charge of neptunyl(V) compared to U(VI) and the concomitant weaker binding, a stronger tendency to form four-coordinated surface complexes is expected. For that reason, we optimized initial structures with CN = 4 and 5 for Np(V). Indeed, as shown in Table 32, four-coordinated species are always preferred for adsorbed neptunyl [145].

To facilitate the comparison of mono- and bidentate adsorption complexes, we grouped the adsorption sites according to the surface groups which are deprotonated [145]. In this way one obtains pairs of corresponding mono- and bidentate sites **mx** and **bx** (Table 32), where $x = 1-3$ labels the way of surface deprotonation. Relative formation energies for all adsorption complexes considered are shown in Fig. 18. As earlier shown for uranyl, also neptunyl shows lower energies for substituted than for unsubstituted sites, which is explained by the increased effective charge of the substituted sites (Section 4.2.2, Table 23). For uranyl, monodentate coordination to the surface tends to be less favorable than bidentate coordination for surfaces with and without surface substitution (compare the sites **m1** and **b1** as well as **m2** and **b2**, Fig. 18). The corresponding sites **m3** and **b3** are rather close in energy with **m3** being only 4 kJ/mol lower in energy than **b3**. For neptunyl the opposite trend is calculated. For all deprotonation variants, monodentate coordination is preferred (Fig. 18). Interestingly, the most favorable site for U(VI), (Al,Mg)OH-SiO, is also the preferred one for Np(V), but neptunyl coordinates only to its SiO group (SiO₁ site, **m2**). An overall view on relative energies (Fig. 18) shows that more preferred complexes with low relative energies, close to the most preferred one, might be mono- or bidentate species. Thus, for U(VI) as well as Np(VI) both forms of surface coordination might occur in nature.

Table 33. Structural parameters (in pm)^a and relative energies E_{rel} (in kJ/mol) of neptunyl(V) monodentate and bidentate adsorption complexes for various sites at the unsubstituted and substituted (110) edge surfaces of montmorillonite. For comparison computational data for the solvated neptunyl ion modeled as $\text{NpO}_2^+(\text{H}_2\text{O})_6$ with CN = 4 and 5 and experimental data with CN in parentheses are given. For site designations see Fig. 17.

Site	CN	Np-O _t	Np-O _s ^b		Np-O _H	Np-O _w	Np-O _{eq}	Np-Al	Np-Si	E_{rel}
NpO ₂ ⁺	4	185					244			
NpO ₂ ⁺	5	185					253			
Unsubst.										
AlOH	m1	4	188	232	231	247	239	401		41
AlO _m OH	b1	4	184	246 238		242	242	347	351	86
Si _u O	m2	4	187	220	235	247	237		377	36
SiOO _m	b2	4	187	232 258		241	243	420	306	80
Si _l O	m3	4	186	230	236	246	240		366	0
AlOH-SiO	b3	4	184	240 231		246	241	392	359	15
		5	185	234 231		265	252	395	362	24
AlO-SiOH	b4-2	4	188	203 252		256	242	368	385	127
Subst.										
								Np-Mg		
MgOH	m1	4	189	228	230	249	239			22
MgO _m OH	b1	4	187	239 233	235	237	236	340	373	71
Si _u O	m2	4	186	218		248	241		379	52
SiOO _{Mg}	b2	4	185	232 245		250	244		300	59
Si _l O	m3	4	186	233	221	256	242		366	0
MgOH-SiO	b3	4	185	229 232		247	239		366	26
MgO-SiOH	b4-2	4	190	197 250		251	237	370	385	143
Exp.										
	Ref.	pH								
NpO ₂ ⁺	161		182(2)				249(3.6)			
kaolinite	162	8	185(2)				245(4)			
	162	9	186(2)				250(4)			
	162	10	187(2)				247(4)			

^a Average terminal neptunyl bond length Np-O_t, bond lengths Np-O_s to surface oxygen centers, Np-O_H bond length to OH ligands, bond length Np-O_w to aqua ligands, average equatorial Np-O bond lengths Np-O_{eq}, Np-Al/Mg and Np-Si distances to the nearest surface Al/Mg and Si centers. ^b The order of Np-O_s bonds follows the site label.

Structural parameters of monodentate adsorption complexes turned out to be rather similar to bidentate ones for U(VI) [145]. For the three monodentate sites of the (110) surface of montmorillonite we calculated U-O_t bond lengths of 183-185 pm and U-O_{eq} distances of 241-247 pm for CN = 5 and of 233-234 pm for CN = 4 [145]. These results are well comparable to the data for bidentate complexes on the same surface, which are U-O_t = 182-185 pm and U-O_{eq} = 242-247 pm for CN = 5 and 230-234 pm for CN = 4, as well as to average values over various smectite models (Table 26). Thus, the observation that U-O_{eq} essentially depends on the coordination number (see above and Section 4.1.2) is also valid for monodentate adsorption complexes. Also individual U-O bonds to surface oxygen centers, to OH ligands as well as to aqua ligands are similar for mono- and bidentate U(VI) adsorption complexes [145]. The only parameter which allows a discrimination of mono- and bidentate

coordination of U(VI) to the surface are the U-Al/Si distances. These were calculated for monodentate complexes to about 375-380 pm for U-Si and to more than 400 pm for U-Al [145], exceeding the shorter ones of these distances for bidentate complexes. As these distances are beyond U-Al/Si distances of up to 343 pm as measured until now for montmorillonite [150] (Table 26), one may conclude that monodentate adsorption complexes do not occur. On the other hand, monodentate surface species may well be present, as their energies are only slightly above the ones of bidentate species, especially when substituted sites are taken into account (Fig. 18) and their U-Al/Si distance are beyond the typical range of distances easily resolvable by EXAFS.

Due to its lower charge, NpO_2^+ shows longer bonds than UO_2^{2+} . For the aqua complex neptunyl bonds of 180-185 pm and Np-O_{eq} bonds of 244-252 pm have been measured [161], which are by roughly 5 pm longer than for uranyl. Correspondingly, also adsorbed NpO_2^+ exhibits longer geometry parameters than UO_2^{2+} . Our calculated results show neptunyl bonds of 184-190 pm, compared to 182-185 pm for uranyl (Table 33). The averaged An-O_{eq} bond lengths amount to 236-244 pm for adsorbed neptunyl for the preferred CN of 4 (Table 33) and to 230-235 pm for corresponding uranyl species (Table 26). As for U(VI), An-O_{eq} is determined mainly by the CN. For the less stable species with CN = 5, Np-O_{eq} for adsorbed Np(V) complexes measures 252-253 pm (Table 33 [145]). Also the Np-O_{H} bonds for adsorbed neptunyl monohydroxide species tend to be longer than for uranyl. They are calculated at 221-236 pm versus 216-232 pm for U(VI) (Tables 33 and 26). Np-Al/Si distances, which are no direct bonds and more flexible, are found in the same range as for U(VI). In all other aspects, structural features and trends of the two adsorbed actinyls compared are similar. Np-O_{s} bond lengths also correlate with the effective charge of the surface oxygen centers involved, but that correlation is weaker than for uranyl [145], as expected for longer and thus weaker and more flexible bonds. The mainly ionic interaction of neptunyl with the surface is shown as for uranyl by the effect of site substitution, exemplified here by the substitution of Al^{3+} by Mg^{2+} , leading to shorter bonds to the surface due to the higher effective charges of the O_{s} centers (Table 33) [145].

A comparison of various EXAFS results for uranyl and neptunyl adsorption on clay and related minerals shows that pertinent structure parameters like the length of the actinyl bonds or the average equatorial An-O distance are similar for the same actinide ion adsorbed on various minerals [145]. This observation, which corresponds to our finding that adsorbed species and their structures essentially depend on the nature of the adsorption site (Section 4.2.2), encourages us to compare tentatively calculated geometry parameters for Np(V) on montmorillonite to experimental results for kaolinite (Table 33) [162], as no EXAFS measurements for montmorillonite are available. Measured neptunyl(V) bonds of 185-187 pm [162] fit well to our calculated results of 184-188 pm, when ignoring coordination to less probable (Al,Mg)O surface groups (Table 33). The EXAFS results for Np-O_{eq} of 245-250 pm [162] are longer than the calculated values for four-coordinated species of 236-244 pm and

shorter than the corresponding results for five-coordinated species of 252-253 pm [145]. The measured Np-O_{eq} values are shorter than the reference value of 250 pm [162] measured by the same group for the neptunyl(V) aqua ion. This trend we observe also in our calculated results, where we obtain Np-O_{eq} = 244 pm for the four-coordinated aqua ion and mainly shorter Np-O_{eq} distances of 236-244 pm for the adsorbed complexes (Table 33) [145]. Although Np-Al/Si/Mg distances are unfortunately missing in the experimental results, the close correspondence of calculated and measured geometry parameters and trends supports our finding of predominately monodentate and four-coordinated Np(V) adsorbed species on edge surfaces of montmorillonite. Our more detailed studies for U(VI) adsorption on smectite edge surfaces allow the tentative hypothesis that also our results for Np(V) are valid in general for clay mineral edge surfaces. Thus, these results are a first step toward an atomistic speciation model for Np(V) adsorption on clay mineral surfaces, which might be helpful for the construction of thermodynamic models.

4.2.4 Adsorption of salt cations

Studies of actinide adsorption most commonly have been carried out at low ionic strength. However, pore waters of potential clay host rock formations for final repositories, e.g. in northern Germany, may show rather high salt concentration of up to about 5 M [16]. Thus, the influence of elevated ionic strength, which might lead to a competition for adsorption sites of typical salt cations like Na⁺, Ca²⁺ and Mg²⁺ and actinide ions has to be studied. Experimental work of the project partners showed that adsorption of Eu(III), which serves as an analogue for actinides in oxidation state III, is suppressed at low pH by high concentrations of Ca²⁺ and Mg²⁺ [164], where the ion exchange sorption mechanism prevails. At a pH > 5 the sorption curves of Eu(III) are only slightly affected. For U(VI) and Np(V), only marginal effects of the presence of elevated concentrations of alkaline earth cations have been measured [164]. The concentration of Na⁺ in pore water solutions seems to have in general no effect on actinide adsorption [165]. To complement the experimental investigations of the project partners, we studied the adsorption of Ca²⁺ and Mg²⁺ for the example of the (110) edge surface of montmorillonite by means of the LTPE approach [57], to determine favorable adsorption sites, preferred species, and to estimate the adsorption strength in comparison to our results for actinide ions (see above).

As in our detailed study of adsorption of U(VI) (Section 4.2.2) and Np(V) (Section 4.2.3) on the (110) edge surface of montmorillonite we considered mono- and bidentate adsorption sites for Ca²⁺ and Mg²⁺. We choose the initial coordination number of both cations to be six, which is the common coordination number in solution [166]. Table 34 lists the species, as obtained by the LTPE approach, together with their coordination numbers and relative energies of adsorption. Attempts to stabilize adsorption complexes on the sites AlO_mO and AlO-SiOH were not successful. In both cases the AlO groups involved were protonated by protons stemming from neighboring silanol groups, leading to adsorption complexes at AlO_mOH and either AlOH-SiOH or AlOH-SiO sites. Thus, no stable adsorption

Table 34. Species and relative formation energies (in kJ/mol) of Ca^{2+} and Mg^{2+} adsorbed on various sites of the (110) edge surface of montmorillonite.

Surface/Site	Adsorbate	CN	E_{rel}	Adsorbate	CN	E_{rel}
unsubstituted						
AlO_mOH	Ca^{2+}	6/7	0/19	Mg^{2+}	6	2
AlOH	CaOH^+	6	46	Mg^{2+}	6	52
SiOO_m	CaOH^+	6	102	- ^a	-	-
Si_iO	- ^b	-	-	Mg^{2+}	5	0
Si_uO	Ca^{2+}	6	39	Mg^{2+}	6	58
AlOH-SiO	Ca^{2+}	6	17	Mg^{2+}	5	33
AlOH-SiOH	-	-	-	Mg^{2+}	6	19
substituted						
MgO_mOH	Ca^{2+}	6	0	Mg^{2+}	6	19
MgOH	Ca^{2+}	6	28	Mg^{2+}	6	57
SiOO_m	CaOH^+	5	62	MgOH^+	5	89
Si_iO	- ^b	-	-	Mg^{2+}	6	0
Si_uO	Ca^{2+}	6	35	Mg^{2+}	6	42
MgOH-SiO	Ca^{2+}	6	3	Mg^{2+}	5	44
MgOH-SiOH	Ca^{2+}	6	34	Mg^{2+}	6	58

^a converged to monodentate adsorption on Si_uO site; ^b converged to bidentate adsorption at AlOH-SiO site.

complexes at sites including AlO groups, which have a high deprotonation energy (see above), were found. This phenomenon, also observed to a lesser extent for Np(V) (see Section 4.2.3) may be rationalized by the effective charges of the metal centers of the adsorbates, which decrease from UO_2^{2+} over NpO_2^{2+} to Mg^{2+} and Ca^{2+} [90]. Due to its high formal charge of $-3/2$ the AlO group is prone to protonation by a proton from a neighboring group. Coordination of a cationic metal center with increasing charge compensates the charge of the AlO group more efficiently and thus suppresses its protonation. Thus, adsorption complexes coordinating to AlO groups are most commonly found for U(VI) (Table 32) and not at all for the alkaline earth ions. Other cases of seemingly unstable sites are the SiOO_m site for Mg^{2+} at the unsubstituted surface (Table 34). Optimization of such a starting geometry lead to a monodentate adsorbed species at the Si_uO group. For Ca^{2+} we found no monodentate adsorption complexes at the Si_iO site and obtained instead a bidentate complex at the AlOH-SO site (Table 34). As Table 34 shows, in most cases we found Ca^{2+} and Mg^{2+} with $\text{CN} = 6$ as adsorbate. Exceptions are the AlOH and SiOO_m sites for Ca^{2+} at the unsubstituted surface and the SiOO_m site at the substituted surface for Ca^{2+} and Mg^{2+} . For these sites monohydroxides were calculated as adsorbates. This finding is astonishing, as both ions only weakly hydrolyze compared to U(VI) or Np(V) . On the one hand, hydroxide species are determined less frequently than for the actinides, on the other, they do not appear for the same sites. Thus, this aspect needs further investigations. Changes of the coordination number of the adsorption complex from 6 to 5 are more common for Mg^{2+} than for Ca^{2+} , in agreement with the larger radius of the latter ion. As for U(VI) , $(\text{Al,Mg})\text{OH-SiO}$ is a site prone to lowering of the CN of Mg^{2+} due to steric reasons (Table 34). The larger adsorbate Ca^{2+} in general shows longer

bonds to the surface, which implies smaller angles $O_s-M^{2+}-O_s$ compared to Mg^{2+} , and thus a weaker steric demand of the surface coordination compared to Mg^{2+} . This explains why lowering of the CN is more frequently observed for Mg^{2+} (Table 34).

Relative energies of the adsorption complexes of Ca^{2+} and Mg^{2+} (Table 34) show, that these ions prefer not the same sites as U(VI) and Np(VI) (Table 32). For Ca^{2+} the most favorable site is $(Al,Mg)O_mOH$ and only the next most favorable is $(Al,Mg)OH-SiO$, as for U(VI). For Mg^{2+} AlO_mOH and SiO_1 sites are preferred, where the latter one also binds Np(V) favorably. Thus, although the most stable sites differ from the ones preferred by the actinides, the set of more favorable sites for all these cationic adsorbates is similar. This suggests that there is at least no strong competition for one and the same type of site for actinide and alkaline earth cations. Comparison of absolute complex formation energies for Ca^{2+} , Mg^{2+} , and UO_2^{2+} shows that when the same site is occupied Ca^{2+} binds weaker than Mg^{2+} , as expected due to its larger radius. UO_2^{2+} binds for all but a single site stronger than the alkaline earth ions, which is in line with the higher effective charge of the U center, which is comparable to An(III) [90]. Both these findings support the weak competition between alkaline earth cations and actinides observed experimentally (see above). Unfortunately a reliable comparison of formation energies to Np(V) is hampered by its different charge compared to the other ions, which involves a slightly modified substrate model (Section 4.2.3).

4.3 Method development

Method development and evaluation in this project concentrated on models for surface solvation by an aqueous medium, as a proper treatment of surface solvation is a major challenge in quantum chemical calculations of adsorption at mineral surfaces. With the low temperature partial equilibration computational protocol [57] (Section 4.3.1) we were able to determine efficiently reliable surface complex formation energies with a model including explicit water molecules as solvent. A recently developed surface polarizable continuum model [37] as a complementary approach was evaluated for its performance (Section 4.3.2)..

4.3.1 Low temperature partial equilibration

The calculation of comparable energies for an adsorbate at various sites at a mineral-water interface by a model including more than just a few explicit water molecules of the solution is challenging, as such systems include a large number of soft degrees of freedom like the orientation of solvent water molecules and their hydrogen bond network. Attempts to optimize the geometry of such a system faces the problem of a large number of shallow minima on the potential energy surface. Due to an arbitrary structure of the water overlayer on the surface, fluctuating energies for adsorbates at various sites are typically obtained, as discussed in Section 4.2.2. A fully dynamic treatment of solvated mineral surfaces represents a proper solution to this problem, albeit at the price of a rather high computational effort which is needed to achieve simulation times allowing a reliable statistical evaluation of the results. In

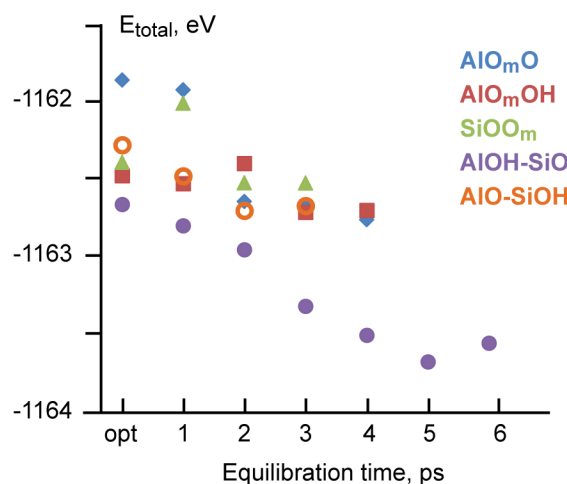


Figure 19. Convergence of total energies during the LTPE procedure as a function of equilibration time for the example of adsorption complexes of uranyl(VI) on various sites of the (110) edge surface of pyrophyllite. For comparison the total energy resulting from conventional optimization (opt.) is also given.

addition, only the most stable structures of adsorbates or energetically low lying metastable species are accessible in this way. As a compromise, we developed an efficient approximate computational scheme applying dynamic simulations at low temperature, with the goal to equilibrate soft degrees of freedom only [57]. We applied this scheme to various problems of actinide adsorption at clay mineral surfaces (Sections 4.2.2-4.2.4).

We start the partial equilibration of an adsorption system from an optimized structure and equilibrated it at 200 K for 3-6 ps applying the NVE microcanonical ensemble. Test calculations showed that the temperature of 200 K is low enough that even metastable adsorption complexes are not disturbed, and high enough to allow the rearrangement of water molecules of the solvation layer. A time step of 0.2 fs is chosen and the temperature is adjusted to 200 K every 50 steps. The convergence of the equilibration is controlled every ps by carrying out an optimization of the current structure. The equilibration is considered to be converged if the total energies of two subsequent test optimizations deviate by less than 10 kJ/mol. Then the system is cooled down to 0 K during 1 ps by linearly decreasing the temperature every 50 steps. Finally a conventional geometry optimization is done as the last step of the procedure.

An example for the performance of the LTPE approach is shown in Fig. 19 for uranyl adsorbed at various sites of the (110) edge surface of pyrophyllite. As to be expected, the total energy of the systems drops with increasing equilibration time due to the relaxation of the solvation layer. In most cases the convergence criterion is reached already after 3-4 ps. Adsorption at the AlOH-SiO site forms an exception as the initially five-coordinated adsorbate changes to CN = 4 after 4 ps. Thus, a little longer equilibration time of 6 ps is needed. An analysis of the structural changes during equilibration based on the test

Table 35. Comparison of structural parameters (see Table 26, in pm) and formation energies (in kJ/mol) as calculated with LTPE and PCM approaches for for uranyl(VI) adsorbed at various sites of the unsubstituted (110) edge surface of montmorillonite.

Site	Meth.	CN	U-O _t	U-O _s ^a		U-O _H	U-O _w	U-O _{eq}	U-Al	U-Si	E _{form}
AlO _m O	LTPE	5	186	249	203		260	246	332		81
	PCM	5	183	251	208		255	245	333		69
AlO _m OH	LTPE	5	182	249	235	218	264	246	351		111
	PCM	5	180	245	232		247	243	347		134
	PCM	5	182	262	236	215	255	244	355		60
SiOO _m	LTPE	5	185	218	261	232	253	243		307	70
	PCM	5	181	238	241		259	253	354	316	90
	PCM	5	182	226	260	225	255	244		308	42
AlOH-SiO	LTPE	4	183	232	216		240	232		356	43
	PCM	4	183	228	217		243	233		354	33
	LTPE	5	183	232	216		257	243		360	59
	PCM	5	183	231	217		256	243		356	50
AlO-SiOH	LTPE	4	187	197	250		247	235	379	384	116
	PCM	4	185	199	247		247	235	379	374	100
	LTPE	5	186	200	256		258	246	381	383	116
	PCM	5	185	200	261		255	245	383	390	106

^a The order of U-O_s bonds follows the site designation.

optimizations of intermediate structures after each ps showed that they decreased to less than 1 pm already after 2-3 ps [57]. Overall, these validation calculations demonstrate the efficiency of the approach compared to a fully dynamic treatment demanding typically simulation times of 10-20 ps at least.

4.3.2 Surface solvation by PCM

As an alternative to solvation modeling by explicit water molecules a PCM model for periodic surface models has been recently developed [37]. While the explicit approach, as used mainly in this project, covers essentially short range solvation effects only, like the coordination of water molecules and the formation of hydrogen bonds, both including some charge transfer, the PCM approach provides long range electrostatic screening by the solvent exclusively. Thus, complementary effects of solvation are covered by these two methods of solvation modeling.

To evaluate the performance of the PCM method we compared structures and energies of uranyl(VI) adsorbed on the (110) edge surface of montmorillonite as determined by the LTPE approach, using a water layer to model solvation, with the PCM method applied to a surface model without explicit water molecules but including the first solvation shell of uranyl. Thus complementary approximate solvation models yielding short or long range solvation effects, respectively, are compared. As starting geometries for structure optimizations with the PCM method the results of the LTPE calculations (Section 4.3.1) have been used.

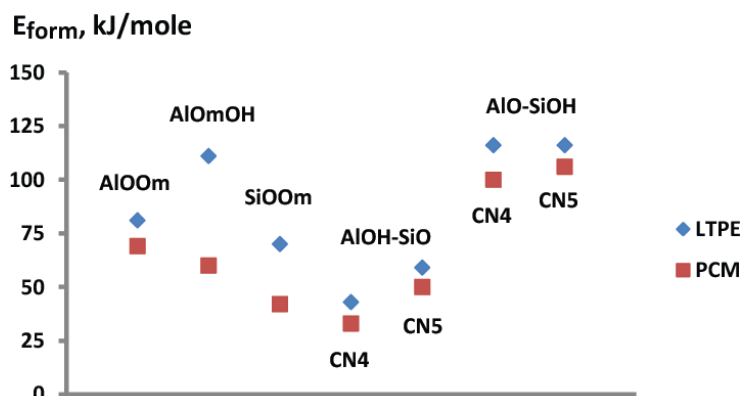


Figure 20. Comparison of formation energies as determined by PCM and LTPE calculations for uranyl(VI) adsorption at various sites of the unsubstituted (110) surface of montmorillonite.

The results of geometry optimizations with the PCM model for various adsorption complexes of uranyl(VI) on the (110) edge surface of montmorillonite together with the corresponding LTPE results are collected in Table 35. Both methods yield the same adsorbed species, uranyl or uranyl monohydroxide, with coordination numbers 4 or 5, for all sites inspected. Also the geometric characteristics of the adsorption complexes as determined by LTPE or PCM are the same. The uranyl bond length $U-O_t$ tends to be shorter, by up to 3 pm, in the PCM calculations as hydrogen bonds between uranyl oxygens and solvent waters are missing in the model. Also $U-O_H$ bonds of uranyl monohydroxide adsorbates are contracted, by up to 7 pm, in the PCM results compared to LTPE due to missing hydrogen bonds to the OH ligands. $U-O_s$ bond length to the surface are short for high empirical charges of the corresponding O_s center and increase with decreasing effective O_s charge (Table 35). Deviations between both methods for $U-O_s$ exceeding a few pm are observed for UO_2OH^+ adsorbates and sites with a strongly contracted uranyl bond (AlO_mO) as a reaction on the changes of the uranyl and $U-O_H$ bond lengths. Concomitantly also average $U-O_w$ bond lengths change stronger for these cases. $U-O_{eq}$ agrees for both methods up to 2 pm, as this quantity is essentially determined by the coordination number (see above). Also $U-Al/Si$ distances are similar for PCM and LTPE calculations (Table 35). Similar trends of differences between the geometries of adsorption complexes between both solvation methods have been calculated for the (110) surface of montmorillonite with a Mg^{2+} substitution on the surface.

Formation energies of the adsorption complexes (Table 35) as determined by PCM and LTPE calculations are compared in Fig. 20, which shows that these energies are always lower for the PCM approach. For most of the complexes the differences of the formation energies between both methods are smaller than 20 kJ/mol and show the same trend for various adsorption sites. Larger differences of up to about 50 kJ/mol are obtained for uranyl monohydroxide as adsorbate (Fig. 20). This stronger stabilization of uranyl monohydroxide as

adsorbate by the PCM approach may be attributed to missing strong hydrogen bonds to the OH ligand in this model and the subsequent stabilization of the ionic U-O_H bond (Table 35). The same effect has been observed on the surface substituted (110) surface of montmorillonite, but a comparable stabilization of UO₂²⁺ on the MgO_mO site of that surface deviates from the general trend.

Overall, these test calculations show that the PCM method yields qualitatively similar results for uranyl adsorption on a clay mineral surface compared to a model with an explicit solvation layer and the application of partial equilibration by means of the LTPE approach. Deviating geometry parameters and formation energies for uranyl monohydroxide as adsorbate show the limits of this model for cases when short range solvation effects are important. Thus PCM is a valuable and efficient method to treat surface solvation, but a carefully constructed model of the surface, including the most important water molecules of the solvent explicitly, seems to be necessary to achieve accurate results. Circumventing the limitations of the PCM approach in this way, this efficient method will be very useful for future quantum chemical studies of actinide adsorption.

5 Summary

Quantum chemical modeling of actinide complexes in solution and adsorbed on clay mineral surfaces, motivated by safety considerations of deep geological repositories for highly radioactive waste, has been carried out in this project. Complexation of actinides in aqueous solution, which contributes to the solubility, is investigated to provide insight to speciation, geometry, and thermodynamics of various species present in pore and ground waters. Adsorption of actinides at clay mineral surfaces is studied as an important retardation effect against transport of these elements in the environment.

Complexation of actinides by small carboxylic acids, which are components of soluble clay organic matter, have been investigated for U(VI), Np(V) and Am(III). Preferred coordination modes and structural parameters of formate, acetate, and lactate complexes have been determined and are in most cases in agreement with experimental findings. While in thermodynamic models carboxylate complexes are commonly regarded as single effective species, our calculated complexation energies in many cases suggest an equilibrium between various coordination modes. Thus, in some cases actinide carboxylate complexes should be regarded as a set of species with varying thermodynamic properties, to achieve a more realistic and transferable thermodynamic modeling. Calculated absolute complexation energies are not very accurate, but show reliable trends which allow comparison with the corresponding experimentally determined complexation energies for various ligands and actinide oxidation states. These results contribute to the check of accuracy of available thermodynamic data sets and help to identify uncertainties. Our calculations show that besides pure carboxylate complexes also ternary chloro carboxylate complexes may exist in salt solutions.

The complexation of actinides by borate has been inspected as borate is found in small amounts in salt formations considered as potential host rocks for final repositories. It is also introduced into geological repositories as part of the nuclear inventory, e.g. by heat resistant vitrified waste. Mainly the complexation of U(VI) and Am(III) by monoborate, relevant at low borate concentrations, has been modeled. Comparison with carboxylate complexes shows that borate forms complexes of comparable strength. Interestingly, also complexes with the borate Brønstedt anion seem to be possible, as well as ternary hydroxo borate complexes. Coordination modes and structures of the complexes have been characterized, which will be helpful for a spectroscopic identification of these species. Borate esters, suggested as model ligands by project partners but also of interest on their own, showed lower complexation energies as monoborate. Thus, although at higher borate concentrations precipitation prevails, borate complexes should be considered to exist at lower borate concentrations.

Adsorption of actinides on dioctahedral 2:1 phyllosilicates has been studied for the reactive edge surfaces of pyrophyllite, montmorillonite and beidellite type model minerals. These models represent compositions and structures of typical smectite clay minerals. Our models included generic surface substitutions as well as iron substitutions. As a main result we find that speciation and structure of adsorption complexes of U(VI) and Np(V) essentially depend on the type of the adsorption site and are rather independent of the mineral model inspected. The interaction of the ionic adsorbed complexes increases with the charge of the site and the mineral, as expected. Iron substitutions at the edge surfaces of the minerals inspected tend to stabilize adsorption complexes. While for U(VI) CN = 5 is prevailing, Np(V) tends to a lower CN of 4 due to its lower charge. Besides adsorbed actinyls also actinyl monohydroxides have been obtained as adsorbed species. In contrast to current thermodynamic models, modeling adsorption by the assumption of strong and weak sites, our results suggest a variety of possible adsorption sites on the edge surfaces of clay mineral, represented better by a continuum of interaction strengths. As we did not consider absorption into the mineral bulk or rare defect sites, our model calculations could be also interpreted to represent only weak sites. Preferred sites at relevant pH conditions are formed by AlOH and SiO groups. Comparing the same type of site, U(VI) prefers bidentate and Np(V) monodentate coordination to the surface. Nevertheless, energy considerations show that for both actinides mono- and bidentate coordination modes have to be taken into account. Comparison of structural parameters to EXAFS results sheds light on the difficulty to identify adsorption complexes. The commonly measured average equatorial An-O bond lengths of actinyl ions is shown to be essentially determined by the coordination number of the actinyl, as shown already earlier for actinide complexes. An-Al/Si/Fe distances show a wide variation, depending on the type of adsorption site. Comparison of these distances to experiment supports our suggestions of more probable adsorption sites based on energy and surface deprotonation considerations. Thus, our results provide a more detailed insight into actinide adsorption at clay mineral surfaces than current spectroscopic experiments, which is useful for

a mechanistic understanding and helpful for the construction of more realistic thermodynamic models. The type of available adsorption sites and the system charge (of the mineral and the site) have been identified as more important factors determining actinide adsorption, which is rather independent of the specific clay mineral and its composition. These results suggest that a generic thermodynamic model for various 2:1 clay minerals, parameterized by the layer charge and the iron content, could be a reliable approach to describe actinide adsorption for this wide class of minerals.

6 Publikations resulting from this project

1. G. Beridze, A Relativistic Density Functional Study on Americium Aqua- and Acetate Complexes, Master Thesis, TU München, 2011.
 2. A. Kremleva, B. Martorell, S. Krüger, N. Rösch, Uranyl Adsorption on Solvated Edge Surfaces of Pyrophyllite: A DFT Model Study, *Phys. Chem. Chem. Phys.* 14 (2012) 5815.
 3. A. Kremleva, Y. Zhang, A. M. Shor, S. Krüger, C. Joseph, B. Raditzky, K. Schmeide, S. Sachs, G. Bernhard, N. Rösch, Uranyl(VI) Complexation by Sulfonate Ligands: A Relativistic Density Functional and Time-Resolved Laser-Induced Fluorescence Spectroscopy Study, *Eur. J. Inorg. Chem.* 22 (2012) 3636.
 4. A. Kremleva, S. Krüger, N. Rösch, Assigning EXAFS Results for Uranyl Adsorption on Minerals via Formal Charges of Bonding Oxygen Centers, *Surf. Sci.* 615 (2013) 21.
 5. A. Kremleva, S. Krüger, N. Rösch, Uranyl Adsorption on Solvated Edge Surfaces of 2:1 Smectites. A Density Functional Study. *Phys. Chem. Chem. Phys.* 17 (2015) 13757.
 6. A. Kremleva, S. Krüger, N. Rösch, Toward a Reliable Energetics of Adsorption at Solvated Mineral Surfaces: A Computational Study of Uranyl(VI) on 2:1 Clay Minerals. *J. Phys. Chem. C* 120 (2016) 324.
 7. A. Kremleva, S. Krüger, N. Rösch, Uranyl Adsorption at Clay Minerals, in *High Performance Computing in Science and Engineering 2016*, S. Wagner, A. Bode, H. Brüche, M. Brehm (Ed.), Bayerische Akademie der Wissenschaften, 2016, p. 177.
 8. A. Kremleva, S. Krüger, Comparative Computational Study of Np(V) and U(VI) Adsorption on the (110) Edge Surface of Montmorillonite, *Clay Clay Min.* 2016 accepted.
- Further publications on results of this project and follow-up studies are in preparation.

References

- [1] M. Altmaier, X. Gaona, T. Fanghänel, *Chem. Rev.* 113 (2013) 901.
- [2] R. Guillaumont, T. Fanghänel, V. Neck, J. Fuger, D. A Palmer, I. Grenthe, M. H. Rand, Update on the Chemical Thermodynamics of Uranium, Neptunium, Plutonium, Americium and Technetium, Elsevier: Amsterdam, 2003, Vol. 5.
- [3] W. Hummel, G. Anderegg, L. Rao, I. Puigdomènech, O. Tochiyama, Chemical Thermodynamics of Compounds and Complexes of U, Np, Pu, Am, Tc, Se, Ni and Zr with Selected Organic Ligands, Elsevier: Amsterdam, 2005, Vol. 9.
- [4] L. R. Morss, N. M. Edelstein, J. Fuger (Eds.), Actinide and Transactinide Elements, 3. ed., Springer: Dordrecht, 2006.
- [5] E. A. Jenne (Ed.), Adsorption of Metals by Geomedia: Variables, Mechanisms and Model Applications, Academic Press: United Kingdom, 1998.
- [6] M. Barnett, D. Kent (Eds.), Adsorption of Metals by Geomedia II: Variables, Mechanisms, and Model Applications, Elsevier: Amsterdam, 2008.
- [7] H. Geckeis, J. Lützenkirchen, R. Polly, T. Rabung, M. Schmidt, *Chem. Rev.* 113 (2013) 1016.
- [8] M. H. Bradbury, B. Baeyens, *Geochim. Cosmochim. Acta* 69 (2005) 4187.
- [9] M. H. Bradbury, B. Baeyens, *Geochim. Cosmochim. Acta* 69 (2005) 875.
- [10] M. Marques Fernandes, B. Baeyens, R. Dähn, A. C. Scheinost, M. H. Bradbury, *Geochim. Cosmochim. Acta* 93 (2012) 262.
- [11] Z. Szabo, T. Toraiishi, V. Vallet, I. Grenthe, *Coord. Chem. Rev.* 250 (2006) 784.
- [12] H. Moll, A. Rossberg, R. Steudtner, B. Drobot, K. Müller, S. Tsushima, *Inorg. Chem.* 53 (2014) 1585.
- [13] A. Kremleva, Y. Zhang, A. M. Shor, S. Krüger, C. Joseph, B. Raditzky, K. Schmeide, S. Sachs, G. Bernhard, N. Rösch, *Eur. J. Inorg. Chem.* 22 (2012) 3636.
- [14] A. Courdouan, I. Christl, S. Meylan, P. Wersin, R. Kretzschmar, *Appl. Geochem.* 22 (2007) 1537.
- [15] A. Courdouan, I. Christl, S. Meylan, P. Wersin, R. Kretzschmar, *Appl. Geochem.* 22 (2007) 2926.
- [16] W. Brewitz, Zusammenfassender Zwischenbericht, GSF T 114, 1980.
- [17] D. R. Turner, M. Whitfield, A. G. Dickson, *Geochim. Cosmochim. Acta* 45 (1981) 855.
- [18] B. Grambow, *Elements* 2 (2006) 357.
- [19] M. Borkowski, M. Richmann, D. T. Reed, Y. Xiong, *Radiochim. Acta* 98 (2010) 577.
- [20] J.-F. Luccini, M. Borkowski, M. K. Richmann, D. T. Reed, *Radiochim. Acta* 101 (2013) 391
- [21] S. Wang, E. V. Alekseev, W. Depmeier, T. E. Albrecht-Schmitt, *Chem. Commun.* 47 (2011) 10874.
- [22] H. Geckeis, T. Rabung, *J. Cont. Hydrol.* 102 (2008) 187.
- [23] K. Choi, J. W. Park, *Geoscience J.* 9 (2005) 53.
- [24] P. Benes, K. Kratzer, S. Vlckova, E. Sebestova, *Radiochim. Acta* 82 (1998) 367.
- [25] A. Krepelova, S. Sachs, G. Bernhard, *Radiochim. Acta* 94 (2006) 825.
- [26] R. Kautenburger, H. P. Beck, *ChemSusChem* 1 (2008) 295.
- [27] C. Joseph, K. Schmeide, S. Sachs, V. Brendler, G. Geipel, G. Bernhard, *Chem. Geol.* 284 (2011) 240.
- [28] M. H. Lee, E. C. Jung, K. Song, Y. H. Han, H. S. Shin, *J. Radioanal. Nuc. Chem.* 287 (2011) 639.
- [29] R. N. Collins, T. Saito, N. Aoyagi, T. E. Payne, T. Kimura, T. D. Waite, *J. Environ. Qual.* 40 (2011) 731.
- [30] M. A. Denecke, *Coord. Chem. Rev.* 250 (2006) 730.
- [31] S. S. Lee, P. Fenter, C. Park, N. C. Sturchio, K. L. Nagy, *Langmuir* 26 (2010) 16647.
- [32] P. Fenter, S. S. Lee, C. Park, L. Soderholm, R. E. Wilson, O. Schwindt, *Geochim. Cosmochim. Acta* 74 (2010) 6984.
- [33] S. V. Churakov, *J. Phys. Chem. B* 110 (2006) 4135.
- [34] A. Kremleva, S. Krüger, N. Rösch, *Radiochim. Acta* 98 (2010) 635.
- [35] F. Schlosser, S. Krüger, N. Rösch, *Inorg. Chem.* 45 (2006) 1480.
- [36] C. Lucks, A. Rossberg, S. Tsushima, H. Foerstendorf, A. Scheinost, G. Bernhard, *Inorg. Chem.* 51 (2012) 12288.
- [37] K. Mathew, R. Sundararaman, K. Letchworth-Weaver, T. Arias, R. Hennig, *J. Chem. Phys.*, 140 (2014) 084106.
- [38] N. Rösch, S. Krüger, M. Mayer, V. A. Nasluzov, The Douglas-Kroll-Hess Approach to Relativistic Density Functional Theory: Methodological Aspects and Applications to Metal Complexes and Clusters, in: Recent Developments and Applications of Modern Density Functional Theory, J. M. Seminario (Ed.), Theoretical and Computational Chemistry Series, Vol. 4, Elsevier: Amsterdam, 1996, p. 497.
- [39] N. Rösch, A. V. Matveev, V. A. Nasluzov, K. M. Neyman, L. Moskaleva, S. Krüger, Quantum Chemistry with the Douglas-Kroll-Hess Approach to Relativistic Density Functional Theory: Efficient Methods for Molecules and Materials, in: Relativistic Electronic Structure Theory-Applications, P.

- Schwerdtfeger (Ed.) *Theoretical and Computational Chemistry Series*, Vol. 14, Elsevier: Amsterdam, 2004, p. 656.
- [40] T. Belling, T. Grauschopf, S. Krüger, F. Nörtemann, M. Staufer, M. Mayer, V. A. Nasluzov, U. Birkenheuer, A. Hu, A. V. Matveev, A. M. Shor, M. S. K. Fuchs-Rohr, K. M. Neyman, D. I. Ganyushin, T. Kerdcharoen, A. Woiterski, S. Majumder, M. H. i Rotllant, R. Ramakrishnan, G. Dixit, A. Nikodem, T. M. Soini, M. Roderus, N. Rösch, ParaGauss Version 3.1.9, Technische Universität München, 2013.
- [41] A. D. Becke, *Phys. Rev. A* 38 (1988) 3098.
- [42] J. P. Perdew, *Phys. Rev. B* 33 (1986) 8822.
- [43] V. Vallet, P. Macak, U. Wahlgren, I. Grenthe, *Theor. Chem. Acc.* 115 (2006) 145.
- [44] A. Kremleva, S. Krüger, N. Rösch, *Inorg. Chim. Acta* 362 (2009) 2542.
- [45] M. S. K. Fuchs, A. M. Shor, N. Rösch, *Int. J. Quantum Chem.* 86 (2002) 487.
- [46] P. E. Blöchl, *Phys. Rev. B* 50 (1994) 17953.
- [47] G. Kresse, D. Joubert, *Phys. Rev. B* 59 (1999) 1758.
- [48] G. Kresse, J. Furthmüller, *Phys. Rev. B* 54 (1996) 11169.
- [49] G. Kresse, J. Hafner, *Phys. Rev. B* 49 (1994) 14251.
- [50] G. Kresse, J. Hafner, *Phys. Rev. B* 47 (1993) 558.
- [51] G. Kresse, J. Hafner, *Phys. Rev. B* 48 (1993) 13115.
- [52] G. Kresse, J. Furthmüller, *Comput. Mater. Sci.* 6 (1996) 15.
- [53] A. H. MacDonald, S. H. Vosko, *J. Phys. C* 12 (1979) 2977.
- [54] W. Koch, M. C. Holthausen, *A Chemist's Guide to Density Functional Theory*, 2. ed. Wiley-VCH: Weinheim, 2000.
- [55] J. P. Perdew, Y. Wang, *Phys. Rev. B* 45 (1992) 13244.
- [56] T. Ziegler, *Chem. Rev.* 91 (1991) 651.
- [57] A. Kremleva, S. Krüger, N. Rösch, *J. Phys. Chem. C* 120 (2016) 324.
- [58] A. S. Pereira Gomes, F. Réal, B. Schimmelpfennig, U. Wahlgren, V. Vallet, in *Computational Methods in Lanthanide and Actinide Chemistry*, M. Dolg (Ed.), Wiley: Chichester, 2015, Chapt. 11.
- [59] X. Cao, A. Weigand, in *Computational Methods in Lanthanide and Actinide Chemistry*, M. Dolg (Ed.), Wiley: Chichester, 2015, Chapt. 6.
- [60] E. van Lenthe, E. J. Baerends, J. G. Snijders, *J. Chem. Phys.* 99 (1993) 4597.
- [61] E. van Lenthe, E. J. Baerends, J. G. Snijders, *J. Chem. Phys.* 101 (1994) 9783.
- [62] M. Dolg (Ed.), *Computational Methods in Lanthanide and Actinide Chemistry*, Wiley: Chichester, 2015.
- [63] C. Clavaguéra-Sarrio, V. Vallet, D. Maynau, C. J. Marsden, *J. Chem. Phys.* 121 (2004) 5312.
- [64] J. Tomasi, M. Persico, *Chem. Rev.* 94 (1994) 2027.
- [65] J. Tomasi, B. Menucci, R. Cammi, *Chem. Rev.* 105 (2005) 2999.
- [66] P. Wählin, B. Schimmelpfennig, U. Wahlgren, I. Grenthe, V. Vallet, *Theor. Chem. Acc.* 124 (2009) 377.
- [67] S. Vukovic, B. P. Hay, V.S. Bryantsev, *Inorg. Chem.* 54 (2015) 3995.
- [68] M. Bühl, G. Wipff, *Chem. Phys. Chem.* 12 (2011) 3095.
- [69] B. Rode, T. Hofer, B. Randolph, C. Schwenk, D. Xenides, V. Vchirawongkwin, *Theor. Chem. Acc.* 115 (2006) 77.
- [70] A. Tirlir, T. Hofer, *J. Phys. Chem. B* 118 (2014) 12983.
- [71] F. Hirata, *Molecular Theory of Solvation*, Kluwer Academic Publisher: Dordrecht, 2003.
- [72] B. Li, A. V. Matveev, S. Krüger, N. Rösch, *Comp. Theor. Chem.* 1051 (2015) 151.
- [73] B. Li, A. V. Matveev, *J. Phys. Chem. A* 119 (2015) 8702.
- [74] J. A. Greathouse, R. T. Cygan, *Environ. Sci. Tech.* 40 (2006) 3865.
- [75] S. Kerisit, C. X. Liu, *Environ. Sci. Tech.* 48 (2014) 3899.
- [76] S. Lectez, J. Roques, M. Salanne, E. Simoni, *J. Chem. Phys.* 137 (2012) 134705.
- [77] K. Sebbari, J. Roques, C. Domain, E. Simoni, *J. Chem. Phys.* 137 (2012) 164701.
- [78] A. K. Vatti, M. Todorova, J. Neugebauer, *Langmuir* 32 (2016) 1027.
- [79] S. N. Steinmann, P. Sautet, *J. Phys. Chem.* 120 (2016) 5619.
- [80] W. A. Runde, W. W. Schulz in *Actinide and Transactinide Elements*, L. R. Morss, N. M. Edelstein, J. Fuger (Eds.), 3. Ed., Springer: Dordrecht, 2006, Chap. 8.8.2.
- [81] J. Wiebke, A. Moritz, X. Cao, M. Dolg, *Phys. Chem. Chem. Phys.* 9 (2007) 459.
- [82] S. Stumpf, T. Stumpf, K. Dardenne, C. Hennig, H. Foerstendorf, R. Klenze, T. Fanghänel, *Environ. Sci. Technol.* 40 (2006) 3522.
- [83] D. R. Fröhlich, A. Skerencak-Frech, N. Bauer, A. Rossberg, P. J. Panak, *J. Synchrotron Rad.* 22 (2015) 99.
- [84] T. Stumpf, C. Hennig, A. Bauer, M. A. Denecke, T. Fanghänel, *Radiochim. Acta* 92 (2004) 133.
- [85] P. G. Allen, J. J. Bucher, D. K. Shuh, N. M. Edelstein, I. Craig, *Inorg. Chem.* 39 (2000) 595

- [86] M. Duvail, F. Martelli, P. Vitorge, R. Spezia, *J. Chem. Phys.* 135 (2011) 044503.
- [87] P. D'Angelo, R. Speza, *Chem. Eur. J.* 18 (2012) 11162.
- [88] G. R. Choppin, M. P. Jensen in *Actinide and Transactinide Elements*, L. R. Morss, N. M. Edelstein, J. Fuger (Eds.), 3. Ed., Springer: Dordrecht, 2006, Chap. 23.2.1.
- [89] A. S. Pershin, T. V. Sapozhnikova, *J. Radioanal. Nuc. Chem.* 143 (1990) 455.
- [90] G. R. Choppin, L. F. Rao, *Radiochim. Acta* 37 (1984) 143.
- [91] C. Lucks, A. Rossberg, S. Tsushima, H. Foerstendorf, K. Fahmz, G. Bernhard, *Dalton Trans.* 42 (2013) 13584.
- [92] J. Jiang, L. Rao, P. Di Bernardo, P. L. Zanonato, A. Bismondo, *J. Chem. Soc., Dalton Trans.* (2002) 1832
- [93] E. H. Bailey, J. F. W. Mosselmans, P. F. Schofield, *Geochim. Cosmochim. Acta* 68 (2004) 1711.
- [94] K. Takao, S. Takao, A. C. Scheinost, G. Bernhard, C. Hennig, *Inorg. Chem.* 48 (2009) 8803.
- [95] A. S. A. Khan, R. Ahmed, M. L. Mirza, *Radiochim. Acta* 95 (2007) 693.
- [96] A. Kirishima, Y. Onishi, N. Sato, O. Tochiyama, *J. Chem. Thermodyn.* 39 (2007) 1432.
- [97] I. Grenthe, J. Drozdzyński, T. Fujino, E. C. Buck, T. E. Albrecht-Schmidt, S. F. Wolf in *Actinide and Transactinide Elements*, L. R. Morss, N. M. Edelstein, J. Fuger (Eds.), 3. Ed., Springer: Dordrecht, 2006, Chap. 5.10.2.
- [98] V. Sladkov, *J. Chromatogr. A* 1289 (2013) 133.
- [99] F. Rösch, S. Dittrich, G. V. Buklanov, M. Milanov, V. A. Khalkin, R. Dreyer, *Radiochim. Acta* 49 (1990) 29.
- [100] K. Takao, S. Takao, A. C. Scheinost, G. Bernhard, C. Hennig, *Inorg. Chem.* 48 (2009) 8803.
- [101] P. G. Allen, J. J. Bucher, D. K. Shuh, N. M. Edelstein, T. Reich, *Inorg. Chem.* 36 (1997) 4676.
- [102] T. Reich, G. Bernhard, G. Geipel, H. Funke, C. Hennig, A. Rossberg, W. Matz, N. Schell, H. Nitsche, *Radiochim. Acta* 88 (2000) 633.
- [103] J.-M. Combes, C. J. Chisholm-Brause, G. E. Brown, G. A. Parks, S. D. Conradson, P. G. Eller, I. R. Triay, D. E. Hobart, A. Meijer, *Environ. Sci. Tech.* 26 (1992) 376.
- [104] S. Krüger, F. Schlosser, R. S. Ray, N. Rösch in *Lecture Series on Computer and Computational Science*, T. E. Simos, G. Maroulis (Eds.), Koninklijke Brill: Leiden, 2006, Vol. 7, p. 904.
- [105] M. Kakihana, T. Nagumo, M. Okamoto, H. Kakihana, *J. Phys. Chem.* 91 (1987) 6128.
- [106] A. Barkleit, J. Kretschmar, S. Tsushima, M. Acker, *Dalton Trans.* 43 (2014) 11221.
- [107] R. Moore, M. Borkowski, M. Bronikowski, J. Chen, O. Pokrovsky, Y. Xia and G. Choppin, *J. Sol. Chem.*, 28 (1999) 521.
- [108] G. X. Tian, L. R. Martin, L. F. Rao, *Inorg. Chem.* 49 (2010) 10598.
- [109] C. Lucks, PhD Thesis, Institut für Ressourcenökologie, Helmholtz-Zentrum Dresden-Rossendorf, 2013.
- [110] D. R. Fröhlich, A. Skerencak-Frech, U. Kaplan, C. Koke, A. Rossberg, P. J. Panaka, *J. Synchrotron Rad.* 22 (2015) 1469.
- [111] R. D. Shannon, *Acta Crystallogr. A* 32 (1976) 751.
- [112] W. Stumm, J. J. Morgan, *Aquatic Chemistry*, Wiley: Chichester, 3. ed., 1996.
- [113] P. Debye, E. Hückel, *Physik Z.* 24 (1923) 185 (1923).
- [114] L. Ciavatta, *Ann. Chim.* 70 (1980) 551.
- [115] K. S. Pitzer (Ed.), *Activity Coefficients in Electrolyte Solutions*, CRC Press: Boca Raton, 1991, Chap. 3.
- [116] P. Thakur, Y. Chiong, M. Borkowski, G. Choppin, *Geochim. Cosmochim. Acta* 133 (2014) 299.
- [117] R. Buchner, G. T. Hefter, P. M. May, *J. Phys. Chem. A* 103 (1998) 1.
- [118] R. L. Bassett, *Geochim. Cosmochim. Acta* 44 (1980) 1151.
- [119] J. Schott, J. Kretschmar, S. Tsushima, B. Drobot, M. Acker, A. Barkleit, S. Taut, V. Brendler, T. Stumpf, *Dalton Trans.* 44 (2015) 11095.
- [120] M. Attinà, F. Cacace, G. Occhiucci, A. Ricci, *Inorg. Chem.* 31 (1992) 3114.
- [121] C. Su, D. L. Suarez, *Environ. Sci. Technol.* 20 (1995) 302.
- [122] P. L. Zanonato, P. Di Bernardo, I. Grenthe, *Dalton Trans.* 43 (2014) 2378.
- [123] F. A. Cotton, G. Wilkinson, *Advanced Inorganic Chemistry*, Wiley, Chichester, 5th ed., 1988, p. 171
- [124] J. Schott, J. Kretschmar, M. Acker, S. Eidner, M. U. Kumke, B. Drobot, A. Barkleit, S. Taut, V. Brendler, T. Stumpf, *Dalton Trans.* (2015) 43 11516.
- [125] Nagra Project Opalinus Clay – safety report: Demonstration of disposal feasibility for spent fuel, vitrified-high level waste and long-lived intermediate level waste (Entsorgungsnachweis), NTB 02-05, Nagra: Wettingen, Switzerland, 2002.
- [126] Hartmann, H, Geckeis, T. Rabung, J. Lützenkirchen, T. Fanghänel, *Radiochim. Acta* 96 (2008) 699.
- [127] K. A. Carrado in *Handbook of Layered Materials*, S. M. Auerbach, K. A. Carrado, P. K. Dutta (Eds.), Marcel Dekker: New York, 2004, Chap. 1.
- [128] F. Wolters, G. Lagaly, G. Kahr, R. Nueesch, K. A. Emmerich, *Clays Clay Min.* 57 (2009) 115.

- [129] A. Kremleva, S. Krüger, N. Rösch, *Phys. Chem. Chem. Phys.* 17 (2015) 13757.
- [130] P. Hartmann, W. G. Perdok, *Acta Cryst.* 8 (1955) 49.
- [131] P. Hartmann, W. G. Perdok, *Acta Cryst.* 8 (1995) 521.
- [132] P. Hartmann, W. G. Perdok, *Acta Cryst.* 8 (1995) 525.
- [133] G. N. White, L. W. Zelazny, *Clays Clay Minerals* 36 (1988) 141.
- [134] Y. Kuwahara, *Am. Min.* 91 (2006) 1142.
- [135] M. D. Liptak, G. C. Shields, *Int. J. Quantum Chem.* 85 (2001) 727.
- [136] L. Pauling, *J. Am. Chem. Soc.* 51 (1929) 1010.
- [137] A. Kremleva, S. Krüger, N. Rösch, *Geochim. Cosmochim. Acta* 75 (2011) 706.
- [138] E. R. Sylwester, E. A. Hudson, P. G. Allen, *Geochim. Cosmochim. Acta* 64 (2000) 2431.
- [139] M. L. Schlegel, M. Descostes, *Environ. Sci. Tech.* 43 (2009) 8593.
- [140] S. Tazi, B. Rotenberg, M. Slanne, M. Sprik, M. Sulpizi, *Geochim. Cosmochim. Acta* 94 (2012) 1.
- [141] S. V. Churakov *Geochim. Cosmochim. Acta* 71 (2007) 1130.
- [142] X. Liu, X. Lu, M. Sprik, J. Cheng, E. J. Meijer, R. Wang, *Geochim. Cosmochim. Acta* 117 (2013) 180.
- [143] I. Grenthe, J. Fuger, R. Konings, R. Lemire, A. Muller, C. Nguyen-Trung, H. Wanner, *Chemical Thermodynamics of Uranium*, OECD Publications: Paris, 2004.
- [144] X. D. Liu, J. Cheng, M. Sprik, X. C. Lu, R. C. Wang, *Geochim. Cosmochim. Acta* 140 (2014) 410.
- [145] A. Kremleva, S. Krüger, *Clays Clay Min.* (2016), accepted.
- [146] A. Kremleva, S. Krüger, N. Rösch, *Surf. Sci.* 615 (2013) 21.
- [147] S. V. Churakov, *Geochim. Cosmochim. Acta* 71 (2007) 1130.
- [148] R. Bader, *Atoms in molecules: A quantum theory*, Oxford University Press: New York, 1990.
- [149] I. D. Brown, D. Altermatt, *Acta Cryst. B* 41 (1985) 244.
- [150] C. Hennig, T. Reich, R. Dähn, A. M. Scheidegger, *Radiochim. Acta* 90 (2002) 653.
- [151] J. G. Catalano, G. E. Brown, *Geochim. Cosmochim. Acta* 69 (2005) 2995.
- [152] S. L. Dudarev, G. A. Botton, S. Y. Savrasov, C. J. Humphreys, A. P. Sutton, *Phys. Rev. B* 57 (1998) 1505.
- [153] G. Bidoglio, G. Tanet, A. Chatt, *Radiochim. Acta* 38 (1985) 21.
- [154] D. R. Turner, R. T. Pabalan, F. T. Bertetti, *Clays Clay Min.* 46 (1998) 256.
- [155] S. Amayri, A. Jermolajev, T. Reich, *Radiochim. Acta* 99 (2011) 349.
- [156] K. Schmeide, G. Bernhard, *Appl. Geochem.* 25 (2010) 1238.
- [157] Y. Arai, P. B. Moran, B. D. Honeyman, J. A. Davis, *Environ. Sci. Tech.* 41 (2007) 3944.
- [158] O. Tochiyama, H. Yamazaki, T. Mikami, T. (1996). *Radiochim. Acta* 43 (1996) 191.
- [159] K. Müller, H. Foerstendorf, V. Brendler, G. Bernhard, *Env. Sci. Tech.* 43 (2009) 7665.
- [160] K. Gückel, A. Rossberg, K. Müller, V. Brendler, G. Bernhard, H. Foerstendorf, *Environ. Sci. Tech.* 47 (2013) 14418.
- [161] T. Reich, T. Y. Reich, S. Amayri, J. Drebert, N. L. Banik, R. A. Buda, J. V. Kratz, N. Trautmann, in: *X-ray Absorption Fine Structure – XAFS13*, B. Hedman, P. Painetta, (Eds.), 2007, p. 179.
- [162] S. Amayri, N. L. Banik, M. Breckheimer, R. A. Buda, S. Burger, J. Drebert, A. Jermolajev, J. V. Kratz, B. Kuczewski, D. Kutscher, T. Y. Reich, T. Reich, N. Trautmann, in: *Migration of Actinides in the System Clay, Humic Substances, Aquiver*, C. M. Marquardt, (Ed.), Forschungszentrum Karlsruhe: Karlsruhe, 2008, p. 141.
- [163] R. Lemire, J. Fuger, H. Nitsche, P. Potter, M. Rand, J. Rydberg, K. Spahiu, J. Sullivan, W. Ullman, P. Vitorge, H. Wanner, *Chemical Thermodynamics of Neptunium and Plutonium*, Elsevier: Amsterdam, 2001.
- [164] A. Schnurr, *Untersuchungen zur Radionuklidisorption an Tonmineraloberflächen bei hohen Ionenstärken*, PhD Thesis, Karlsruhe, 2015.
- [165] A. Schnurr, R. Marsac, T. Rabung, J. Lützenkirchen, H. Geckeis, *Geochim. Cosmochim. Acta* 151 (2015) 192.
- [166] Y. Markus, *Chem. Rev.* 109 (2009) 1346.